Study of the $^{12}C(e, e'p)$ Reaction in a Correlations Dominant Regime with $Q^2 = 2.0$ (GeV/c)^2 and $X_B > 1$

by

Peter Monaghan

Submitted to the Department of Physics
in partial fulfillment of the requirements for the degree of

Doctor of Philosophy

at the

MASSACHUSETTS INSTITUTE OF TECHNOLOGY

May 2008

© Massachusetts Institute of Technology 2008. All rights reserved.

Author . . . .
Department of Physics
May 9, 2008

Certified by . . . .
William Bertozzi
Professor of Physics
Thesis Supervisor

Certified by . . . .
Shalev Gilad
Senior Research Scientist
Thesis Co-Supervisor

Accepted by . . . .
Thomas J. Greytak
Associate Department Head for Education

Study of the ${}^{12}C(e, e'p)$ Reaction in a Correlations Dominant Regime with $Q^2 = 2.0$ (GeV/c)^2 and $X_B > 1$

by

Peter Monaghan

Submitted to the Department of Physics
on May 9, 2008, in partial fulfillment of the
requirements for the degree of
Doctor of Philosophy

Abstract

This experiment was motivated by studying short-range nucleon-nucleon correlations via multinucleon knockout reactions—$(e, e'pN)$. The data were taken in Hall A at Jefferson Lab using the pair of high resolution spectrometers to detect the $(e, e'p)$ reaction data, and using a third large acceptance spectrometer called *BigBite* to detect the second nucleon ejected from the nucleus. The kinematics were chosen to be conducive for studying short-range correlations—namely a large momentum transfer and $x_B > 1$. The central kinematic values used during the experiment were $Q^2 = 2$ (GeV/c)^2 and $x_B = 1.2$, although the spectrometer acceptances resulted in a range of both Q^2 and x_B being recorded in the data. While the electron spectrometer was unchanged during the experiment, the proton spectrometer was changed to cover a range of missing momentum values, $\vec{P}_m \sim 200 - 650$ MeV/c; this resulted in three different datasets.

This thesis presents the analysis and results of the $(e, e'p)$ reaction channel. The motivation of the experiment is discussed and a description of the experimental equipment is given. The methods used to calibrate the equipment, improve the analysis software and to extract the cross-sections from the data are described. The cross-section results from both the ${}^{12}C(e, e'p)^{11}B$ bound state and the ${}^{12}C(e, e'p)$ continuum reaction channels are presented.

The ${}^{12}C(e, e'p)^{11}B$ results are compared to theoretical calculations and show agreement for $P_m < 300$ MeV/c but significant disagreement at larger missing momenta. The data from different kinematic settings which overlap in missing momentum around $\vec{P}_m = 400$ MeV/c did not provide sufficient statistics to extract a meanful cross-section measurement.

The ${}^{12}C(e, e'p)$ continuum cross-sections are extracted as a function of missing energy over a range of missing momentum. A peak is observed in the cross-sections as a function of missing momentum; this is consistent with scattering from a quasideuteron pair. However, the peak location is different from the location predicted using the quasideuteron model. A suggested modification to the quasideuteron model, namely that the remaining nucleons are not at rest, results in a predicted peak location in the cross-section which lies closer to the observed peak location.

The reduced cross-section is also extracted by dividing the results by the single-nucleon offshell cross-section; the σ_{cc2} prescription of DeForest is used. This reduced cross-section for the same missing momentum and missing energy bins is compared for the three different kinematic settings. No agreement is found between the different datasets showing that the plane-wave impulse approximation does not describe the data. The data presented for the $^{12}C(e,e'p)$ reaction allows theorists a direct comparison between data and their calculations. We hope it will provide motivation for theorists to improve their calculations and models of the reaction mechanism. Although no theoretical calculations are currently available for comparison, it is anticipated that they will be available in the near future.

Thesis Supervisor: William Bertozzi
Title: Professor of Physics

Thesis Co-Supervisor: Shalev Gilad
Title: Senior Research Scientist

This thesis is dedicated to my mother and father for all their love,
encouragement and support.

Charles Joseph Monaghan, 1935 -
Bridget Monaghan 1935-2003

Contents

1 Introduction **27**

2 Physics Motivation **33**

2.1 Inclusive (e, e') Experiments 34

2.2 Semi-Inclusive $(e, e'p)$ Experiments 35

2.3 Multinucleon Knockout Experiments 38

2.4 This Experiment 39

2.5 The $(e, e'p)$ Reaction 39

2.5.1 Definition of Kinematic Variables 40

2.5.2 The Plane Wave Impulse Approximation 44

2.6 Kinematics for this Experiment 45

3 Experimental Setup **49**

3.1 Electron Accelerator Overview 49

3.2 Hall A Overview 51

3.3 Beamline Components 53

3.3.1 Beam Energy Measurement 53

3.3.2 Beam Current Monitors 54

3.3.3 Beam Position Monitors 56

3.4 Target System 57

3.5 Hall A High Resolution Spectrometers 59

3.5.1 Detector Packages 61

3.6 The BigBite Spectrometer 66

3.6.1 The BigBite Magnet 66
3.6.2 The Proton Detector 66
3.6.3 The Neutron Detector 69
3.6.4 The Complete Package 72
3.7 Data Acquisition System and Trigger Setup 73

4 Spectrometer calibrations and efficiency determination 79
4.1 High Resolution Spectrometer Optics Calibration 79
4.2 Spectrometer Mispointing 85
4.3 HRS Coincidence Time Calibration 87
4.4 Efficiency Determination 89
4.4.1 Trigger Efficiency 89
4.4.2 Tracking Efficiency 90
4.4.3 Particle Identification Efficiency 91
4.4.4 Data Acquisition System Deadtime 94

5 Analysis of $^{12}C(e,e'p)$ Data 97
5.1 Coincidence Time 97
5.2 Particle Identification 98
5.3 Spectrometer Acceptance 100
5.3.1 Pion and Delta-resonance Event Rejection 100
5.4 Measured Data Ranges 105
5.5 Simulation of the Experiment 106
5.6 Experimental $(e,e'p)$ Cross-sections 111
5.6.1 $^{12}C(e,e'p)^{11}B$ Five-fold Differential Cross-section 112
5.6.2 $^{12}C(e,e'p)$ Six-fold Differential Cross-section 114
5.6.3 Kinematic I: $\vec{P}_{miss} = 200 - 450$ MeV/c 120
5.6.4 Kinematic II: $\vec{P}_{miss} = 300 - 550$ MeV/c 120
5.6.5 Kinematic III: $\vec{P}_{miss} = 400 - 650$ MeV/c 124
5.7 Radiative Corrections 124
5.7.1 Internal Bremsstrahlung 127

5.7.2 External Radiation Processes 128
5.8 Systematic Uncertainies 130
5.8.1 Uncertainties in the $^{12}C(e,e'p)^{11}B$ Analysis. 131
5.8.2 Uncertainties in the $^{12}C(e,e'p)$ Continuum Analysis 132

6 Experimental Results **133**
6.1 $^{12}C(e,e'p)^{11}B$ Cross-section Results 133
6.1.1 Extracted Momentum Distribution 135
6.2 $^{12}C(e,e'p)$ Continuum Cross-section Results 138
6.3 Extracted Experimental Spectral Function 147
6.4 Effective Momentum Density 155
6.5 Quasielastic Cross-section Comparison 157
6.6 Tabulated Results 161
6.6.1 Kinematic I Results 161
6.6.2 Kinematic II Results 164
6.6.3 Kinematic III Results 167

7 Summary and Conclusions **171**

List of Figures

1-1 An illustration of the nucleon-nucleon potential as a function of the nucleon-nucleon separation. The repulsive core contributes to nucleon-nucleon correlations at short distances. 29

1-2 The spectroscopic factor from $(e, e'p)$ experiments for various nuclei. The observed values are only 55-75% of the shell model prediction, indicating other effects from the N-N interaction are important. Figure reproduced from [1]. 30

2-1 An illustration of the nucleon-nucleon short-range correlation, with the virtual photon being absorbed by one nucleon which is subsequently knocked-out of the nucleus. Momentum conservation leads to the partner nucleon recoiling with sufficient momentum to be ejected as well when the relative momentum is large compared with the Fermi momentum, k_f. 34

2-2 The results from a Hall B (JLab) inclusive (e, e') experiment; the cross-section ratios of ^{56}Fe, ^{12}C and ^{4}He relative to ^{3}He as a function of x_B are shown. Figure reproduced from [2]. 35

2-3 Cross-section results from $^{3}He(e, e'p)pn$ reaction. The vertical arrow gives the expected position for the disintegration of correlated nucleon-nucleon pairs; the peak location is reasonably well predicted at lower momentum values, but fails at the highest momentum shown. Figure reproduced from [3]. 37

2-4 The experimental spectral function for ^{12}C (solid lines) for several different momenta. The vertical arrow gives the expected missing energy value for two nucleons being ejected from the nucleus. The dashed-dotted lines are the spectral functions predicted by a self-consistent Green's function theory calculation [4]. Figure reproduced from [5]. . 38

2-5 Results from the Eva collaboration $^{12}C(p, 2pn)$ experiment at BNL. The scatter plot shows the cosine of the angle between the recoil neutron momentum and the scattered proton momentum, as a function of the neutron momentum. When the measured recoil neutron momentum is larger than the Fermi momentum in carbon (dashed line) the angle is always larger than 90°. This indicates a directional correlation between the momentum vectors of the proton-neutron pair. 40

2-6 Feynman diagram showing the $(e, e'pN)$ reaction; the exchanged virtual photon is absorbed by a single proton. 41

2-7 The semi-inclusive $(e, e'p)$ reaction and the associated kinematic variables; figure courtesy of [6]. 42

2-8 Feynman diagram showing the $(e, e'p)$ reaction in the plane wave impulse approximation. 44

2-9 Diagram showing the kinematic settings used in the experiment. Note the three proton momentum vectors correspond to the three kinematics given in Table 2.1. 46

3-1 An illustration of the Continuous Electron Beam Accelerator Facility (CEBAF), showing the two accelerating linacs, the recirculating arcs and the three experimental halls, A, B and C. 50

3-2 An illustration of the layout of Hall A during this experiment, showing the approximate locations of the spectrometers used. The accelerator diagram shown is not to scale. 52

3-3 An illustration of the arc beamline section, showing the eight magnets used to deflect the beam. 55

3-4 Diagram of the beam current monitor system. 56

3-5 The primary carbon foil target was rotated by 70° relative to the beam axis as shown. 57

3-6 Photograph showing the target ladder inside the scattering chamber; the 4 cm and 15 cm *cigar tubes* containing liquid hydrogen and liquid deuterium can be easily seen, but the carbon foil target is out of view. 58

3-7 A 3D rendering of the new scattering chamber built for this experiment. Notice the large window opening to utilise the increased acceptance in BigBite. 59

3-8 A side-view schematic of one HRS, showing the quadrupole-quadrupole-dipole-quadrupole magnet arrangement and the location of the detectors; dimensions are given in meters. 60

3-9 A side view of the detector stacks in each spectrometer, showing the detectors used; left figure is for the electron spectrometer; right figure is for the proton spectrometer. 61

3-10 A diagram of the vdc wire planes showing the orientation of the wires relative to the central ray (left figure) and a side view of the vdc pair (right figure). 63

3-11 A typical particle trajectory through the VDC creates a *five-cell event*; i.e. the five wires closest to the trajectory register a hit. Also shown are the electric field lines between the wires and the cathode planes (mylar foils); the electrons drift along the path of least time - the geodetic path - and induce a signal in the wires [7]. 64

3-12 Diagram showing the preshower-shower detector used in the electron spectrometer for particle identification. Note, the transverse and dispersive directions in the figure refer to the coordinates in the spectrometer reference frame. 65

3-13 A side view (left) and above view (right) of the BigBite magnet showing the magnetic field boundary and the large pole face gap. 67

3-14 A 3D drawing of BigBite, showing the magnet and proton detector mounted together on the custom platform. 68

3-15 A 3D rendering of the auxiliary plane; notice that each scintillator bar has only one PMT. 69

3-16 A 3D rendering of the trigger plane, showing the δE and E planes; each scintillator bar in both planes has two PMTs attached, one at each end. 70

3-17 A side view diagram of the neutron detector, showing the layer of 2 cm veto bars at the front and the different heights of 10 cm thick scintillator bars used throughout the four planes of the detector. . . . 71

3-18 A side view diagram of the complete BigBite spectrometer, showing the effective field boundary of the magnet, location of each detector and sample rays of protons and neutrons through each detector. Notice also, the lead wall in front of the neutron detector to provide shielding against photon radiation from the target. 72

3-19 A photo of the complete BigBite spectrometer setup in the hall during the experiment. 73

3-20 Electronics diagrams of the data acquisition system for both the proton and neutron detectors. 75

4-1 The Hall A coordinate system, with its origin defined to be the center of the hall with the z-axis pointing along the electron beam direction. 80

4-2 The target coordinate system; note, that the z_{tg}-axis points along the central axis of the spectrometer and is rotated an angle $\theta_\circ$ from the electron beam direction. The in-plane angle (ϕ_{tg}) and out-of-plane angle (θ_{tg}) of the scattered particle are defined in this coordinate system. 81

4-3 The focal plane coordinate system. Note that Z_{det}, the local central ray is perpendicular to the wire planes in the VDCs. 81

4-4 The y_{tg} reconstruction for the set of carbon optics foils before (black trace) and after (red trace) the database calibration for the Y_{ijkl} matrix elements. 84

4-5 The reconstruction of the sieve hole locations before (left figure) and after (right figure) the calibration for the T_{ijkl} and P_{ijkl} matrix elements. 85

4-6 Definition of the mispointing variables, in the Hall coordinate system; the Y-axis in the hall frame is pointing out of the page. 87

4-7 The coincidence time calibration for the left and right spectrometers; note the left arm measurement (left figure) has better resolution than the right arm measurement. 89

4-8 The sum of ADC signals from the preshower versus shower detectors allows electrons and pions in the left HRS to be easily separated. . . . 92

4-9 Comparison of the β value of particles detected in the proton spectrometer before (upper plot) and after (lower plot) the coincidence time cut is applied. Events corresponding to detected deuterons, protons and pions are shown in the upper plot. After applying the coincidence time cut, only the distribution corresponding to protons survives and so no further proton particle identification cut was necessary. 94

5-1 The HRS coincidence time spectrum from the first dataset. The limits on the cut were chosen by fitting a gaussian function to the peak of the distribution and then finding the limit as $\pm 3\sigma$ of the fitted gaussian. Note, the only part of the coincidence time window is shown here, to highlight the peak region. Background contribution was found to be $\sim 0.46\%$ by taking the same cut as used around the peak and applying it to a region of background events only. 98

5-2 The sum of ADC channels for the preshower versus shower detectors shows the clear separation of electron and pion events. The pions are excluded by removing the events in the region indicated by the red line. With this cut, the electron detection efficiency is 0.997 and the resulting pion contamination was found to be $\sim 0.075\%$. 99

5-3 Comparison of the β value of particles detected in the proton spectrometer before (upper plot) and after (lower plot) the coincidence time cut is applied. Events corresponding to detected deuterons, protons and pions are shown in the upper plot. After applying the coincidence time cut, only the distribution corresponding to protons survives and so no further proton particle identification cut was necessary. 101

5-4 One dimensional distributions of out-of-plane angle (ϕ), in-plane angle (θ) and momentum (δ) acceptances; left plots are for the electron spectrometer, right plots are for the proton spectrometer. The dashed lines indicate the acceptance cuts used on each quantity. Data shown are from kinematic I. 102

5-5 Distributions of electrons in the left spectrometer acceptance with the applied acceptance cuts shown by the solid lines. Left plot shows the out-of-plane angle versus the in-plane angle. Right plot shows the in-plane angle versus the momentum acceptance (given as a percentage of the spectrometer momentum setting). Note that some events reconstruct outside the physical acceptance of the spectrometer. 103

5-6 Distributions of proton in the right spectrometer acceptance with the applied acceptance cuts shown by the solid lines. Left plot shows the out-of-plane angle versus the in-plane angle. Right plot shows the in-plane angle versus the momentum acceptance (given as a percentage of the spectrometer momentum setting). Note that some events reconstruct outside the physical acceptance of the spectrometer. 103

5-7 Two dimensional plot of ω versus y-scaling variable with the solid line representing the chosen empirical cut to reject possible pion or delta-resonance events. All events above the solid line were removed by this cut. The two dashed lines represent variations of this cut used to evaluate the systematic error associated with using this cut. 104

5-8 Three dimensional view of ω-y distribution showing the location of the empirical cut used. Events located to the left of the solid line, in the "pion and Δ" region were removed by this cut. 105

5-9 Missing energy distribution for kinematic I showing the events passing the empirical ω-y cut (dashed line - red online) and those rejected by the cut (dotted line - green online). The two dotted (blue online) lines around the dashed (red) line show the effect of using the upper and lower limiting cuts on the $\omega - y$ distribution and are used to evaluate the systematic error associated with this cut. 106

5-10 Upper Plot: Two-dimensional distribution of events in kinematic II of ω versus y-scaling variable, with empirical cut selected; dotted lines give limits of the systematic check of this cut on the final cross-section result. Lower Plot: Full missing energy distribution for kinematic II; dashed line (red online) shows the distribution after the ω-y cut is applied; dotted line (green online) shows the data rejected by this cut. The two dotted (blue) lines around the dashed (red) line show the effect of the upper and lower limits of the $\omega - y$ cut and are used to evaluate the systematic error associated with this cut. 107

5-11 Upper Plot: Two-dimensional distribution of events in kinematic III of ω versus y-scaling variable, with empirical cut selected; dotted lines give limits of the systematic check of this cut on the final cross-section result. Lower Plot: Full missing energy distribution for kinematic III; dashed line (red online) shows the distribution after the ω-y cut is applied; dotted line (green online) shows the data rejected by this cut. The two dotted (blue) lines around the dashed (red) line show the effect of the upper and lower limits of the $\omega - y$ cut and are used to evaluate the systematic error associated with this cut. 108

5-12 Distribution of missing momentum versus missing energy for kinematic I after all the described cuts have been applied. Note that this dataset shows clearly the bound state peak at low missing energy and momentum. 109

5-13 Distribution of missing momentum versus missing energy for kinematic II after all cuts applied. 109

5-14 Distribution of missing momentum versus missing energy for kinematic III after all cuts have been applied. 110

5-15 An illustration of how the simulation (red line) evolves after each iteration compared with the measured counts in the data (black squared). Note, error bars on the data are statistical only. 115

5-16 Comparison of the missing energy distribution for the data (black squares) and simulation (red triangles). Left plot shows the distribution with the cut at $E_{miss} = 20$ MeV to define the bound state dataset. Right plot shows the full data and simulation distribution; note how the radiative tail from the simulation contributes in the continuum region at higher missing energy values. 116

5-17 Nuclear shell energy level diagram for boron-11 showing the lowest lying levels above the ground state [8]. 118

5-18 Missing energy distribution for the kinematic I bound states data. Dashed line (red online) is the simulated yield for the ground state of boron-11; dotted line (green online) is the simulated yield for the excited states at 4.4 and 5.0 MeV; solid line (blue online) is the sum of the ground and excited states simulations. 119

5-19 Kinematic I missing energy distributions for each missing momentum bin. Black squares are data. Solid line (red online) shows the continuum simulation yield. Dashed line (green online) shows the ground state simulation yield contribution. Dotted line (blue online) shows the excited state simulation contribution. 121

5-20 Kinematic I missing energy distributions for data compared with the total yield from continuum and bound state simulations summed together. 122

5-21 Kinematic II missing energy distributions for each missing momentum bin. Black squares are data. Solid line (red online) shows the continuum simulation yield. Dashed line (green online) shows the ground state simulation yield contribution. Dotted line (blue online) shows the excited state simulation contribution. 123

5-22 Kinematic II missing energy distributions for data compared with the total yield from continuum and bound state simulations summed together. 125

5-23 Kinematic III missing energy distributions for each missing momentum bin. Black squares are data points. Dashed line (red online) is the yield from the continuum simulation. 126

5-24 An example of the effect of radiation on the data and simulated yields; data are shown for a single missing momentum bin from kinematic III by the black squares. Dashed line (red online) is the yield from the radiated simulation which has been fitted to the data. Dotted line (green online) is the radiatively corrected simulation yield, from which the cross-section is extracted from. The dotted (green) line for the radiatively corrected simulated yield shows more counts at lower missing energy values as radiation causes events to have a larger missing energy and missing momentum values. 129

5-25 The ratio of the radiative corrected yield to non-corrected yield from Fig. 5-24, giving the radiation correction factor bin-by-bin in the missing energy distribution for the given missing momentum bin. 130

6-1 Five-fold differential cross-section extracted for the kinematic I data as a function of missing momentum. The solid curve (red online) is a fully-relativistic mean field theoretical calculation; the dashed curve (blue online) is plane wave impulse approximation calculation. Data shows good agreement with the relativistic calculation for $P_m < 300$ MeV/c but disagrees at larger momenta. Both theoretical calculations are courtesy of J. M. Udias [9]. 134

6-2 Acceptance averaged unit cross-section, $K\sigma_{cc2}$, used as a divisor of the experimental extracted cross-section to produce the extracted distorted momentum distribution. 136

6-3 Extracted distorted momentum distribution from kinematic I data for $^{12}C(e,e'p)^{11}B$ reaction. The solid line (red online) is the reduced cross-section from the relativistic mean full calculation of the cross-section. The dotted line is the reduced cross-section for the plane wave calculation. 137

6-4 Three dimensional plots of yield (upper left), phase space (upper right) and cross-section (lower plot) extracted from MCEEP for kinematic I continuum data. 139

6-5 Three dimensional plots of yield (upper left), phase space (upper right) and cross-section (lower plot) extracted from MCEEP for kinematic II continuum data. 140

6-6 Three dimensional plots of yield (upper left), phase space (upper right) and cross-section (lower plot) extracted from MCEEP for kinematic III continuum data. 141

6-7 Upper plot: Momentum of the recoil partner neutron determined from time-of-flight measurements in the neutron detector. Lower plot: Momentum of recoil partner neutron if assumed to be equal to the missing momentum $\vec{P}_{miss}$. This data is for kinematic III only and figure is courtesy of R. Subedi [10]. 144

6-8 The cross-section ratios of $(e,e'pn)/(e,e'p)$ (blue, upper point) and $(e,e'pp)/(e,e'p)$ (red, lower point) corrected for acceptance and extrapolated for all possible partner nucleons available. Together the sum is (within errors) equal to unity, meaning that a recoil partner nucleon is emitted for every $(e,e'p)$ event. This data is for kinematic III only and courtesy of R. Subedi [10]. 145

6-9 The distribution of missing energy of the (A-2) system as measured in BigBite through the $^{12}C(e,e'pp)$ reaction. The two proton knockout begins in the $(1p^2)$ regime and continues to higher energy. Therefore, the excitation energy of the (A-2) system is taken relative to this region and for the purposes of a simple calculation is taken as 25 MeV ($1s1p - 1p^2$ regions)This data is for all three kinematics together and courtesy of R. Shneor [11]. 146

6-10 Kinematic I extracted cross-section as a function of missing energy for each individual missing momentum bin. The solid (red online) arrow shows the location of the peak in the cross-section based on the recoiling system being a spectator in the reaction; dashed arrow (green online) shows the expected peak location based on a model with the recoiling system having non-zero momentum; the dotted arrow (blue online) shows the expected peak location based on a model which includes the excitation energy of the (A-2) system. 148

6-11 Kinematic II extracted cross-section as a function of missing energy for each individual missing momentum bin. The solid (red online) arrow shows the location of the peak in the cross-section based on the recoiling system being a spectator in the reaction; dashed arrow (green online) shows the expected peak location based on a model with the recoiling system having non-zero momentum; the dotted arrow (blue online) shows the expected peak location based on a model which includes the excitation energy of the (A-2) system. 149

6-12 Kinematic III extracted cross-section as a function of missing energy for each individual missing momentum bin. The solid (red online) arrow shows the location of the peak in the cross-section based on the recoiling system being a spectator in the reaction; dashed arrow (green online) shows the expected peak location based on a model with the recoiling system having non-zero momentum; the dotted arrow (blue online) shows the expected peak location based on a model which includes the excitation energy of the (A-2) system. 150

6-13 The extracted spectral function as a function of missing energy for each missing momentum bin in kinematic I. The average value of Bjorken-X and y scaling variables is also quoted for each plot. The dashed (red online) curve is fitted to the peak location to facilitate calculation of the integral of the spectral function over the missing energy range. . . 152

6-14 The extracted spectral function as a function of missing energy for each missing momentum bin in kinematic II. The average value of Bjorken-X and y scaling variables is also quoted for each plot. The dashed (red online) curve is fitted to the peak location to facilitate calculation of the integral of the spectral function over the missing energy range. . . 153

6-15 The extracted spectral function as a function of missing energy for each missing momentum bin in kinematic III. The average value of Bjorken-X and y scaling variables is also quoted for each plot. The dashed (red online) curve is fitted to the peak location to facilitate calculation of the integral of the spectral function over the missing energy range. . . 154

6-16 Comparison of reduced cross-section (spectral function) for missing momentum bins which overlap between two or more of the kinematic settings. Black squares are kinematic I data; red circles are kinematic II data; green triangles are kinematic III data. 156

6-17 Comparison of the effective momentum density for each dataset from the continuum reaction (integrated reduced cross-section) as a function of missing momentum. The black squares are data the reduced cross-section for the $^{12}C(e, e'p)^{11}B$ reaction. The fact that the continuum datasets do not overlap for the same missing momenta values is another indication of the breakdown of the factorisation model of the cross-section and that other effects contribute significantly to the cross-section. 158

6-18 The extracted quasielastic cross-section as a function of missing energy for different missing momenta. A cut of $x_B = 1 \pm 1\%$ was used to extract these cross-sections and thus only a limited range of missing momentum is covered in each kinematic. 159

6-19 A comparison of the quasielastic cross-section extracted using $x_B = 1 \pm 1\%$ and the continuum cross-sections extracted without using this constraint on Bjorken-X. For the same missing momentum bin, the *full* cross-section (not using the x_B cut) has a tail arising from the data at $x_B = 1$. 160

List of Tables

2.1 The three kinematic settings used during this experiment. The electron spectrometer was unchanged, but the proton spectrometer was changed to map out a wider range of missing momentum. 46

3.1 A list of targets used during the experiment and their material properties. 58
3.2 The general characteristics of each Hall A HRS. 61

4.1 Track reconstruction efficiencies for electron and proton spectrometers, for each kinematic setting. 92

5.1 Kinematic settings of the electron and proton spectrometer used in this experiment. 106
5.2 Systematic normalisation uncertainties applicable throughout the data analysis; the total is the sum in quadrature of the individual normalisation uncertainties. 131

6.1 Results for $^{12}C(e, e'p)^{11}B$ reaction in kinematic I; statistical and systematic errors are given for each data point; errors on the Q^2 and ω values are the standard deviation of the distribution for that missing momentum bin. 137
6.2 Results for kinematic I: $P_{miss} = 200 \pm 25$ MeV/c 161
6.3 Results for kinematic I: $P_{miss} = 250 \pm 25$ MeV/c 162
6.4 Results for kinematic I: $P_{miss} = 300 \pm 25$ MeV/c 162
6.5 Results for kinematic I: $P_{miss} = 350 \pm 25$ MeV/c 162
6.6 Results for kinematic I: $P_{miss} = 400 \pm 25$ MeV/c 163

6.7 Results for kinematic I: $P_{miss} = 450 \pm 25$MeV/c 163
6.8 Results for kinematic II: $P_{miss} = 300 \pm 25$ MeV/c 164
6.9 Results for kinematic II: $P_{miss} = 350 \pm 25$ MeV/c 164
6.10 Results for kinematic II: $P_{miss} = 400 \pm 25$ MeV/c 165
6.11 Results for kinematic II: $P_{miss} = 450 \pm 25$ MeV/c 165
6.12 Results for kinematic II: $P_{miss} = 500 \pm 25$ MeV/c 166
6.13 Results for kinematic II: $P_{miss} = 550 \pm 25$ MeV/c 166
6.14 Results for kinematic III: $P_{miss} = 400 \pm 25$ MeV/c 167
6.15 Results for kinematic III: $P_{miss} = 450 \pm 25$ MeV/c 167
6.16 Results for kinematic III: $P_{miss} = 500 \pm 25$ MeV/c 168
6.17 Results for kinematic III: $P_{miss} = 550 \pm 25$ MeV/c 168
6.18 Results for kinematic III: $P_{miss} = 600 \pm 25$ MeV/c 169
6.19 Results for kinematic III: $P_{miss} = 650 \pm 25$ MeV/c 169

Chapter 1

Introduction

One of the main goals of nuclear physics is to understand the structure of nuclei and to understand how nucleons interact with one another. With this in mind, a full theoretical model of the observed behaviour of nuclei would have to include all possible nucleon interactions over all degrees of freedom for each nucleon – clearly an impossibly large dimensional problem to solve. Instead, the study of nuclei has proceeded by use of different theories and models to describe the properties, structure, and behaviour of nuclei observed under certain experimental conditions. By studying nuclei through continually improving experiments, our understanding is increased, allowing new, more comprehensive theoretical models to be developed. This cycle continues when new experiments are performed to test these enhanced theories and further our understanding of the physics of nuclei.

As a tool for studying nuclei, *electron scattering* affords physicists the opportunity to peer inside the nucleus and examine not only the structure, but under carefully chosen experimental conditions, the behaviour of interactions between individual protons and neutrons. The advent of high current, high energy and continuous wave electron accelerators has enabled more varied study of nuclei without being limited by the relative weakness of the electromagnetic interaction compared with hadronic interactions. The electromagnetic interaction is well understood from quantum electrodynamics (QED). In the one photon exchange approximation, the reaction proceeds via exchange of a virtual photon between the electron probe and the target nucleus. The virtual photon can sample the whole nuclear volume while hadronic probes mostly sample the nuclear surface.

A successful approximation to the many-body system of strongly interacting nucleons with a nucleus is the *Independent Particle Shell Model* [12] (IPSM). This model assumes each nucleon moves independently in a *mean field* potential which represents the average interaction with all other nucleons in the nucleus. The Pauli Exclusion Principle prevents identical fermions from occupying the same single particle state and so shells within the nucleus are populated sequentially. Nucleon transitions to occupied states are forbidden. The IPSM has been relatively successful in predicting the properties of low-level states in odd-A nuclei.

The IPSM replaces the real wavefunction with a set of single particle wavefunctions which are the solution of a Hamiltonian containing only the mean field potential. This restricts the wavefunction to be a product of the individual wavefunctions for each particle and hence, the particles are independent of one another. The model excludes explicit *correlation* functions between two or more particles; for example, functions dependent on $(\vec{r}_i - \vec{r}_j)$. Since the mean field potential is the average interaction, it does include implicit dependencies on correlations. Evidence from nucleon-nucleon scattering experiments shows that the strong interaction between nucleons consists of a both a repulsive part at short distances (typically less than 1 fm) and an attractive part at larger separations ($>$ 1 fm); an example of such an interaction potential is shown in Fig. 1-1. As the nucleon-nucleon interaction becomes increasingly repulsive as internucleon separations decrease, so contributions to the real wavefunction from particle correlations will become more important. Thus, correlations can arise from the part of the nucleon-nucleon interaction which is neglected by the approximate Hamiltonian implicit in the IPSM.

It has been observed in semi-inclusive $(e, e'p)$ experiments that the spectroscopic factors, which represent the occupancy of shell model states, are significantly less than unity [1, 13]. The observed spectroscopic factors for electron scattering from several different nuclei vary from $\sim 55\% - 70\%$ and are shown in Fig. 1-2. This means that the boundary between occupied and unoccupied states (referred to as the *Fermi*

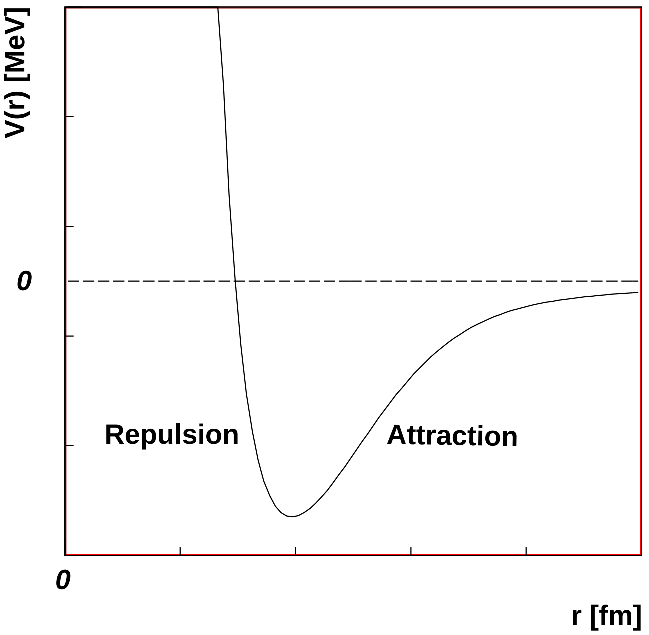

Figure 1-1: An illustration of the nucleon-nucleon potential as a function of the nucleon-nucleon separation. The repulsive core contributes to nucleon-nucleon correlations at short distances.

level) becomes blurred. Thus, an effect of correlations (both repulsive short-range and attractive long-range) in the nucleon-nucleon interaction is to deplete states below the Fermi level and populate states above the Fermi level at higher excitation energies. The short-range correlations give rise to additional high momentum components of the relative wavefunctions of nucleons.

Another experimental indication of nucleon-nucleon correlations comes from inclusive (e, e') quasi-elastic electron scattering experiments investigating the Coulomb Sum Rule. The Coulomb Sum Rule states that the integral of the longitudinal quasi-elastic electron response function, $R_L(\vec{q}, \omega)$, over the full range of energy loss ω at sufficiently large momentum transfer q (typically $|\vec{q}| > 500$ MeV/c), should be equal to the number of protons, Z, in a nucleus. This assumes that the nucleon charge form factor inside the nucleus is equal to that off a free nucleon. While some experiments have observed saturation of the Coulomb Sum Rule in helium and deuterium, other

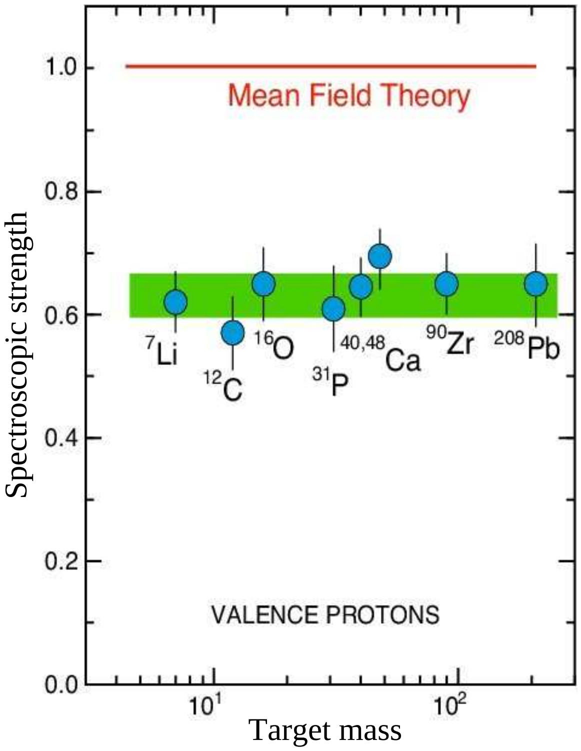

Figure 1-2: The spectroscopic factor from $(e, e'p)$ experiments for various nuclei. The observed values are only 55-75% of the shell model prediction, indicating other effects from the N-N interaction are important. Figure reproduced from [1].

experiments have observed quenching of the sum rule for heavier nuclei, up to 30% of the expected saturation limit; see [14] for a full review. The analysis presented in [15] shows that the observed quenching of the sum rule cannot be explained by nucleon-nucleon correlations alone and nuclear medium modification effects may also be important.

The short distance structure of the nucleon-nucleon interaction can be studied through single and multi-nucleon knockout reactions at high momenta and high energy. The experimental facilities at the Thomas Jefferson National Accelerator Facility (JLab) provide the opportunity to probe such a kinematic regime in which short-range correlations are anticipated to provide a significant contribution to the measured cross-sections. Previous experiments [13, 16, 17] studying short-range correlations through the $(e, e'p)$ reaction have been limited by the beam energy, luminosity and the momentum transfer accessible by the available equipment.

This thesis describes the experiment, *Studying the Internal Small Distance Structure of Nuclei via the Triple Coincidence* $(e, e'pN)$ *Reaction* (E01015) [18] from Hall A at JLab. This experiment was motivated by a desire to search for short-range correlations through multi-nucleon knockout reactions. Data were taken for the $(e, e'p)$, $(e, e'pp)$ and $(e, e'pn)$ reaction channels simultaneously. This allows the fraction of $(e, e'p)$ events in which another nucleon was detected to be determined. The analysis for the single nucleon knockout channel is presented in this thesis. The $(e, e'p)$ cross-sections are measured in a kinematic regime which is expected to be dominated by short-range correlations. Chapter 2 describes the physics motivation for the experiment and the physics of the $(e, e'p)$ reaction channel being studied here. The experimental equipment and set-up are described in Chapter 3, while the necessary calibration measurements and corrections are discussed in Chapter 4. The methods used for analyzing the data are described in Chapter 5. The results are presented in Chapter 6 and final conclusions are drawn in Chapter 7.

Chapter 2

Physics Motivation

The short-distance repulsion of the nucleon-nucleon (N-N) interaction gives rise to physics beyond the IPSM, since the approximate Hamiltonian implicit in the IPSM does not include any residual interactions. In the context of this experiment and the physics motivating it, a short-range nucleon-nucleon correlation (SRC) refers to pair of nucleons with strongly overlapping wavefunctions. In a simple picture of this configuration, the nucleon pair has a large relative momentum[1]. In the impulse approximation, a virtual photon is absorbed by one nucleon of the pair, knocking it out of the nucleus. To conserve momentum, the untouched partner nucleon must recoil with its initial momentum and is ejected from the nucleus. This concept is illustrated in Fig. 2-1. The relative weakness of the electromagnetic interaction compared with hadronic interactions makes this simple reaction mechanism possible. If a hadronic probe were used instead of an electron, the reaction mechanism would be much more complicated because of multiple strong interactions of the probe with nucleons in the target.

This experiment [18] was motivated by a desire to study short-range correlations in a conducive kinematic regime - large momentum transfer, large recoil momenta and large excitation energy of the residual system - based on what was learned from previous experiments [17, 19, 20, 21]. An overview of previous results and their

---

[1] In reality, as well as a large relative momentum, the nucleon pair also has a low energy and so is significantly off-shell making the interaction more complicated

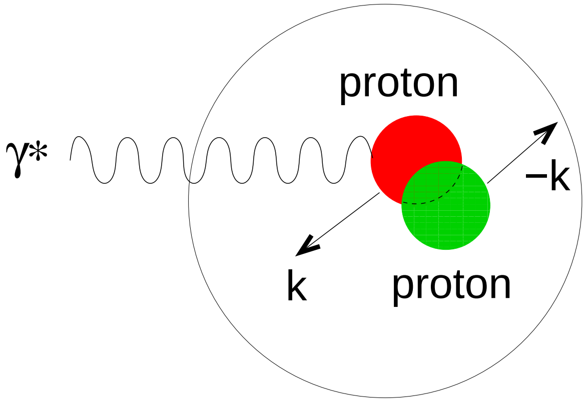

Figure 2-1: An illustration of the nucleon-nucleon short-range correlation, with the virtual photon being absorbed by one nucleon which is subsequently knocked-out of the nucleus. Momentum conservation leads to the partner nucleon recoiling with sufficient momentum to be ejected as well when the relative momentum is large compared with the Fermi momentum, k_f.

influence on the motivation for this experiment is presented here. An overview of the $(e, e'p)$ reaction and the kinematic details of this experiment are provided as well.

2.1 Inclusive (e, e') Experiments

Inclusive electron scattering, A(e, e'), where only the scattered electron is detected, is the simplest electron-nucleon scattering process to study. An experiment performed in Hall B at JLab [2] measured the inclusive cross-section ratios of various nuclei relative to ^3He, as a function of the Bjorken-x variable, x_B[2]. Since SRC arise from the localised behaviour of nucleons, their influence should be similar for different nuclei. This is an example of *scaling*. The cross-section ratios, shown in Fig. 2-2, all show two flat regions where they scale; $1.5 < x_B < 2$ indicative of two-nucleon SRC (since at least two nucleons must contribute) and $x_B > 2.25$ indicative of three-nucleon SRC (since at least three nucleons must contribute). These results are consistent with theoretical expectations [22, 23] of two-nucleon SRC dominance at nucleon momenta above 300

---

[2] Bjorken-x is the fraction of the nucleon's longitudinal momentum which is carried by the struck quark; for a nuclear target, x_B can vary from 0 to A (nuclear mass number) since there are more than one nucleon present from which the knocked-out nucleon can take momentum. Thus, $x_B > 1$ indicates more than one nucleon contributes to the reaction, while $x_B > 2$ indicates more than two nucleons contribute etc.

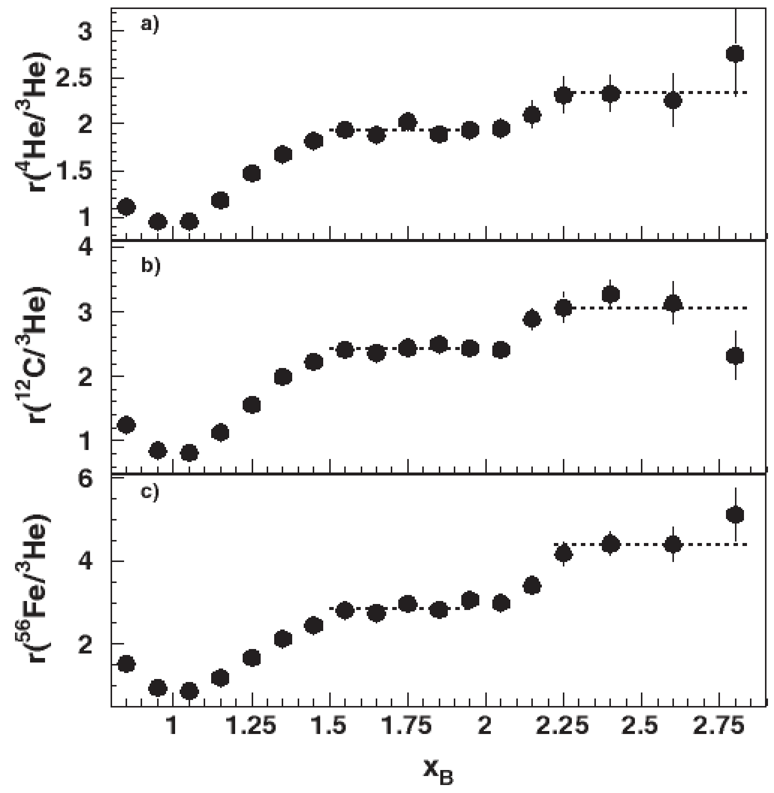

Figure 2-2: The results from a Hall B (JLab) inclusive (e, e') experiment; the cross-section ratios of ^{56}Fe, ^{12}C and ^{4}He relative to ^{3}He as a function of x_B are shown. Figure reproduced from [2].

MeV/c and three-nucleon SRC dominance above 500 MeV/c. This experiment also showed that SRC could be probed at kinematics with a large momentum transfer from the incident electron beam and $x_B > 1$.

2.2 Semi-Inclusive $(e, e'p)$ Experiments

The role of short-range correlations can be investigated through the semi-inclusive A$(e, e'p)$ reaction in which the scattered electron and knocked-out proton are detected in coincidence. By measuring the momenta and energies of the scattered electron and knocked-out proton involved in the reaction, the initial state of the knocked-out proton can be reconstructed; this assumes a simple final state and that the reaction mechanism is one-body—i.e. there are no competing two-body effects. If this proton was part of a short-range correlation, then the measured momentum distributions and spectral function[3] should have a larger strength at higher momenta and energies than predicted by the shell model.

A study of quasielastic electron scattering from ^3He was carried out in Hall A at JLab at large momentum transfer [3, 24]. Competing two-body effects such as meson exchange currents (MEC) and isobar configurations (IC), which can mask the correlation effects, can be suppressed using a large four-momentum transfer Q^2 and $x_B > 1$ (see [25, 26] for a discussion). In this experiment, $Q^2 \sim 1.5$ (GeV/c)^2 and $x_B \sim 1$ were used. A broad peak in the cross-section as a function of energy was observed to shift to higher energy at higher momentum values as shown in Fig. 2-3. This behaviour is consistent with a simple reaction mechanism picture in which the struck proton was part of a nucleon-nucleon pair with equal and opposite momenta $\pm\vec{p}_c$, in their center-of-mass. If the other nucleons present are assumed to be spectators at rest, then the struck proton is knocked-out with momentum $\vec{q} - \vec{p}_c$ and the partner nucleon recoils with momentum $\vec{p}_c$. The spectator nucleons and the undetected recoiling partner nucleon constitute a residual system with a mass given by,

$$M_{recoil}^2 = [M_{spec} + \sqrt{m_N^2 + p_c^2}]^2 - p_c^2 \tag{2.1}$$

where M_{spec} is the mass of the (A-2) spectator nucleons and m_N is the mass of the recoil partner nucleon. Since the missing energy is given by,

$$E_m = M_{recoil} + m_p - M_{target} \tag{2.2}$$

the position of the cross-section peak as a function of missing energy depends on the nucleon pair center-of-mass momentum $\vec{p}_c$. This simple picture provides a clear signature for processes involving two nucleons and a spectator nucleus; see Fig. 2-3.

A similiar experiment has been performed in Hall C at JLab [27] by Danielle Rohe and collaborators. In this experiment, electrons were scattered from carbon in

---

[3] The spectral function, usually denoted $S(k, E)$, is the probablity of finding a nucleon with momentum k and energy E in the nucleus.

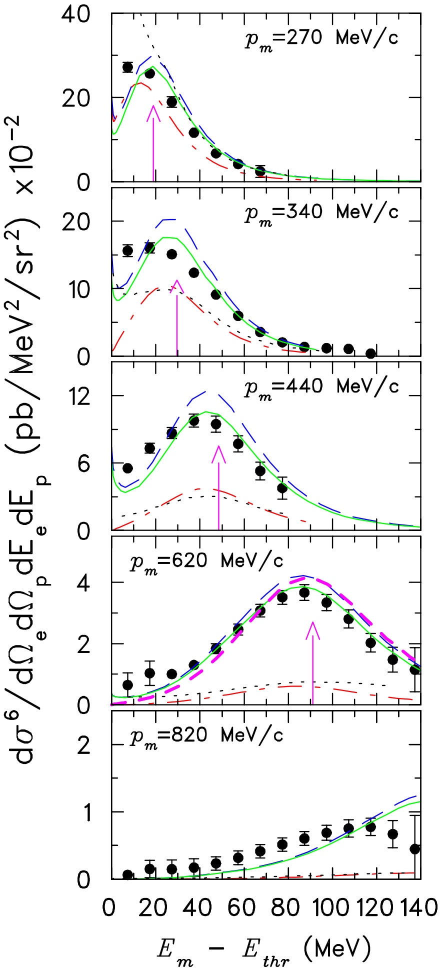

Figure 2-3: Cross-section results from $^3He(e, e'p)pn$ reaction. The vertical arrow gives the expected position for the disintegration of correlated nucleon-nucleon pairs; the peak location is reasonably well predicted at lower momentum values, but fails at the highest momentum shown. Figure reproduced from [3].

parallel kinematics[4], with large momentum transfer. The extracted spectral function was compared with a self-consistent Green's function theoretical calculation [4] in which the full structure of a nucleon-nucleon potential [28] was taken into account. The results are illustrated in Fig. 2-4, showing good agreement between theory and experiment at lower energy and momenta. However, at higher momenta this simple picture clearly fails. This shows that while short-range correlations may contribute to the spectral function strength at lower energy and momentum values, the contribution cannot be separated from the shell model piece. At higher energy and momentum values, the reaction cannot be described by a simple hard interaction between two nucleons.

---

[4] Parallel kinematics means that the initial nucleon momentum vector is parallel to the momentum transfer vector from the incoming electron.

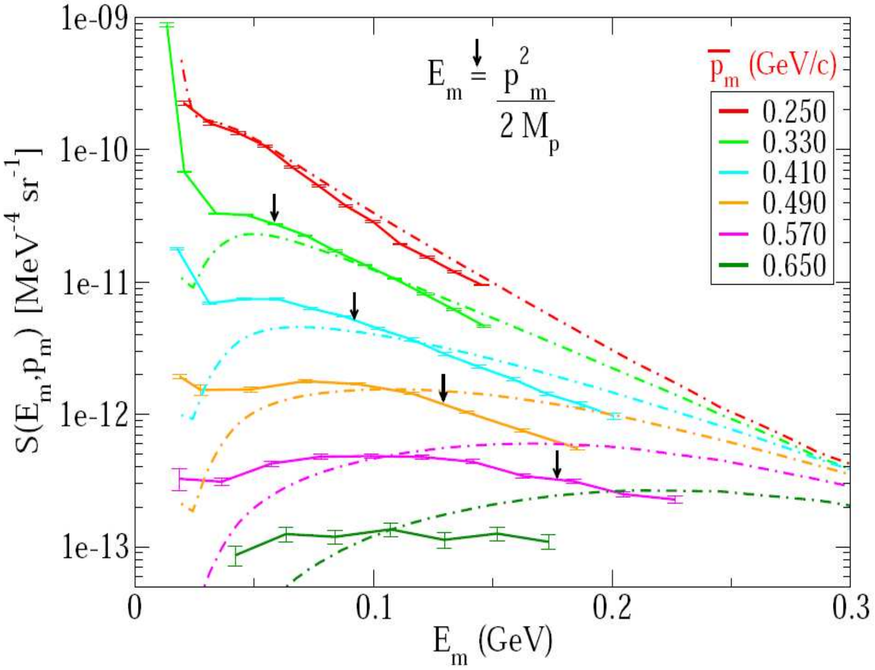

Figure 2-4: The experimental spectral function for ^{12}C (solid lines) for several different momenta. The vertical arrow gives the expected missing energy value for two nucleons being ejected from the nucleus. The dashed-dotted lines are the spectral functions predicted by a self-consistent Green's function theory calculation [4]. Figure reproduced from [5].

2.3 Multinucleon Knockout Experiments

Experiments in which more than one outgoing nucleons are detected in coincidence allow a direct probe of short-range correlations. If both nucleons from an initial state correlation are detected, then a directional correlation of their momenta should be observed. A triple coincidence measurement of the $^{12}C(p, 2pn)$ reaction was performed at Brookhaven National Laboratory by the *Eva* collaboration [21]. The experiment searched for proton-neutron correlated pairs and used an array of neutron detectors to detect the outgoing recoil partner neutron moving in the backward direction, in coincidence with the scattered and knocked-out protons. The results, shown in Fig. 2-5, show that for neutron momenta larger than the Fermi momentum in carbon ($k_F \sim 221$ MeV) [29], the protons and neutrons are emitted in preferential directions, such that their initial momentum vectors have a large angular separation up to a maximum of 180°, in which case the momentum vectors are in opposite directions. For measured neutron momenta below the Fermi momentum, Fig. 2-5 shows a random distribution of angles between the proton and neutron momentum vectors. This preferential directional correlation is a clear signature that the detected nucleons came from a short-range correlation pair, confirming that the pair should have a large relative momentum. This directional correlation is only observed when the initial state momenta of the nucleons in the pair are larger than the Fermi momentum of the target nucleus.

2.4 This Experiment

This experiment sought to investigate SRC in carbon through a triple coincidence $(e, e'pN)$ reaction as illustrated in Fig. 2-6. The Hall A high resolution spectrometers were used in their standard configuration to detect the scattered electrons and knocked-out protons from the $(e, e'p)$ reaction. A third spectrometer was added to this set-up for detecting the recoil partner nucleon. With the available equipment and beam energy at JLab, this experiment studied a kinematic regime (namely large Q^2 and $x_B > 1$) which previous experiments did not explore [1, 13, 19, 21, 3, 27]. Further details of the experimental equipment are provided in Chapter 3.

2.5 The $(e, e'p)$ Reaction

A short overview of the $(e, e'p)$ reaction formalism is presented here. The plane wave impulse approximation is introduced and the kinematic variables defined. The actual

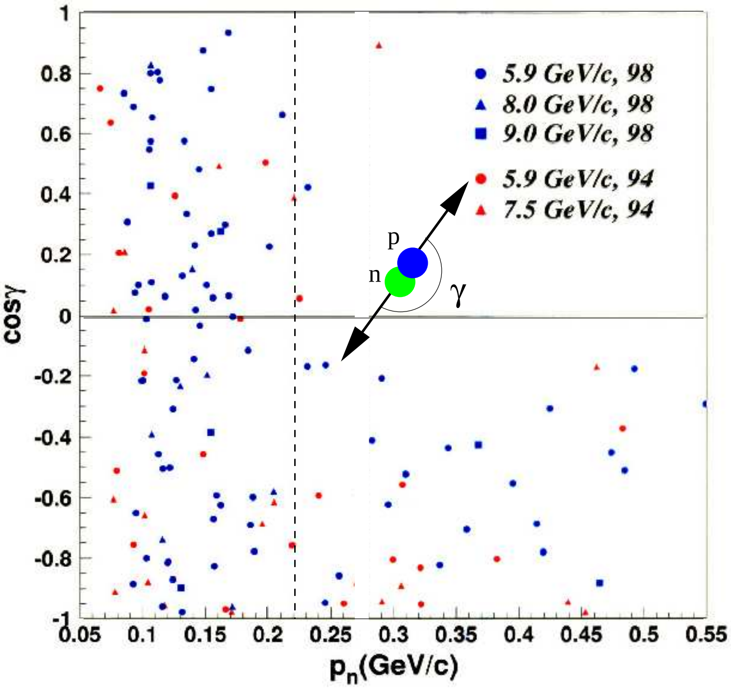

Figure 2-5: Results from the Eva collaboration $^{12}C(p,2pn)$ experiment at BNL. The scatter plot shows the cosine of the angle between the recoil neutron momentum and the scattered proton momentum, as a function of the neutron momentum. When the measured recoil neutron momentum is larger than the Fermi momentum in carbon (dashed line) the angle is always larger than 90°. This indicates a directional correlation between the momentum vectors of the proton-neutron pair.

kinematic settings used for data taking during the experiment are also provided.

2.5.1 Definition of Kinematic Variables

While this experiment was conceived to search for short-range correlations through a triple coincidence measurement, the kinematics are based on a semi-inclusive $(e,e'p)$ reaction. In such a reaction, the four-vectors of the participating particles are given by,

where the energy ω, and momentum $\vec{q}$, of the virtual photon are transferred from the incoming electron to the target nucleus and are thus given by,

$$\text{Energy transfer}: \quad \omega \quad = E_i - E_f \tag{2.3}$$

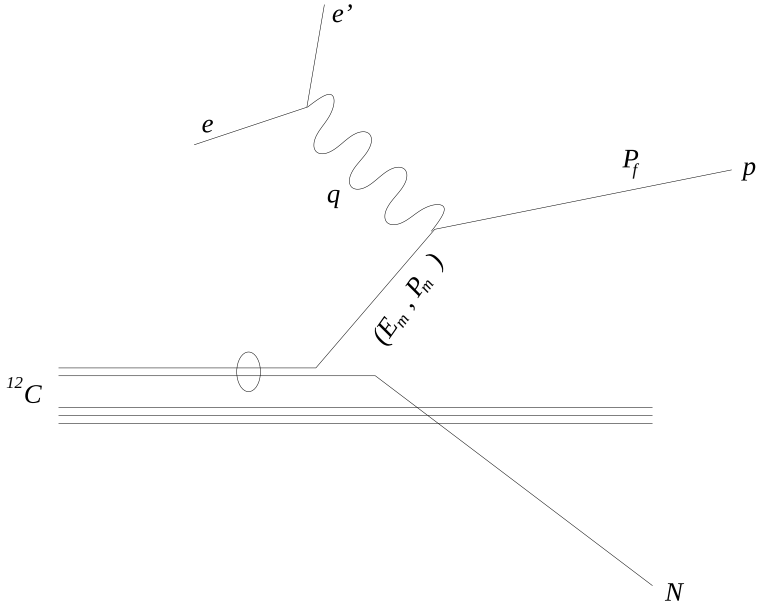

Figure 2-6: Feynman diagram showing the $(e, e'pN)$ reaction; the exchanged virtual photon is absorbed by a single proton.

Particle	4-vector
incident electron	$k_i = (E_i, \vec{k_i})$
scattered electron	$k_f = (E_f, \vec{k_f})$
target nucleus	$p_A = (E_A, \vec{P_A})$
detected proton	$p_p = (E_p, \vec{p_p})$
residual system	$p_B = (E_B, \vec{p_B})$
virtual photon	$q = (\omega, \vec{q})$

$$3 - \text{momentum transfer}: \quad \vec{q} \quad = \vec{k_i} - \vec{k_f} \tag{2.4}$$

The corresponding four-momentum transfer from the virtual photon to the target nucleus is,

$$q = k_i - k_f \tag{2.5}$$

from which we define Q^2 such that,

$$Q^2 = -q^2 = |\vec{q}|^2 - \omega^2 \tag{2.6}$$

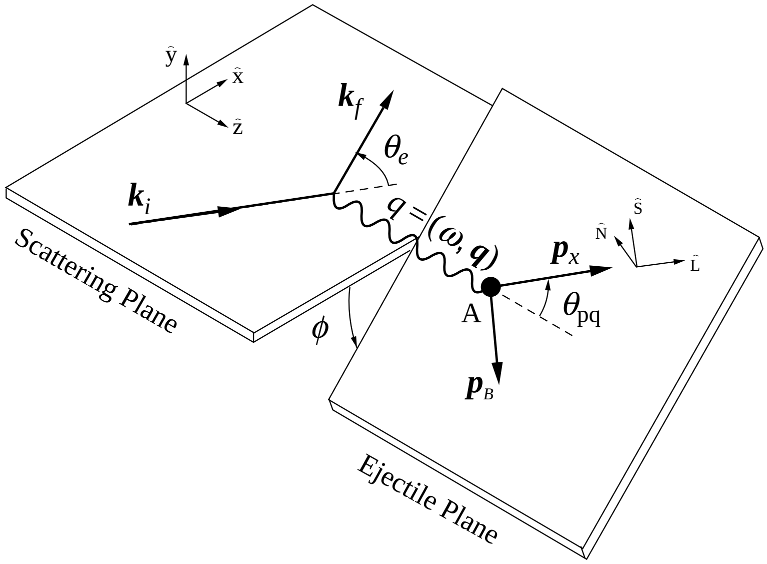

Figure 2-7: The semi-inclusive $(e, e'p)$ reaction and the associated kinematic variables; figure courtesy of [6].

These vectors are illustrated in Fig.2-7 [5] The scattering plane is defined as the plane containing both the incident and scattered electron vectors, $\vec{k_i}$ and $\vec{k_f}$. The ejectile plane is similarly defined as the plane containing the momentum transfer and scattered proton momentum, $\vec{q}$ and $\vec{p_p}$. In $(e, e'p)$ experiments, the momenta of the incident and scattered electrons and the knocked-out proton are all measured. In the laboratory reference frame, the target nucleus is assumed to be at rest so $p_A = (M_A, 0)$ where M_A is the target mass. In this experiment, the electrons are *ultrarelativistic* allowing their mass to be neglected such that $E_i \approx |\vec{k_i}|$ and $E_f \approx |\vec{k_f}|$.

The conservation of momentum at the reaction vertex leads to the definition of missing momentum as the momentum of the undetected residual nuclear system,

$$\text{Missing momentum} : \vec{p}_m \equiv \vec{p_B} = \vec{q} - \vec{p_p} \tag{2.7}$$

Note, some authors define missing momentum with the opposite sign convention – $\vec{p_m} = -\vec{p_B}$. The missing energy gives the excitation energy of the residual system and is defined as,

---

[5] In Fig. 2-7, the 4-vector for the scattered proton is p_x which corresponds to the 4-vector p_p defined in Table 2.5.1.

$$E_m = \omega - T_p - T_B \tag{2.8}$$

where T_p and T_B are the kinetic energies of the ejected proton and the residual system. Then writing out the kinetic energy terms explicitly, we have,

$$E_m = \omega - (\sqrt{\vec{p}_p^{\,2} + m_p^2} - m_p) - (\sqrt{\vec{p}_m^{\,2} + M_B^{*2}} - M_B^*) \tag{2.9}$$

where the M_B^* takes account of any excitation and other unobserved energies of the residual system. Conservation of energy at the reaction vertex leads to,

$$\begin{aligned} \omega + M_A &= E_f + E_B && (2.10) \\ &= m_p + T_p + M_B^* + T_B && (2.11) \\ \omega - T_p - T_B &= m_p + M_B^* - M_A && (2.12) \end{aligned}$$

Rewriting the residual mass in terms of energy and momentum and then using the conservation of energy gives,

$$\begin{aligned} M_B^* &= \sqrt{E_B^2 - \vec{p}_m^{\,2}} && (2.13) \\ E_B &= \omega + M_A - E_f && (2.14) \\ M_B^* &= \sqrt{(\omega + M_A - E_f)^2 - \vec{p}_m^{\,2}} && (2.15) \end{aligned}$$

Substituting back into eqn. 2.9 and rearranging gives the missing energy as,

$$E_m = m_p - M_A + \sqrt{(\omega + M_A - E_f)^2 - \vec{p}_m^{\,2}} \tag{2.16}$$

This expression for missing energy does not require any knowledge of the residual system. Since we have also used conservation of energy in subsituting for M_B^* then it also includes any binding energy lost in removing a proton from the target nucleus.

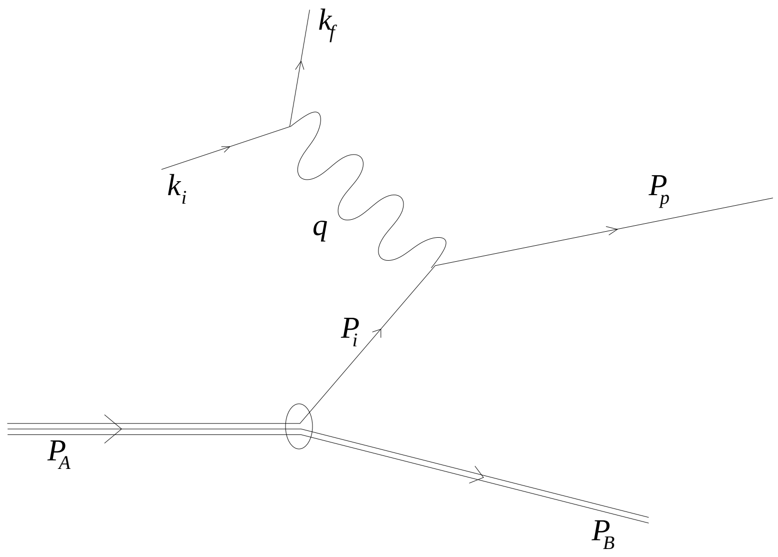

Figure 2-8: Feynman diagram showing the $(e, e'p)$ reaction in the plane wave impulse approximation.

2.5.2 The Plane Wave Impulse Approximation

The plane wave impulse approximation (PWIA) is a simple model for the $(e, e'p)$ reaction which assumes that the interaction is mediated by exchange of a single virtual photon, radiated by the scattered electron, which is absorbed by a single proton in the nucleus. It is this proton which is knocked-out of the nucleus and detected. The PWIA does not account for any final state interactions (for example, a rescattering of the struck proton by another nucleon) which the knocked-out proton may have as it exits the nucleus. This process is illustrated in Fig. 2-8 which shows the initial proton momentum, $\vec{p_i}$ is given by,

$$\vec{p_i} = \vec{p_p} - \vec{q} \tag{2.17}$$

By comparison with the definition of missing momentum in eqn. 2.7, the initial proton momentum is simply the opposite of the missing momentum vector; i.e. $\vec{p_i} = -\vec{p_m}$. Therefore, in the PWIA the initial proton momentum inside the nucleus before it was struck can be determined.

In the PWIA, the $(e, e'p)$ scattering cross-section is given by [30]

$$\frac{d^6\sigma}{d\Omega_e d\Omega_p dE_e dE_p} = p_p \, E_p \, \sigma_{ep} \, S(\vec{p_m}, E_m) \tag{2.18}$$

where σ_{ep} is the single nucleon off-shell cross-section. In the data analysis, the σ_{cc2} prescription of DeForest [30] is used for the single nucleon off-shell cross-section. The $sigma_{cc2}$ prescription is a current conserving offshell extrapolation of the on-shell nucleon current obtained from the Dirac equation for relativistic scattering interactions. This prescription includes explicitly the four-momentum transfer in the nucleon current calculation; further details are given in [30]. S$(\vec{p}_m, E_m)$ is the spectral function and is the probability of finding a proton in the nucleus with momentum p_m and energy E_m.

2.6 Kinematics for this Experiment

With the primary goal of this experiment to investigate short-range nucleon-nucleon correlations, the kinematics for data taking were chosen to minimise competing effects such as MEC, IC and FSI. Previous experiments [1, 13, 19, 21, 3, 27] have shown that kinematics with a large Q^2 value and $x_B > 1$ are preferred to probe SRC. Data taken over a large range of missing momenta values above the Fermi momentum ($|\vec{p}_m| > 221 MeV/c$) was desired to investigate the evolution of the experimental momentum distributions.

For this experiment, data was taken at a single beam energy of 4.63 GeV; the scattered electrons detected in the Hall A electron spectrometer which was set at a fixed momentum and scattering angle. By fixing the electron kinematics, the momentum transfer was $|\vec{q}| = 1.66$ GeV/c and the energy transfer was $\omega = 0.865$ GeV. This corresponds to $Q^2 \simeq 2$ (GeV/c)^2 and $x_B \simeq 1.23$. By choosing kinematics with $x_B > 1$, contributions from isobar configurations are reduced as the data is taken further from the Δ-resonance peak. This large value of Q^2 will also reduce meson exchange currents which (in some models) have a Q^{-2} dependence [25, 26]. There were three different proton kinematic settings used during the experiment, each one corresponding to an increasing missing momentum vector which was directed into our third spectrometer. The kinematics are simply denoted as I, II and III for ease of notation and are summarised in Table 2.1; a diagram of the kinematic settings is shown in Fig. 2-9.

KIN	Electron Arm		Proton Arm		P_{miss} range
	$\frac{\theta_e}{deg}$	$\frac{\vec{k_f}}{MeV/c}$	$\frac{\theta_p}{deg}$	$\frac{\vec{p_p}}{MeV/c}$	MeV/c
I	19.5	3762	40.1	1450	200-450
II	19.5	3762	35.8	1420	300-550
III	19.5	3762	32.0	1360	400-650

Table 2.1: The three kinematic settings used during this experiment. The electron spectrometer was unchanged, but the proton spectrometer was changed to map out a wider range of missing momentum.

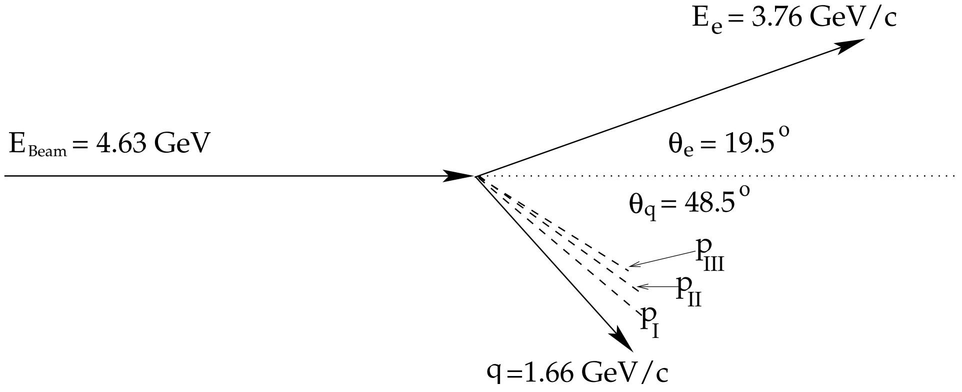

Figure 2-9: Diagram showing the kinematic settings used in the experiment. Note the three proton momentum vectors correspond to the three kinematics given in Table 2.1.

Data for the $^{12}C(e,e'p)^{11}B$ reaction are only present in the first kinematic; the second and third kinematic settings accepted the $^{12}C(e,e'p)$ continuum data only. The $^{12}C(e,e'p)^{11}B$ cross-section and distorted momentum distribution are extracted only for kinematic I. The $^{12}C(e,e'p)$ continuum cross-sections and distorted spectral functions are extracted for all three kinematic settings. The analysis of the triple coincidence reactions $^{12}C(e,e'pp)$ and $^{12}C(e,e'pn)$ are the subject of theses from Ran Shneor [11] and Ramesh Subedi [10] respectively. The analysis of the double coincidence $^{12}C(e, e'p)$ reaction presented in this thesis allows the cross-section evolution in missing momentum and missing energy to be studied in a kinematic regime where SRC are expected to be dominant. The results will provide guidance for theorists to improve their models of the nuclear wavefunction.

Chapter 3

Experimental Setup

This experiment (E01015) was performed at the Thomas Jefferson National Accelerator Facility (JLab), formerly known as CEBAF (Continuous Electron Beam Accelerator Facility). JLab is located in Newport News, Virginia and is a state-of-the-art facility featuring an electron accelerator, three experimental halls (A, B and C), a free electron laser and an applied research center. The experiment took data in Hall A from January through April 2005 utilising the two high resolution spectrometers present in Hall A and a third, larger acceptance spectrometer called *BigBite*. In this chapter, an overview of all the experimental apparatus is given. Further detailed information on both JLab and Hall A can be found in [31, 32]. A full review of the electron accelerator is provided in [33].

3.1 Electron Accelerator Overview

Originally approved in 1983, construction on JLab began in earnest in 1987, with the first experimental data being taken in 1995. JLab was built with the primary goal being to probe the nucleus and study the underlying quark structure of the nucleon. The accelerator can deliver a high energy[1] (up to 6 GeV — sufficiently high that the electron wavelength is a few percent of the nucleon size), high polarisation

---

[1] The electron beam energy at JLab is much higher than other electron accelerators such as those at NiKHEF and Mainz, allowing new kinematic regimes to be studied.

(> 70%), continuous wave electron beam to each of the three experimental halls simultaneously. Cryogenically cooled, superconducting, radio frequency (RF) cavities are used to accelerate the beam

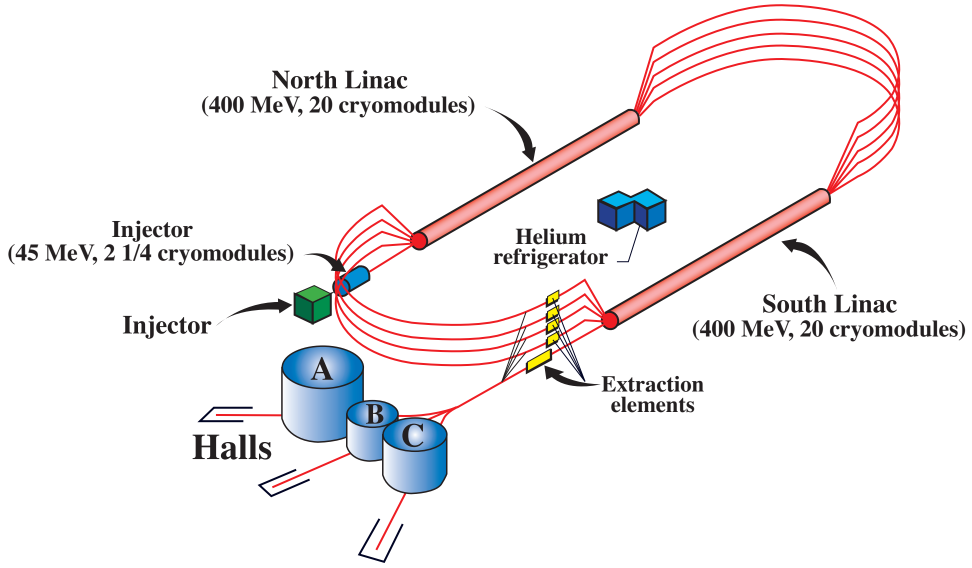
North Linac
(400 MeV, 20 cryomodules)
Injector
(45 MeV, 2 1/4 cryomodules)
Helium
refrigerator
Injector
South Linac
(400 MeV, 20 cryomodules)
A
B
C
Halls
Extraction
elements

Figure 3-1: An illustration of the Continuous Electron Beam Accelerator Facility (CEBAF), showing the two accelerating linacs, the recirculating arcs and the three experimental halls, A, B and C.

The layout of the accelerator is illustrated in Fig. 3-1. It is built 10m underground on an old seabed. As shown, the accelerator consists of two straight sections (the north and south linacs) which are joined by two arcs resulting in the *racetrack* design. The electrons used are produced at the injector by photo-emission from a gallium arsenide (GaAs) *superlattice* photocathode by illuminating it with laser-light of 780 nm wavelength from a titanium-sapphire laser [34]. The superlattice consists of thin layers of GaAs which have a lattice mismatch, inducing strain in the structure. The superlattice has a higher quantum efficiency (more electrons emitted per incident photon) and produces a higher polarisation than the previous strained GaAs cathode. The electrons are then accelerated to 45 MeV in the injector, before being directed into the accelerator at the north linac.

Each linac consists of twenty cryomodules, with each cryomodule containing eight superconducting niobium cavities. The accelerating niobium cavities are cooled by liquid helium to 2K. The two linacs are joined by two recirculating arcs. At the start of each arc, the electron beam can be separated according to the electrons energy. The first arc at the end of the north linac can separate the beam into five energies, while the arc at the end of the south linac can do so into four energies. This means that the electron beam can be accelerated through both linacs up to a total of five times. In each pass through both linacs, the beam can be tuned to gain up to 1.2 GeV per pass, resulting in a maximum deliverable beam energy of 6 GeV into the experimental halls. It is testament to the design and construction of the accelerator, that the 6 GeV beam far exceeds the original design goal of a 4 GeV electron beam. At the end of each pass through the accelerator, the beam can either be directed into one of the experimental halls or recirculated again through the accelerator. For the first four passes through the accelerator, a beam of a particular energy can be provided to only one of the halls. The fifth and final pass can be delivered simultaneously to all three halls.

Although this experiment did not require polarised beam, the electron beam delivered to hall A was polarised at $\sim$ 85%. The experiment used fourth-pass beam, with an energy of 4.6 GeV, with the beam current ranging from 5 - 40 μA.

3.2 Hall A Overview

With a diameter of 53 m and height of 20 m, Hall A is the largest of the three experimental halls. The main experimental equipment in the hall are the two High Resolution Spectrometers (HRSs) which are designed to detect charged particles of a desired momentum within ±4.5%. Before the electron beam is incident on the target in the hall, it passes through several different transport elements along the beamline. These elements are used to aid the transport of the beam onto the target and to measure the polarisation, energy, current and position of the incident beam. The target is located at the centre of the hall inside a cylindrical aluminium scattering chamber, which is kept under vacuum. Each experiment may use several different targets, some for calibrations as well as some for physics investigation; a diagram illustrating the layout of equipment in the hall for this experiment is shown in Fig. 3-2. All the targets used in any particular experiment are assembled on a *target ladder* inside the scattering chamber which is remotely moved vertically, allowing different targets to be used with the incident beam. Most of the electrons in the incident beam do not interact with the target and are transported from the scattering chamber along another beam pipe to a shielded beam dump.

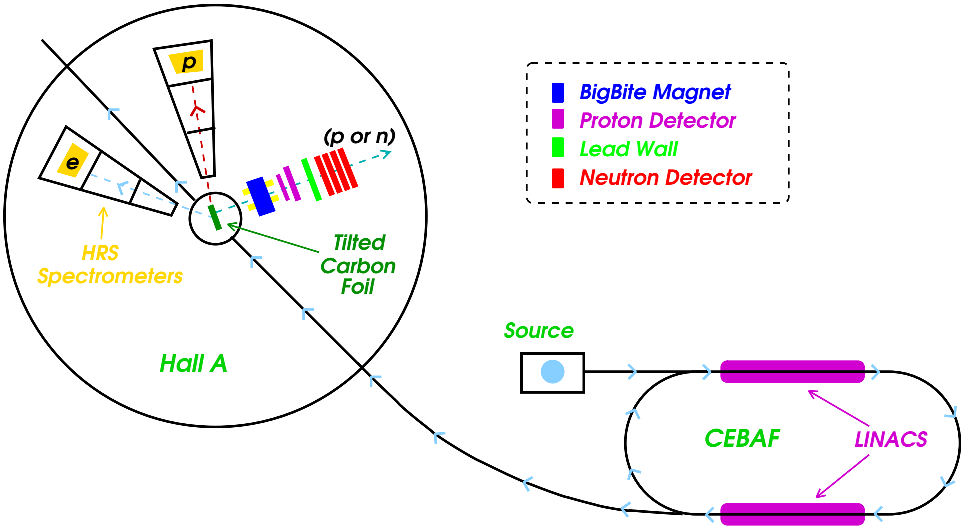

Figure 3-2: An illustration of the layout of Hall A during this experiment, showing the approximate locations of the spectrometers used. The accelerator diagram shown is not to scale.

Of the electrons which do interact with the target, some are scattered into one of the two high resolution spectrometers (HRS); some of the knocked out protons can be detected in the other HRS. Each HRS can be configured to detect either protons or electrons; however, for this experiment, electrons were detected in the left HRS and protons in the right HRS looking along the beam direction. The spectrometers are used to measure the momentum, trajectory, relative timing and particle identification of the particles they detect. Further detailed discussion of the HRSs is given later in this chapter.

3.3 Beamline Components

The beamline in hall A before the electrons are incident on the target, consists of a Compton polarimeter, a beam current monitor, a beam raster, the eP device, the Moller polarimeter and the beam position monitors.

The polarisation of the incident beam can be measured in both the Compton and Moller polarimeters. The Compton polarimeter provides a relatively non-invasive method of measuring the beam polarisation using Compton scattering. The polarization is determined by the measuring the counting rate asymmetry for opposite beam helicities in the scattering of circularly polarised photons by the electron beam. The Moller polarimeter utilises Moller scattering of polarised electrons off polarised atomic electrons in a magnetised foil to make an invasive (compared with Compton scattering) measurement of the electron beam polarisation. Although polarised beam was delivered by the accelerator during the experiment, it was not required and the Compton or Moller polarimeters were not used. However, further details on both polarimeters can be found in the literature [35, 36, 32].

The beam raster is used when currents above $5\mu A$ are incident on any of the liquid cryotargets to uniformly distribute the heat load over a larger area of the target. This helps to minimise target density fluctuations and any possible target boiling effects [37].

3.3.1 Beam Energy Measurement

The energy of the incident electron beam can be measured in two independent ways; an arc energy measurement and an eP measurement. The eP device is a stand-alone apparatus used to make an invasive measurement of the incident beam energy by measuring the angles of scattered electrons and protons in the elastic ${}^{1}H(e, e'p)$ reaction. This method was not used during this experiment, but more information can be found in the literature [38].

The Arc Energy Method

This method is based on the fact that an electron moves in a circular trajectory in a magnetic field. The radius of the trajectory depends on the magnitude of the magnetic field and the momentum of the electron. Therefore, the electron momentum can be determined by measuring the radius of the arc through which it is deflected by a known magnetic field. The deflection of the electron beam in the arc section of the accelerator beamline is used to determine the beam energy. The measurement can be made when the beam is tuned in either dispersive or non-dispersive mode in the arc section of the beamline. The electron beam momentum (p in GeV/c) is then found from the magnetic field integral of eight dipole magnets ($\int \vec{B} \cdot \vec{dl}$ in Tm) in the arc beamline and the resulting bend angle through the arc (θ in radians) by,

$$p = c\frac{\int \vec{B} \cdot \vec{dl}}{\theta} \tag{3.1}$$

where c = 0.299792 GeV rad / Tm ; the nominal bend angle is 34.3°. There are two measurements made to find the beam energy; the field integral of the eight magnets in the arc with respect to a reference magnet (the 9^{th} dipole) and the actual bend angle of the arc using a set of wire scanners. More details of the instrumentation can be found in [39].

The beam energy values used during the analysis are taken as the *Tiefenbach* values recorded in the data stream. The Tiefenbach value is calculated from the arc $B \cdot dl$ value and the beam position monitors in the hall, giving the launch and exit angles of the beam through the arc. The relative error on the Tiefenbach energy is less than 5×10^{-4}.

3.3.2 Beam Current Monitors

The current in the hall is measured by the Beam Current Monitor (BCM) which gives a stable, low-noise, non-invasive measurement. The BCM consists of an Unser monitor [40] sandwiched by two cylindrical RF cavities, with associated electronics;

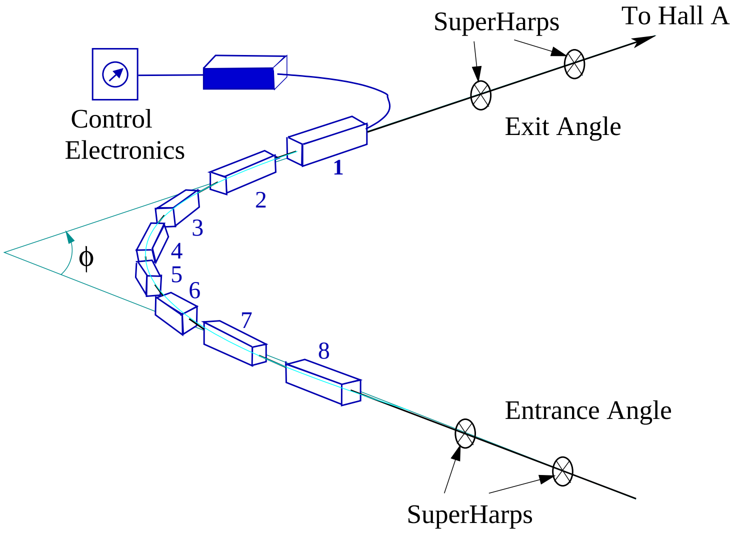

Figure 3-3: An illustration of the arc beamline section, showing the eight magnets used to deflect the beam.

it is located $\sim$ 25 m upstream of the target [41]. The Unser monitor is a parametric current transformer which is calibrated by passing a known current through an internal wire and provides an absolute reference. The nominal output is 4 mV/μA and the signal is readout by a multimeter attached to the Unser monitor. The RF cavities are tuned to the beam frequency (1487 MHz) resulting in output voltages proportional to the beam current. The output signals from the RF cavities are split in two, providing signals for sampled and integrated data.

One of the two signals is read by a high precision digital AC voltmeter which gives an average beam current measurement every second; this is the sampled data and is recorded in the data stream every 2 - 5 seconds, along with the signal from the multimeter connected to the Unser monitor. The other signal is transformed into an analog DC signal by an RMS-to-DC converter. The analog DC signal is converted to a frequency by a Voltage-to-Frequency converter and the resulting output is counted by VME scalers during each run; this gives a measure of the total charge accumulated in each run. The BCM system is shown in Fig. 3-4.

The output from the RMS-to-DC converter is linear for beam currents from 5 - 200 μA. In order to extend the linear range to lower currents, x3 and x10 amplifiers

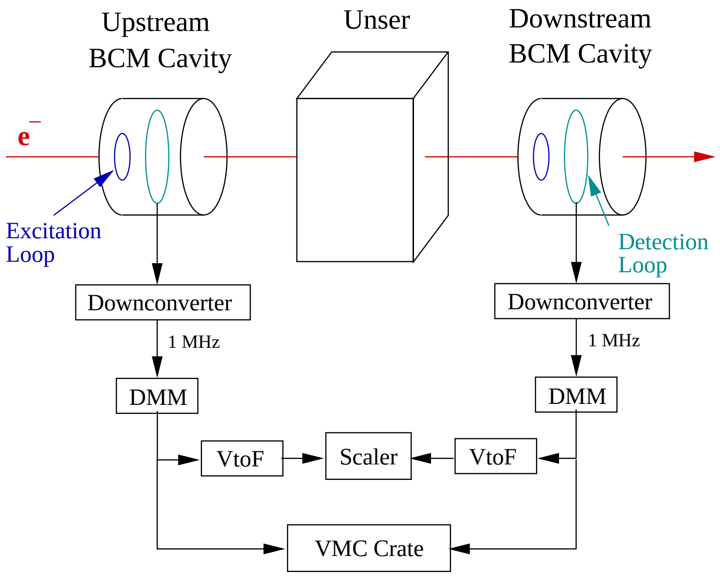
Upstream
BCM Cavity
Unser
Downstream
BCM Cavity
e⁻
Excitation
Loop
Detection
Loop
Downconverter
Downconverter
1 MHz
1 MHz
DMM
DMM
VtoF
Scaler
VtoF
VMC Crate

Figure 3-4: Diagram of the beam current monitor system.

have been added to the system. This means there are three amplified signals from each bcm, which are counted by scalers in both of the HRS spectrometers, giving a twelve-fold redunancy in the outputs for measuring the charge in each data taking run.

The scaler outputs are calibrated by stepping up the current up from zero to the maximum current through five or more cycles. Data is taken simultaneously to measure the charge accumulated in the scalers.

3.3.3 Beam Position Monitors

The position and direction of the beam at the target is determined using two Beam Position Monitors (BPM) located 7.524 m and 1.286 m upstream of the target. Each BPM consists of a cylindrical cavity housing four wires, parallel to the central axis of the beam. As the electron beam goes through the cavity, signals are induced in the wires with amplitudes inversely proportional to the distance of the wire from the beam. The beam position in the (X,Y) direction is found by combining the signals from pairs of wires with known calibration constants. The BPMs are calibrated using wire (harp) scanners located adjacent to each BPM and by performing a *bulls-eye* scan, putting the beam at known coordinates.

3.4 Target System

The cryogenic target system consists of a vertical assembly holding the liquid (or gas) cells and solid foil targets to be used in each experiment. This target *ladder* is mounted inside the scattering chamber and can be moved remotely in the vertical direction to intersect any of the targets with the beam.

In this experiment, the primary target was a carbon foil, whose normal was rotated at 70° with respect to the central axis of the incident beam, as shown in Fig. 3-5. The target was rotated in order to minimise the amount of material being traversed by the recoil partner nucleon ejected in each triple coincidence event. This was done to try and minimise any energy loss or multiple scattering the recoiling nucleon might have as it exited the target.

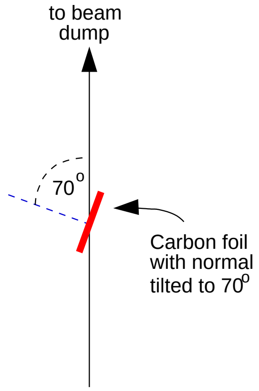

Figure 3-5: The primary carbon foil target was rotated by 70° relative to the beam axis as shown.

The target ladder included 4 cm and 15 cm long liquid hydrogen and liquid deuterium targets, a seven-foil carbon optics target, 4 cm and 15 cm long aluminium dummy targets, a beryllium oxide foil and another carbon foil; see Table 3.1 for more details. The liquid targets were contained within the *cigar tube* aluminium cylinders, shown in Fig. 3-6; these tubes have an inner radius of 20 mm. Elastic scattering from

Target	Thickness	Density
Tilted Carbon	0.25 mm	1.688 g/cm^3
Liquid Hydrogen	4 cm	0.073 g/cm^3
	15 cm	0.073 g/cm^3
Liquid Deuterium	4 cm	0.167 g/cm^3
	15 cm	0.167 g/cm^3
Optics - 7 carbon foils	1 mm each	1.73 g/cm^3
Carbon foil	1 mm	1.73 g/cm^3
4 cm Al dummy		
15 cm Al dummy		
Beryllium Oxide	1mm	

Table 3.1: A list of targets used during the experiment and their material properties.

the liquid hydrogen and deuterium targets was used to calibrate both the proton and neutron detectors in the third arm; further discussion is given in chapter 4.

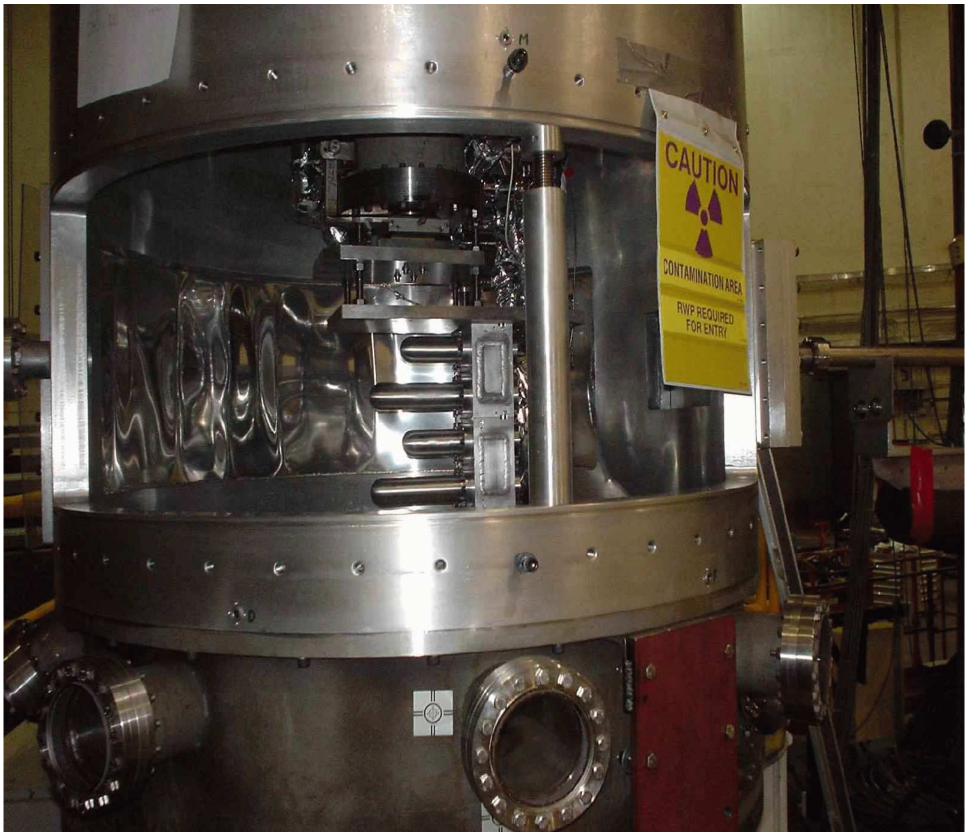

Figure 3-6: Photograph showing the target ladder inside the scattering chamber; the 4 cm and 15 cm *cigar tubes* containing liquid hydrogen and liquid deuterium can be easily seen, but the carbon foil target is out of view.

Since the BigBite spectrometer has a much larger acceptance than the HRSs (96 msr compared with 6 msr), a new scattering chamber with larger exit windows was required. Our collaborators from the University of Virginia secured funding from a Major Research Initiative grant to pay for this new chamber. The chamber was designed with the long term in mind, therefore it can be used with all of the standard equipment available in the hall. The new scattering chamber is illustrated in Fig. 3-7.

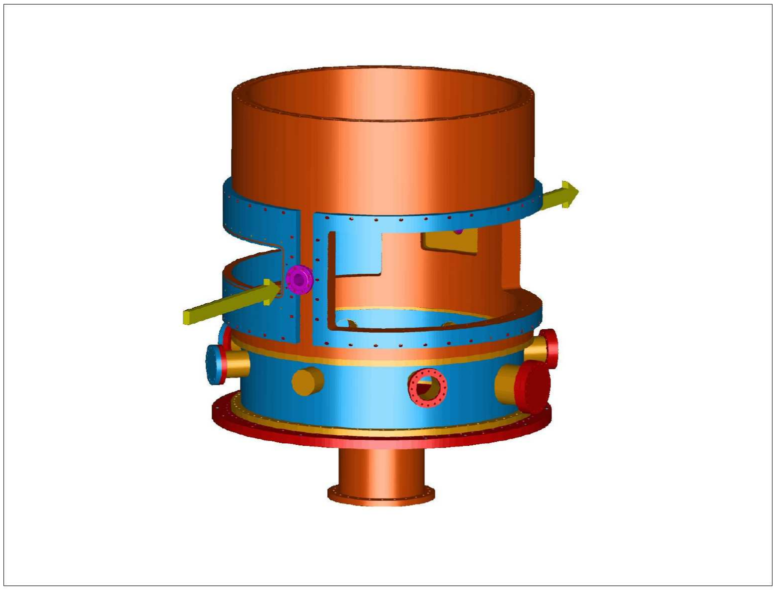

Figure 3-7: A 3D rendering of the new scattering chamber built for this experiment. Notice the large window opening to utilise the increased acceptance in BigBite.

3.5 Hall A High Resolution Spectrometers

The principal equipment in hall A is a pair of near identical high resolution spectrometers (HRS). The HRSs were designed to allow detailed study of nuclear structure, primarily through the $(e, e'p)$ reaction. As such, they have a momentum resolution of better than 2 x 10^{-4} and an in-plane angular resolution of better than 2 mrad at a maximum central momentum of 4 GeV/c.

Each HRS consists of four cryogenically cooled, superconducting magnets arranged sequentially as quadrupole-quadrupole-dipole-quadrupole (QQDQ). The magnets are held by a large steel gantry, with a concrete enclosure on top housing the detectors. The basic layout of each HRS is shown in Fig. 3-8. The first two quadrupole magnets provide a net overall focusing effect on the scattered particles entering the spectrometer. The dipole provides a 45° bend angle for the central ray through the acceptance, as well as net focusing at the entrance and exit polefaces; a field gradient within the dipole itself also contributes to the focusing. The third and final quadrupole magnet allows good horizontal position and angular resolution to be achieved. The main characteristics of the HRSs are given in Table 3.2 and further details on their design can be found in [32].

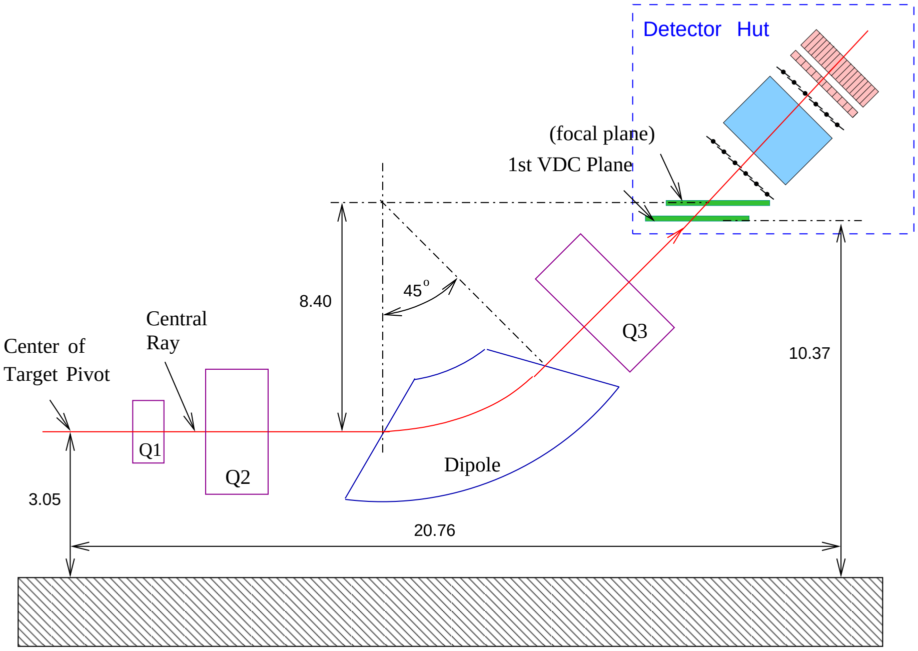
Detector Hut
(focal plane)
1st VDC Plane
8.40
45°
Central
Ray
Center of
Target Pivot
Q1
Q2
Q3
10.37
Dipole
3.05
20.76

Figure 3-8: A side-view schematic of one HRS, showing the quadrupole-quadrupole-dipole-quadrupole magnet arrangement and the location of the detectors; dimensions are given in meters.

Configuration	QQDQ
Bend Angle	45°
Optical Length	23.4 m
Momentum Range	0.3 $\sim$ 4.0 GeV/c
Momentum Acceptance $\delta P/P$	$\pm$4.5%
Momentum Resolution	1 x 10^{-4}
Angular Acceptance - Horizontal	$\pm$30 mrad
Angular Acceptance - Vertical	$\pm$60 mrad
Solid Angle, $\Delta\Omega$	$\sim$ 6 msr
Angular Resolution - Horizontal	0.6 mrad
Angular Resolution - Vertical	2.0 mrad

Table 3.2: The general characteristics of each Hall A HRS.

3.5.1 Detector Packages

In this experiment, the HRS on the left of the beamline was used to detect scattered electrons, while the HRS on the right of the beamline was used to detect knocked out protons. The polarities of the magnets and the detectors used can be customised for each experiment to detect negative or positively charged particles in either spectrometer. The detectors in each spectrometer are illustrated in Fig. 3-9 and are located inside the shielded detector hut at the top of each HRS.

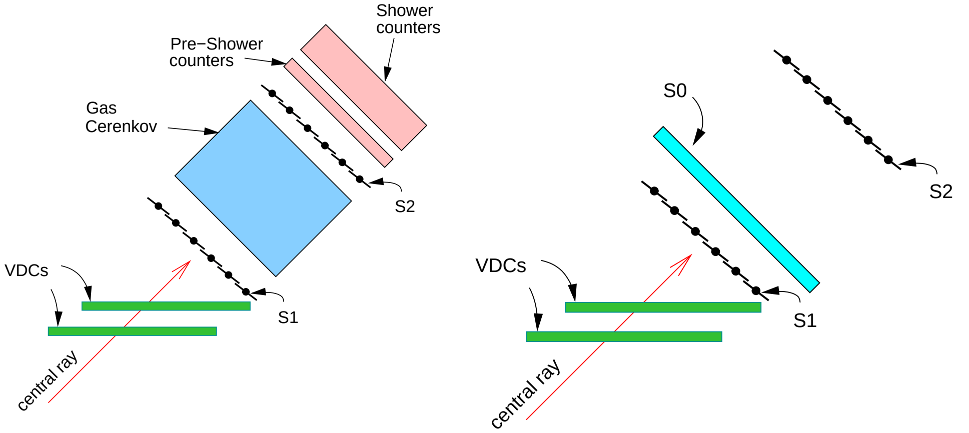

Figure 3-9: A side view of the detector stacks in each spectrometer, showing the detectors used; left figure is for the electron spectrometer; right figure is for the proton spectrometer.

Both detector stacks contain a pair of vertical drift chambers (VDCs) used for particle tracking and a pair of scintillator planes (S1 and S2) used to form the trigger for the data acquisition system. The electron detector stack also contained a gas cherenkov detector and a lead glass preshower-shower detector for particle identification. The hadron detector stack also included another scintillator detector, S0, used to generate auxiliary triggers. All of the detectors used are briefly described below.

Scintillator Planes

The S1 and S2 scintillator planes form the principal trigger system for events in each spectrometer. The S1 plane consists of six overlapping scintillator bars, while the S2 plane has sixteen scintillator bars; each bar has a photomultiplier tube (PMT) at each end of the bar. The scintillator bars in both the S1 and S2 planes are oriented perpendicular to the central ray, in the horizontal direction. The two planes are arranged perpendicular to the central ray through the spectrometer, meaning at an angle of 45° to the vertical. The active area of the S1 plane is 170 cm x 35 cm, while S2 has a slightly larger active area of 220 cm x 54 cm. In the right (proton) HRS, a third scintillator plane, S0 was included. This is a single scintillator bar, 10 mm thick, with an active area of 190 cm x 40 cm, with a 3 inch PMT at each end. The S0 plane was positioned directly behind the S1 plane, oriented such that its long edge was parallel to S1 (see Fig. 3-9). Details of each type of event trigger are given later.

Vertical Drift Chambers

Each detector stack contains a pair of identical vertical drift chambers (VDC) to provide charged particle track information [7, 42]. The VDCs are parallel to one another, in the horizontal plane, separated by 23 cm and are oriented at 45° to the central ray. Each VDC consists of two parallel planes of 20 μm-diameter, gold-plated tungsten wires, in a standard U-V configuration; the wires in successive planes are oriented at 90° to one another and at 45° to the projection of the central ray onto the wire plane, as illustrated in Fig. 3-10.

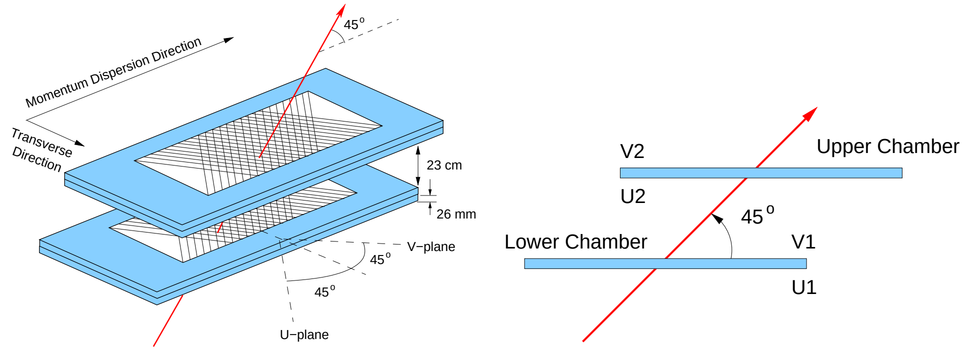

Figure 3-10: A diagram of the vdc wire planes showing the orientation of the wires relative to the central ray (left figure) and a side view of the vdc pair (right figure).

The individual wire planes are bounded by gold-plated mylar foil layers[2], at a nominal operating voltage ∼ -4 kV, while the wires are kept grounded. This creates the electric field between the wires and the mylar foils which accelerates electrons towards the wires, as shown in Fig. 3-11. The ionising gas is an argon-ethane gas mixture (62%/38% by weight) which flows between each cathode at ∼ 10 litres/hour. Charged particles passing through the VDC ionise the gas creating a trail of electrons and ions. These electrons drift along a path of least time to the wires (the geodetic path shown in Fig. 3-11). As the electrons approach the high field region around the wires, they are accelerated towards the wires, causing further ionisation and ultimately resulting in an electron avalanche. This avalanche induces an electrical signal (referred to as a *hit*) on the wire, which is then preamplified and sent to a time-to-digital converter (TDC). The TDC measures the drift time of the electrons from the original trajectory of the particle going through the VDC; this is then converted to a distance from the wire to the trajectory. Combining the drift distance for all wires fired allows the trajectory of the charged particle to be calculated. The resolution is improved by combining information from each of the four wire planes in each VDC pair to determine the particle trajectory; the resulting position resolution is ∼ 100 μm and angular resolution of ∼ 0.5 mrad.

---

[2] Three foil cathodes are used in each VDC with the central foil being double-sided providing a shared cathode between the U and V wire planes; the outer foils are single-sided.

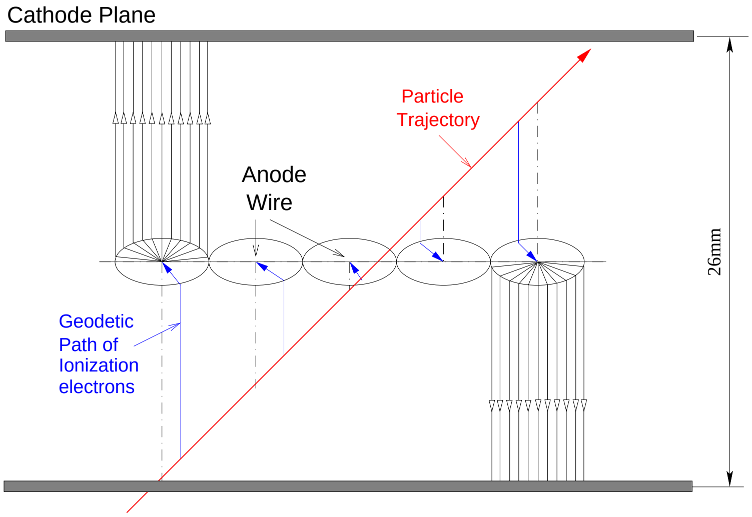

Figure 3-11: A typical particle trajectory through the VDC creates a *five-cell event*; i.e. the five wires closest to the trajectory register a hit. Also shown are the electric field lines between the wires and the cathode planes (mylar foils); the electrons drift along the path of least time - the geodetic path - and induce a signal in the wires [7].

Gas Cherenkov

A carbon-dioxide filled, threshold gas cherenkov detector was used in the electron spectrometer for particle identification and to generate auxiliary triggers. When a charged particle travels through a material with a velocity greater than the speed of light in that material (c/n where n is the material refractive index), Cherenkov light is emitted. The refractive index of the atmospheric CO_2 used is 1.00041, giving a threshold particle velocity and momentum of,

$$v_{th} = \frac{c}{n} \text{ and } p_{th} = \frac{mv}{\sqrt{1-\frac{v^2}{c^2}}} \approx \frac{mc}{\sqrt{2\alpha}} \tag{3.2}$$

where $\alpha = n - 1 << 1$. Thus, the threshold momentum for electrons to produce Cherenkov radiation is $\sim$ 17 MeV/c and $\sim$ 4.8 GeV/c for pions. Since the HRS has a momentum range of 0.3 $\sim$ 4.0 GeV/c, only electrons should emit Cherenkov light. The detector has ten spherical mirrors, each directing the emitted Cherenkov light on to a PMT. The gas cherenkov was mounted between the S1 and S2 scintillator planes and can be used to form a secondary trigger with either (or both) the S1 and

S2 detectors. Further details of the event triggers used in this experiment are given in Section 3.7.

Preshower-Shower Counters

A lead glass shower counter is also used for particle identification in the electron spectrometer. In a shower counter, detected light output is linearly proportional to the energy deposited by the incident particle. The distribution of energy in the detector is used to identify the particle; electrons will produce a large ADC signal, while hadrons will produce a low ADC signal. The separation of these two energy distributions allows the particles to be identified. The lead glass counter used in this experiment consists of two planes of blocks, referred to as the *preshower* and the *shower*. The two layers of blocks provide better particle identification than a single layer because the second layer can further differentiate the energy separation of particles detected in the first layer. The determination of particle identification efficiency is given in section 4.4.3. The preshower consists of 48 lead glass blocks, each 10 x 10 x 35 cm^3, with a single PMT attached to each block. The shower is located directly behind the preshower and consists of 80 blocks, each 14.5 x 14.5 x 35 cm^3. The blocks in the shower are oriented with their long edge along the direction of incident particles, as illustrated in Fig. 5-2.

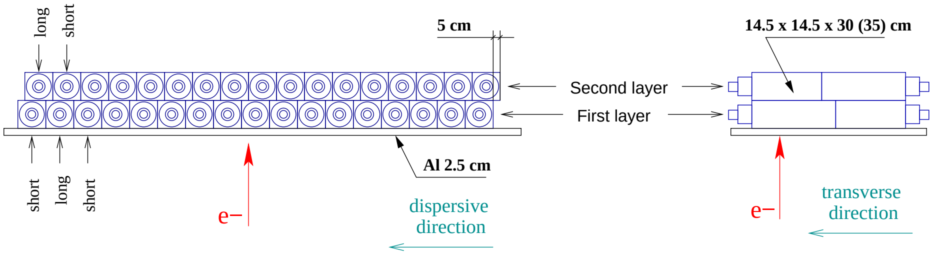

Figure 3-12: Diagram showing the preshower-shower detector used in the electron spectrometer for particle identification. Note, the transverse and dispersive directions in the figure refer to the coordinates in the spectrometer reference frame.

3.6 The BigBite Spectrometer

This experiment required a third spectrometer to be used in conjunction with the two HRSs in order to detect the recoil partner nucleon in the triple coincidence $^{12}C(e, e'pN)$ reaction. The BigBite spectrometer was constructed for this purpose and instrumented with proton and neutron detectors.

3.6.1 The BigBite Magnet

The central component of the spectrometer is a large acceptance, non-focusing dipole magnet. Originally designed and built for use at NiKHEF in the Netherlands [43, 44], the large pole-face gap (25 cm in the horizontal and 84 cm in the vertical directions) allows for a larger bite of scattered particles in the angular acceptance and hence the name, *BigBite*. In this experiment, the magnet was located 1.1 m from the target, resulting in a solid angle acceptance of $\sim$ 96 msr - some sixteen times larger than the nominal HRS acceptance. Although BigBite can provide a field strength of up to 1.2 T, for this experiment the magnet was energized to a field strength of 0.92 T - the same operating conditions used at NiKHEF. This means that a proton of momentum 500 MeV/c going through the center of the magnet would be bent at 25° above the horizontal (for positive polarity); see Fig. 3-13. This defines the central ray for BigBite. The magnet sweeps charged particles into the proton detector, while neutral particles are undeviated and travel straight through towards the neutron detector.

3.6.2 The Proton Detector

The proton detector used in this experiment consists of three layers of scintillator bars, arranged in two detectors, the *auxiliary* plane and the *trigger* plane. By design, the dimensions of the active area of these detectors matchs the acceptance of the BigBite magnet. Both detectors were mounted together in a single frame, separated by $\sim$ 1 m and rotated at 25° to the vertical, thus making them perpendicular to the central ray through the magnet; see Fig. 3-14. The time-of-flight between the auxiliary and trigger planes, as well as the pattern of hit bars in all layers, was used

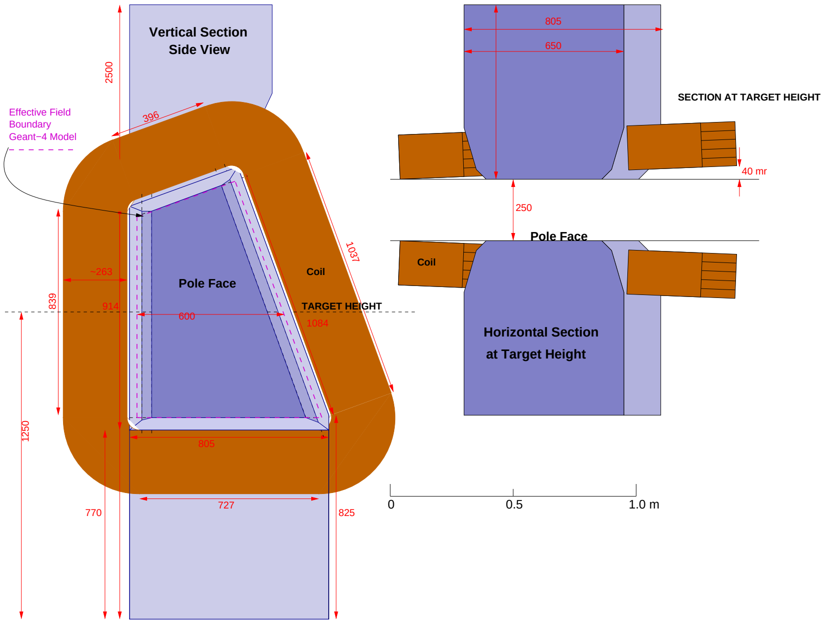
Vertical Section
Side View
2500
396
Effective Field
Boundary
Geant-4 Model
1037
Coil
Pole Face
~263
839
914
600
TARGET HEIGHT
1084
1250
805
727
770
825
805
650
SECTION AT TARGET HEIGHT
40 mr
250
Pole Face
Coil
Horizontal Section
at Target Height
0
0.5
1.0 m

Figure 3-13: A side view (left) and above view (right) of the BigBite magnet showing the magnetic field boundary and the large pole face gap.

to determine the particle track and momentum through BigBite. The magnet and proton detector were mounted on a custom built stand which could be rotated around the pivot in the hall through an angular range of $\sim 55° - 120°$.

The Auxiliary Plane

The auxiliary plane allows the proton momentum to be determined by measuring the time-of-flight of protons detected in it and the trigger plane. A secondary momentum determination can be made from the pattern of hit bars in both the auxiliary and trigger planes. The auxiliary plane is an array of 56 narrow scintillator bars, located at the rear field boundary directly behind the magnet. Each scintillator bar has dimensions 350 x 25 x 2.5 mm^3 and has a single PMT attached to one end; the PMTs for adjacent bars are actually on opposite sides of the detector frame. Each PMT is magnetically shielded by placing a thin mu-metal[3] sheath around the PMT

---

[3] Mu-metal is a nickel alloy (75% nickel, 15% iron, plus copper and molybdenum) with a very high magnetic permeability making it very effective at screening static or low-frequency magnetic fields.

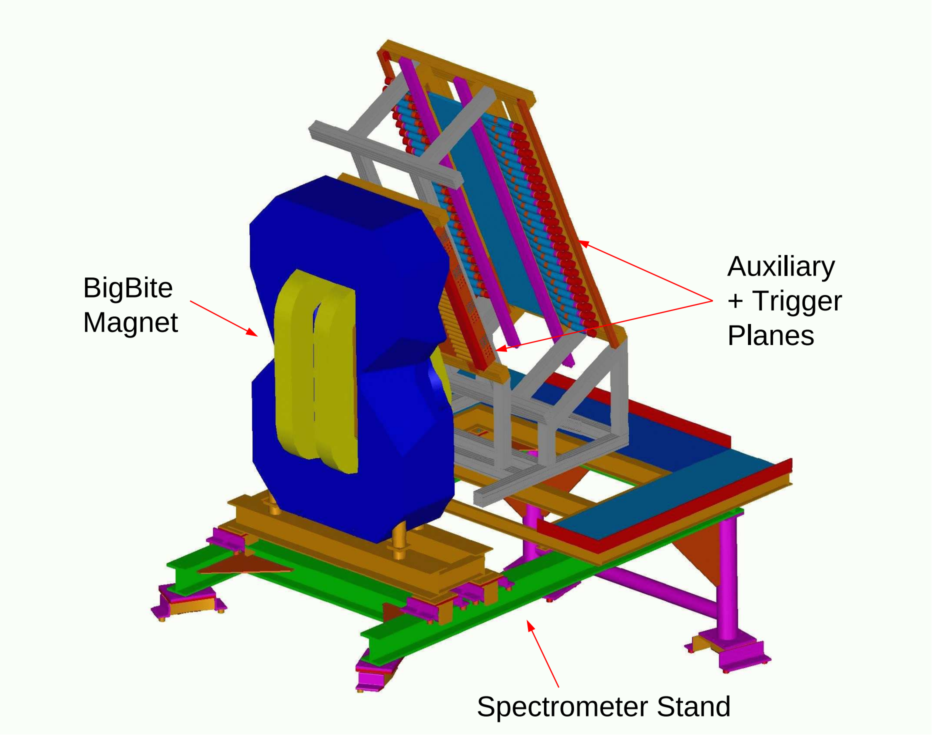

Figure 3-14: A 3D drawing of BigBite, showing the magnet and proton detector mounted together on the custom platform.

and then inserting both into a soft iron cylinder. The auxiliary plane was designed and constructed by our collaborators from Tel Aviv University and is illustrated in Fig. 3-15.

The Trigger Plane

The trigger plane consists of two individual layers of scintillator bars - the δE plane and the E plane - separated by 8 mm. Both layers comprise 24 scintillator bars, with those in the δE plane being 3 mm thick, while those in the E plane are 30 mm thick; the bars are 500 mm wide and 86 mm high (in the dispersive direction). The trigger plane is illustrated in Fig. 3-16. Each bar has a PMT attached to each end and these are enclosed by thin mu-metal cylinders for magnetic shielding. The scintillators in the δE plane are offset by one half bar (43 mm) compared with those in the E plane, thus improving the position resolution to ±43 mm. The trigger plane was designed by

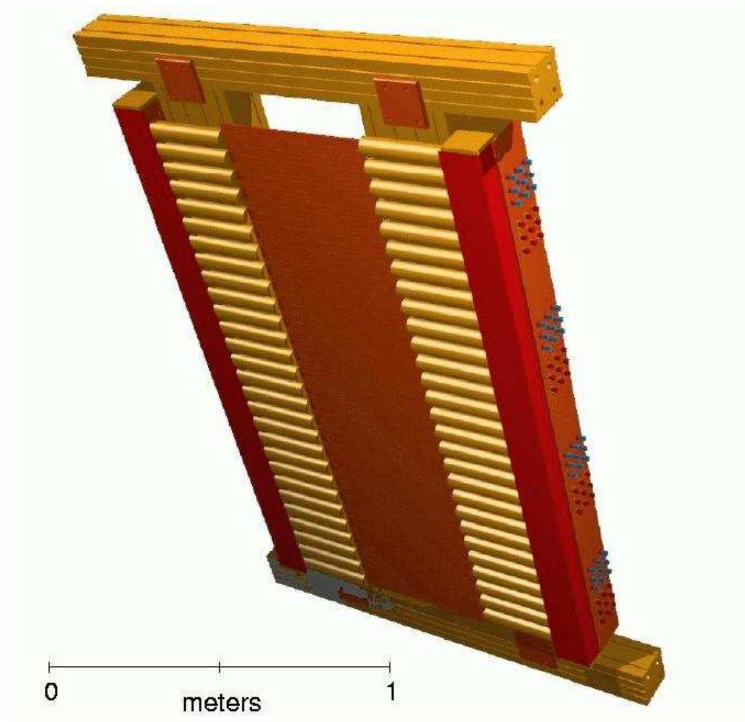

Figure 3-15: A 3D rendering of the auxiliary plane; notice that each scintillator bar has only one PMT.

our collaborators from Glasgow University and was constructed with their assistance at JLab.

3.6.3 The Neutron Detector

A large volume scintillator array was constructed for detecting recoil partner neutrons. It consists of four planes of scintillator bars, of varying heights, but constant thickness (10 cm) and width (1 m) with an active detection volume of 1 x 3 x 0.4 m^3; see Fig. 3-17. The dimensions of the neutron detector were chosen to match the acceptance of BigBite, with the detector placed 6 m from the target. Each scintillator bar had a PMT attached at each end. A special frame was designed to hold the planes of scintillator bars together in a single unit; an extruded aluminium material [45] was chosen for several reasons - strength, lightweight, ease of use. Working with the Hall A engineering design staff and the engineers at Aline Corporation, a suitable modular

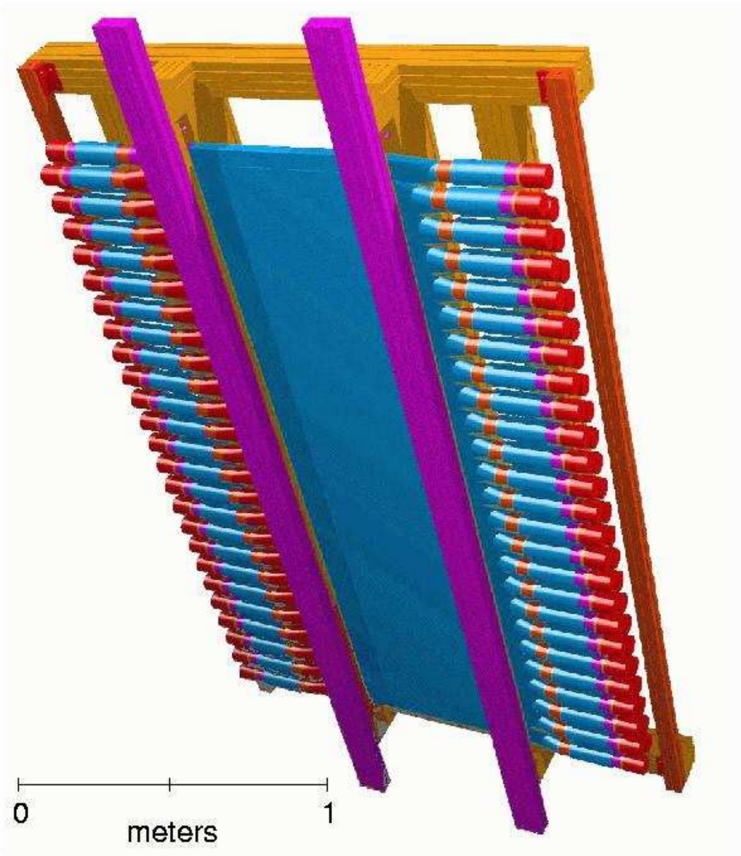

Figure 3-16: A 3D rendering of the trigger plane, showing the δE and E planes; each scintillator bar in both planes has two PMTs attached, one at each end.

frame was designed and test built at the supplier before being disassembled and the components shipped to JLab. The simplicity of the design and ease of assembly meant that the whole neutron detector could be built by a single person (me $\smile$). The frame was designed to have the scintillator planes as closely spaced as possible, while still maintaining a strong enough frame to safely contain all the bars; the final space between planes was only 50 mm. The complete detector weighed $\sim$ 6500 lbs.

A layer of 2 cm thick *veto* scintillator bars was arranged as shown in Fig. 3-17, in front of the first plane of scintillator bars, to detect charged particles and increase the neutron detection efficiency by allowing signals from charged particles to be removed from the data. Each veto bar was 70 cm wide with a single PMT attached at one end; two veto bars were overlapped by 30 cm to create a single row covering the 1 m active width of the scintillator bars. The veto bars were assembled in three overlapping sections to ensure that the whole active area of the first plane of the neutron detector was covered.

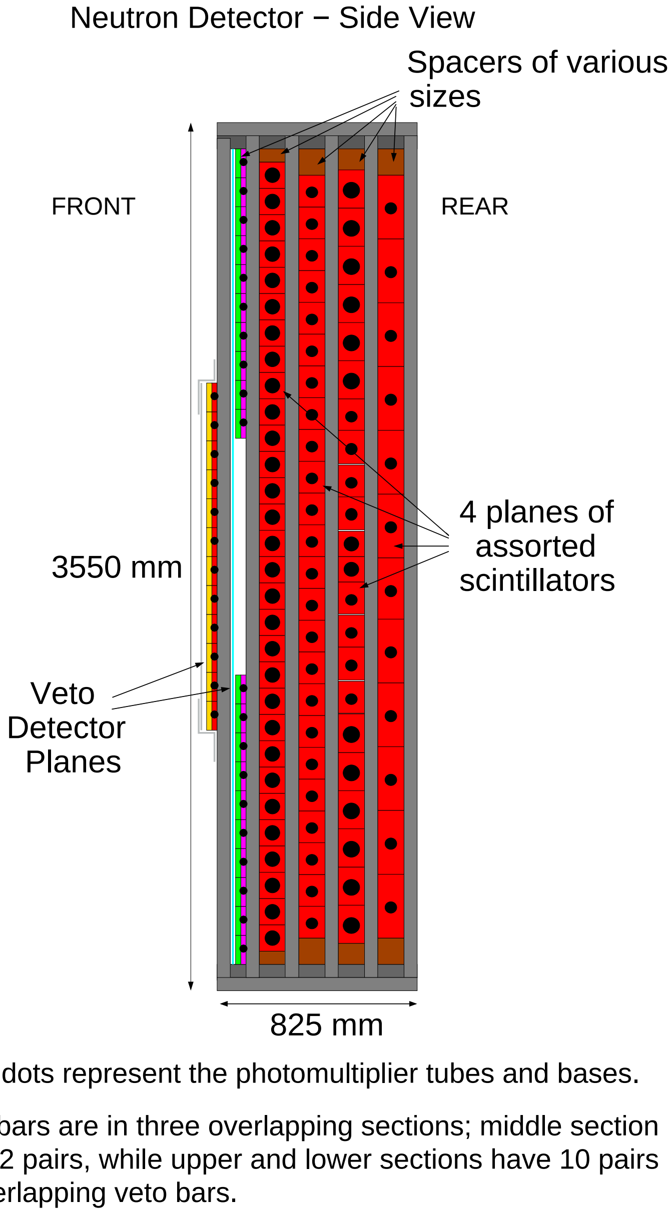
Neutron Detector − Side View
Spacers of various sizes
FRONT
REAR
4 planes of assorted scintillators
3550 mm
Veto Detector Planes
825 mm
Black dots represent the photomultiplier tubes and bases.
Veto bars are in three overlapping sections; middle section has 12 pairs, while upper and lower sections have 10 pairs of overlapping veto bars.

Figure 3-17: A side view diagram of the neutron detector, showing the layer of 2 cm veto bars at the front and the different heights of 10 cm thick scintillator bars used throughout the four planes of the detector.

3.6.4 The Complete Package

With all the detector components assembled, the final setup of the BigBite spectrometer in the hall is shown in Fig. 3-18. The final piece of equipment built for use with this setup was a lead wall, to shield the neutron detector from photon and charged particle radiation from the target. A separate radiation shielding test in the hall had previously shown that the background radiation in the hall was negligible compared with radiation from the target and so only shielding in front of the neutron detector was required. A wall of 2 inch thick lead bricks encased in a steel box was built; the steel box was 1 inch thick on all sides, giving a total material thickness of $\sim$ 4 inches.

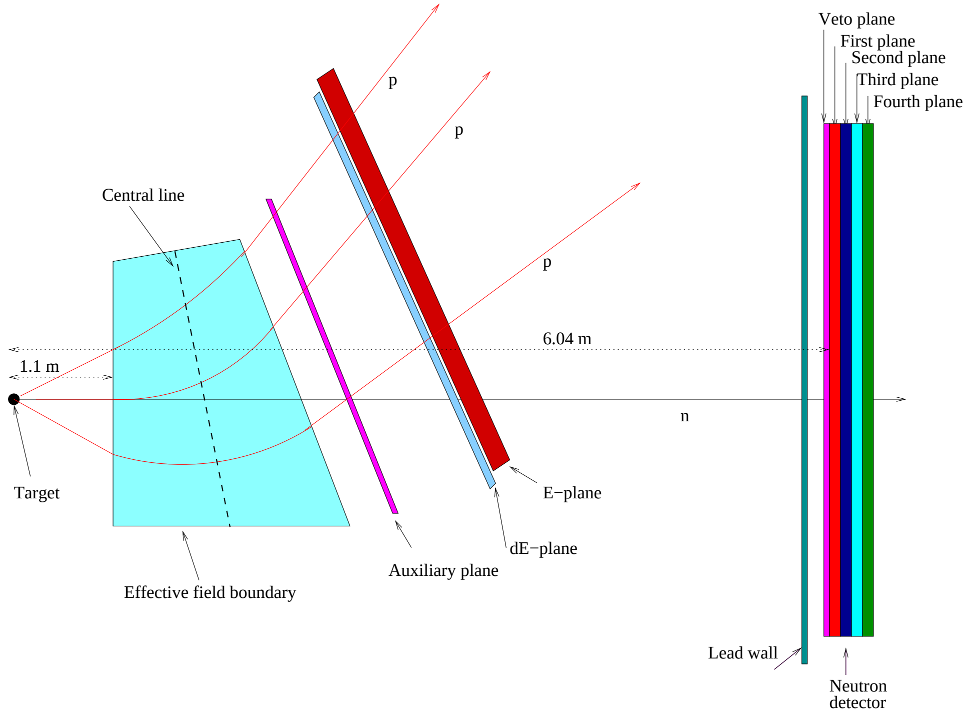
Veto plane
First plane
Second plane
Third plane
Fourth plane
p
p
p
Central line
6.04 m
1.1 m
n
Target
E−plane
dE−plane
Auxiliary plane
Effective field boundary
Lead wall
Neutron detector

Figure 3-18: A side view diagram of the complete BigBite spectrometer, showing the effective field boundary of the magnet, location of each detector and sample rays of protons and neutrons through each detector. Notice also, the lead wall in front of the neutron detector to provide shielding against photon radiation from the target.

In reality, when all of the equipment was assembled in the hall, it was crowded, as illustrated in Fig. 3-19. The magnet was placed as close to the target as possible and ended up being 1.1 m from the target. The 6 m distance from the target to the neutron detector was as close as it could be placed. Indeed, due to interference between BigBite and the right HRS, the smallest angle BigBite could be used at was 55°, assuming the HRS was at 12.5°.

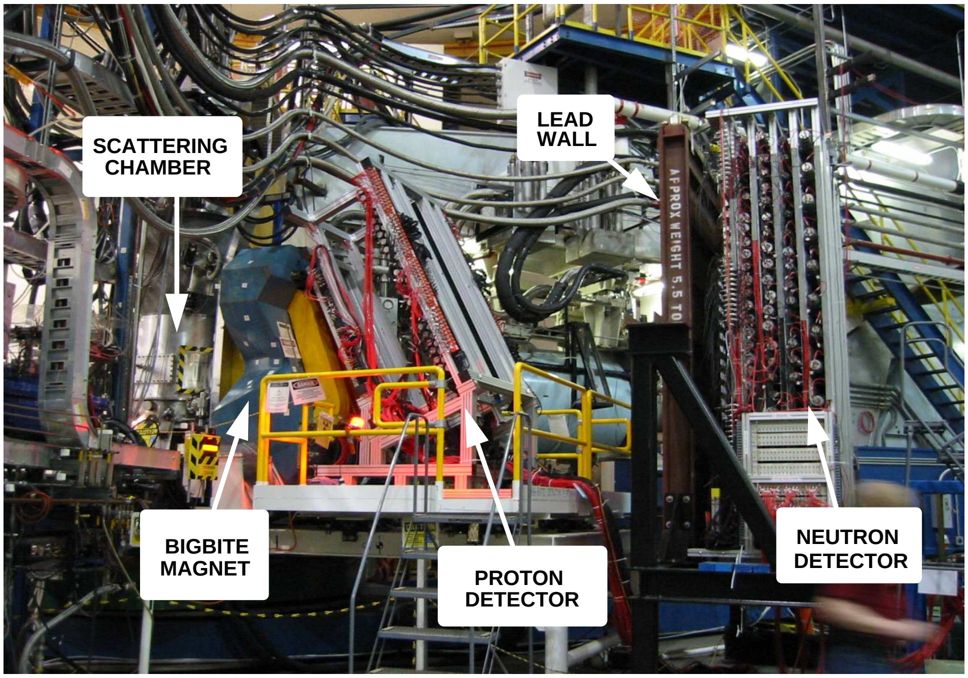

Figure 3-19: A photo of the complete BigBite spectrometer setup in the hall during the experiment.

3.7 Data Acquisition System and Trigger Setup

Data taken at JLab are primarily collected using the *CEBAF Online Data Acquisition* system (CODA) [46]. CODA provides the software tools to take the raw data from ADC, TDC and scaler modules, build events from the various pieces of information read out and then record the event data. Data is usually first written to a local disk and then transferred to long term storage on the *Mass Storage System* (MSS).

Raw signals from the detectors are first amplified and then split, with one copy going to ADCs and the other to TDCs via discriminator modules; all of these front-end modules are in the detector hut on each HRS. A trigger supervisor module decides if signals from the detector correspond to valid triggers or not. For this experiment, the trigger module was placed on the floor, among the data acquisition electronics used for the BigBite spectrometer. This meant that signals from the two HRSs had to be brought from the detector hut down to the floor, connected to the trigger supervisor, with the output signal then sent back up to the detector hut, allowing the relevant electronics to be read out appropriately.

The data in the ADCs and TDCs is collected by the *Read Out Controllers* (ROCs) - part of CODA. The ROC then passes the data to the CODA *Event Builder* (EB) which uses the pieces of information from the various ROCs to construct a single data structure for each event. Finally the data is passed from the EB to the *Event Recorder* (ER) which writes data to a local disk before eventually being transferred to the MSS. Various other pieces of information are inserted into the datastream at frequent intervals, for example, the beam current and beam position values.

The data is processed using the C++ based Hall A Analyzer [47], which is built on top of the ROOT libraries from CERN [48]. After the raw data is processed, an output root file is created containing raw and computed data. This file is then further analysed *offline* to extract diagnostic information and produce physics results. The Analyzer can read and decode raw event data, reconstruct tracks from the VDCs, compute basic physics quantities, define conditional cuts on the data and select events based on these cuts, fit analysis parameters to the data as well as display data in user defined histograms.

The electronics configuration used for the BigBite proton and neutron detector data acquisition is shown in Fig. 3-20. The raw signals from the PMTs in each detector are first amplified and then split into two copies. One signal goes to an ADC to measure the accumulated charge in that event. The other signal passes through a discriminator and if the pulse height is above a chosen threshold, a logical signal is output. Two copies of the logical output are used; one goes to scaler modules to count event rates and the other to TDC modules; together with timing information from the HRSs, the time-of-flight of particles detected in the proton and neutron detectors can be measured. The TDCs for the proton detector were operated in *common start* mode; the measured time interval is started by a signal from the HRS and stopped by a signal from the proton detector. The neutron detector TDCs were operated in *common stop* mode, where a signal in the neutron detector starts the time interval and the signal from the HRS stops it. The reason for using two different modes of operation for the proton and neutron detectors was dictated by the electronics available. The TDCs used with the proton detector had a fast response but could only deal with a single event at a time; the TDCs used with the neutron detector could deal with several events at a time—they were *multihit* TDCs—and had a longer response time per event and so were more suitable for use in *common stop* mode.

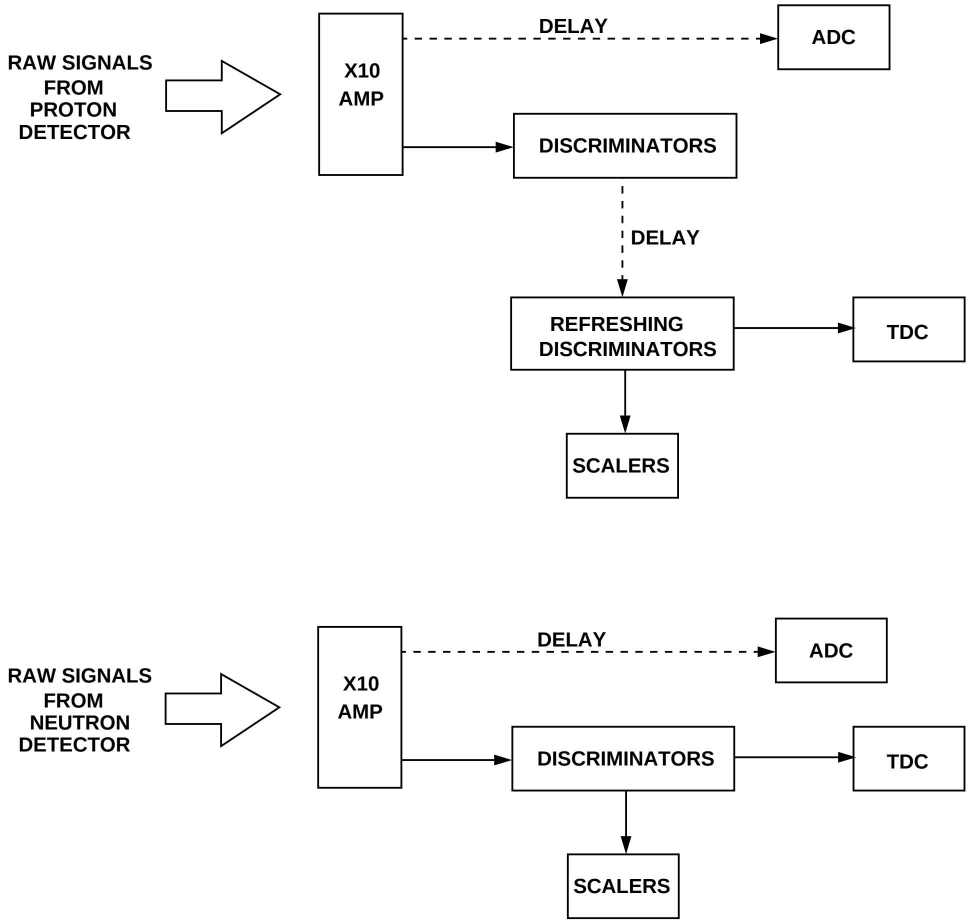
RAW SIGNALS FROM PROTON DETECTOR
X10 AMP
DELAY
ADC
DISCRIMINATORS
DELAY
REFRESHING DISCRIMINATORS
TDC
SCALERS
RAW SIGNALS FROM NEUTRON DETECTOR
X10 AMP
DELAY
ADC
DISCRIMINATORS
TDC
SCALERS

Figure 3-20: Electronics diagrams of the data acquisition system for both the proton and neutron detectors.

The trigger system used in this experiment included the standard Hall A HRS triggers and a trigger for each of the proton detector and neutron detector in BigBite. The different trigger types used were,

- T1 : the proton (right) HRS event trigger is a coincidence between a hit in the S1 and S2 scintillator planes in the proton spectrometer; for each scintillator plane, a hit is defined as the coincidence of the left and right PMTs on the scintillator bar.

- T2 : the auxiliary trigger for the proton HRS is defined as (S1 AND S0) OR (S2 AND S0) AND NOT (S1 AND S2); this auxiliary trigger allows the trigger efficiency for the proton spectrometer to be evaluated.

- T3 : the electron (left) HRS event trigger is a coincidence of a hit in the S1 and S2 scintillator planes in the electron spectrometer.

- T4 : the auxiliary trigger for the electron HRS uses the sum of the analog signals from all 10 PMTs in the gas cherenkov in coincidence with a hit in S1 OR S2; this auxiliary trigger allows the trigger efficiency for the electron spectrometer to be evaluated.

- T5 : the coincidence event trigger is defined as (T1 AND T3) – i.e. an event trigger from both the electron spectrometer and the proton spectrometer – within a certain time interval; this coincidence trigger defines the set of $(e, e'p)$ events.

- T6 : the BigBite proton detector singles trigger. This trigger was formed by making a coincidence between an event in the auxiliary plane AND a an event in an overlapping pair of bars in the δE and E planes.

- T7 : the neutron detector singles trigger. This was a logical OR of any signal from the left PMT of any scintillator bar in the neutron detector.

The data acquisition system (DAQ) was read out for events having any of the above trigger types. Doing this allowed the BigBite proton and neutron detectors to be read out for all of the HRS trigger types, T1 through T5. The proton and neutron detectors were calibrated with elastic scattering from a liquid hydrogen target, with the scattered electron detected in the left HRS and the knocked-out proton detected in either the proton or neutron detectors. During the calibration data-taking, only the T3 trigger from electrons detected in the left HRS is used and all events in the proton (or neutron) detector were recorded in the data aquisition system.

Chapter 4

Spectrometer calibrations and efficiency determination

This chapter describes the calibrations of the optics and detector databases, along with the calculation of various detector efficiencies.

4.1 High Resolution Spectrometer Optics Calibration

The Hall A analyzer (PODD) [47] requires an optics database to reconstruct the momentum (direction and magnitude) and the interaction vertex at the target based on the coordinates of the particle detected at the focal plane in each HRS. The data analysis uses the particle trajectories described in the following three coordinate systems, all of which are right-handed cartesian systems.

1. Hall Coordinate System (HCS): The origin is the center of the hall defined as the intersection of the "*ideal*" unrastered electron beam with the plane perpendicular to the beam containing the vertical symmetry axis of the target system. The $\hat{z}$-axis points in the beam direction; the $\hat{y}$-axis points vertically upwards; the $\hat{x}$-axis points to the left of the beam line, perpendicular to the $\hat{y}$ and $\hat{z}$-axes. This coordinate system is shown in Fig. 4-1.

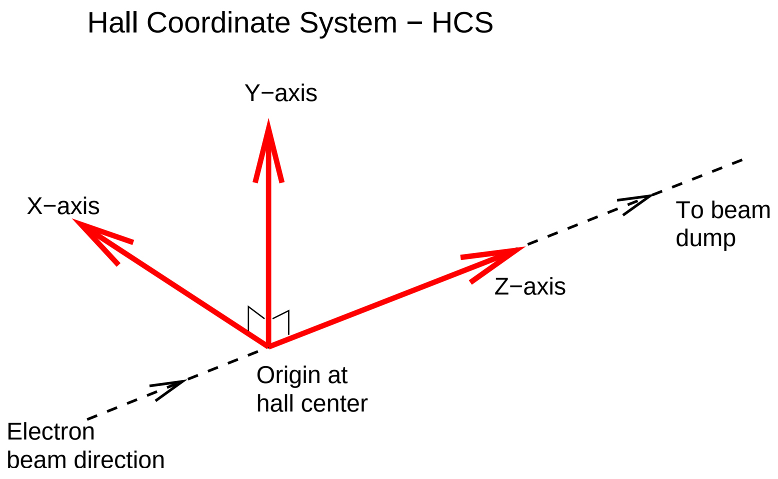

Figure 4-1: The Hall A coordinate system, with its origin defined to be the center of the hall with the z-axis pointing along the electron beam direction.

2. Target Coordinate System (TCS): The origin is defined as the point 1.25 m from the center of the central hole in the sieve slit plate[1] perpendicular to the sieve plate surface and pointing toward the target. The $\hat{z}_{tg}$-axis is defined as the line perpendicular to the sieve slit plate of each spectrometer, pointing towards the central hole in the sieve plate. The $\hat{x}_{tg}$ points vertically downwards with the $\hat{y}_{tg}$ forming the right-handed triplet. The in-plane (ϕ_{tg}) and out-of-plane angles (θ_{tg}) are given by,

$$\tan\theta_{tg} = \frac{dx}{dz} \qquad (4.1)$$

$$\tan\phi_{tg} = \frac{dy}{dz} \qquad (4.2)$$

and are shown in Fig. 4-2. The deviation of the particle momentum (p) from the central momentum of the spectrometer ($p_\circ$ is given by the coordinate δ_{tg} where,

$$\delta_{tg} = \frac{p - p_\circ}{p_\circ} \qquad (4.3)$$

3. Focal Plane Coordinate System (FCS): This is a rotated coordinate system

---

[1] The sieve slit plate [32] is a 5mm thick stainless steel plate, with a regular pattern of 49 (7 x 7) holes drilled through it. Two of the holes have twice the diameter of all the others allowing the orientation of the sieve plate at the focal plane to be easily determined by the scattering data

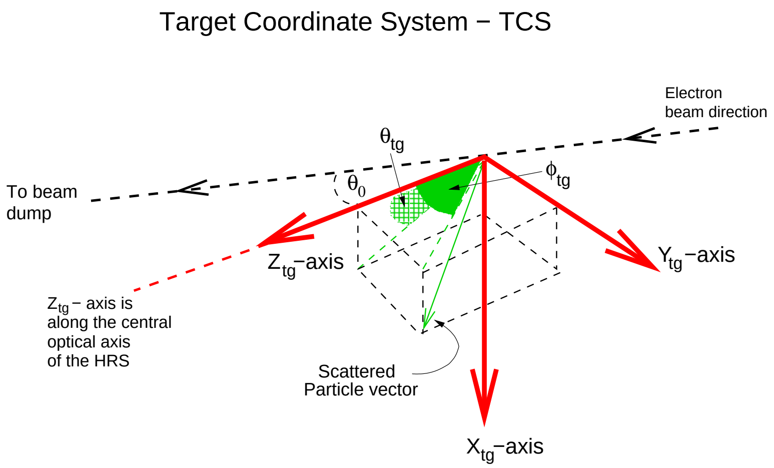
Target Coordinate System − TCS
Electron beam direction
θtg
φtg
θ0
To beam dump
Ztg−axis
Ytg−axis
Ztg− axis is along the central optical axis of the HRS
Scattered Particle vector
Xtg−axis

Figure 4-2: The target coordinate system; note, that the z_{tg}-axis points along the central axis of the spectrometer and is rotated an angle $\theta_\circ$ from the electron beam direction. The in-plane angle (ϕ_{tg}) and out-of-plane angle (θ_{tg}) of the scattered particle are defined in this coordinate system.

where the $\hat{z}_{fp}$ is rotated by an angle $\rho(x_{fp})$ between the *local* central ray[2] of the spectrometer and the vertical axis in the VDC wire plane. This means the $\hat{z}_{fp}$ rotates along the long symmetry axis of the VDC as a function of the relative momentum δ_{tg}, as shown in Fig. 4-3.

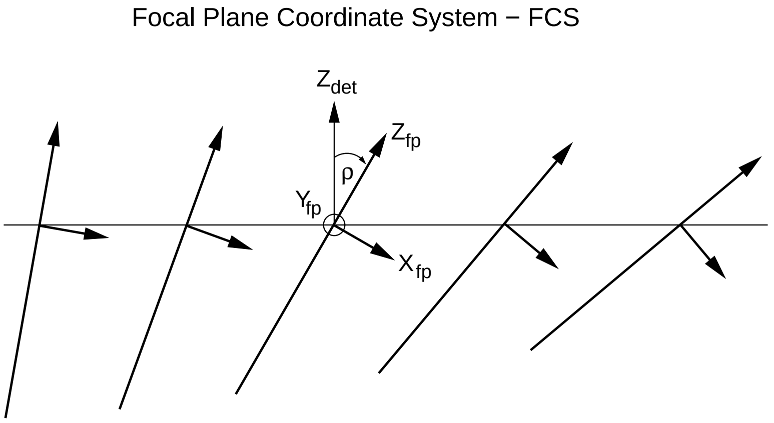
Focal Plane Coordinate System − FCS
Zdet
Zfp
ρ
Yfp
Xfp

Figure 4-3: The focal plane coordinate system. Note that Z_{det}, the local central ray is perpendicular to the wire planes in the VDCs.

---

[2] The *local central ray* has $\theta_{tg} = \phi_{tg} = x_{tg} = y_{tg} = 0$ for the corresponding δ_{tg} but the central ray in the spectrometer has $\delta_{tg} = 0$ as well.

The target cordinates are reconstructed from the focal plane coordinates of the detected particle using the matrix elements $Y_{ijkl},\ T_{ijkl},\ P_{ijkl},\ D_{ijkl}$ where,

$$y_{tg} = \sum_{i,j,k,l} Y_{ijkl}(x_{fp})^i(\tan\theta^j_{fp}(y_{fp})^k(\tan\phi_{fp})^l \tag{4.4}$$

$$\tan\theta_{tg} = \sum_{i,j,k,l} T_{ijkl}(x_{fp})^i(\tan\theta_{fp})^j(y_{fp})^k(\tan\phi_{fp})^l \tag{4.5}$$

$$\tan\phi_{tg} = \sum_{i,j,k,l} P_{ijkl}(x_{fp})^i(\tan\theta_{fp})^j(y_{fp})^k(\tan\phi_{fp})^l \tag{4.6}$$

$$\delta_{tg} = \sum_{i,j,k,l} D_{ijkl}(x_{fp})^i(\tan\theta_{fp})^j(y_{fp})^k(\tan\phi_{fp})^l \tag{4.7}$$

The vertical mid-plane symmetry of each spectrometer requires that,

$$T_{ijkl} = D_{ijkl} = 0 \qquad \text{for odd } (k+l) \tag{4.8}$$

$$Y_{ijkl} = P_{ijkl} = 0 \qquad \text{for even } (k+l) \tag{4.9}$$

In order to calibrate the $Y_{ijkl},\ T_{ijkl},\ P_{ijkl},\ D_{ijkl}$ matrix elements, an overconstrained set of data in which some of the initial conditions are known, is used. The calibration is simplified by using the reaction point along the beamline, z_{react}, with the horizontal and vertical particle trajectories projected to the sieve plane, x_{sieve} and y_{sieve}. These three coordinates can be uniquely determined for a set of foil targets and the sieve slit plate with the equations,

$$z_{react} = -(y_{tg}+D)\frac{\cos(\phi_{tg})}{\sin(\theta_\circ+\phi_{tg})} + x_{beam}\cot(\theta_\circ+\phi_{tg}) \tag{4.10}$$

$$y_{sieve} = y_{tg} + L\tan\phi_{tg} \tag{4.11}$$

$$x_{sieve} = x_{tg} + L\tan\theta_{tg} \tag{4.12}$$

where L is the distance from the center of the hall to the sieve plane and D is the horizontal displacement of the central axis of the spectrometer from its ideal location; $\theta_\circ$ is the central angle setting of the spectrometer. The vertical coordinate x_{tg} is determined by the beam position; z_{react}, θ_{tg} and the vertical displacement of the spectrometer from its ideal position. The matrix elements in the optics databases are calibrated by taking data such that some kinematic quantities of the detected particles are known and adjusting the matrix elements so that the analysis code [47] correctly reconstructs the known kinematic quantities. The usual dataset used for calibrating the optics databases is low energy ($\sim$ 845 MeV) carbon elastic scattering, $^{12}C(e,e')$. The Y_{ijkl} matrix elements (used to calculate y_{tg}) are calibrated using events scattered from a set of seven carbon foil targets and the known location of these targets; their location is accurately given by a survey of the target system prior to taking data. However, depending upon the individual experiment, a set of matrix elements can be improved by reconstructing a discrete missing energy peak for a particular $\mathrm{A}(e,e'p)\mathrm{B}$ reaction. This method also allows matrix elements for both spectrometers to be calibrated simultaneously.

The T_{ijkl} and P_{ijkl} matrix elements (used in determining θ_{tg} and ϕ_{tg}) are calibrated using events scattered from a single carbon foil target which pass through a sieve slit plate inserted at the entrance of each spectrometer. The knowledge of the location of each sieve plate and their corresponding set of holes as well as the target location is required and is known from the spectrometer survey. Finally, the D_{ijkl} matrix elements (for determining the δ_{tg} coordinate) are calibrated using the measured momentum of electrons elastically scattered from the set of carbon foil targets. The optics database calibration procedures are discussed in detail in [49].

In this experiment, the Y_{ijkl} matrix elements were calibrated with quasielastic scattering data taken using the carbon multifoil targets with $E_{beam} = 4.6GeV$. The procedure requires the data to be reconstructed at the correct y_{tg} location (as determined from a survey of the targets) for each of the seven carbon foil targets. The data distribution at each target foil location should also become narrower when the matrix elements are improved. The improvement after calibration for the electron spectrometer is shown in Fig. 4-4, where the red trace represents the reconstructed y_{tg} distribution after adjustment of the Y_{ijkl} matrix elements; the black trace shows the distribution before adjusting the matrix elements. Notice, that the location of the foils in the calibrated database have shifted such that the central target is at $y_{tg} = 0$ as expected from the target survey.

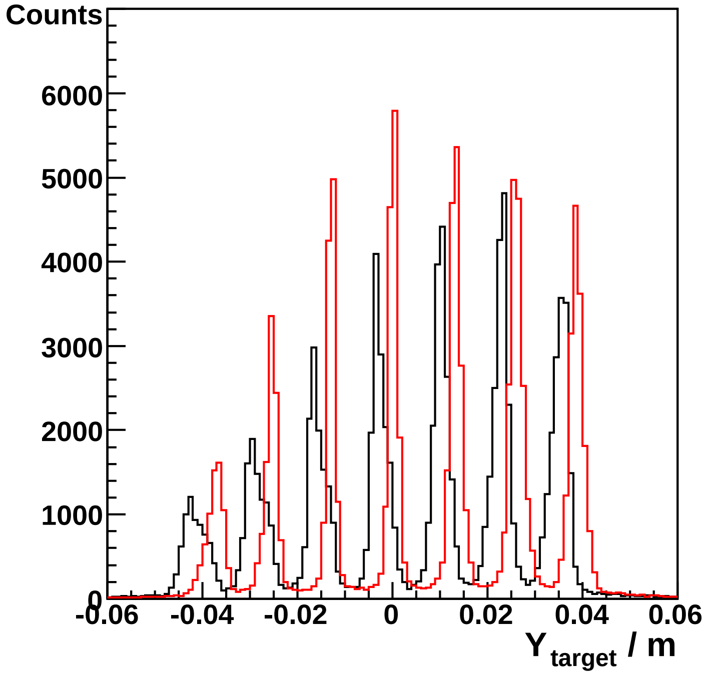

Figure 4-4: The y_{tg} reconstruction for the set of carbon optics foils before (black trace) and after (red trace) the database calibration for the Y_{ijkl} matrix elements.

The T_{ijkl} and P_{ijkl} matrix elements controlling the reconstruction of the angular coordinates, θ_{tg} and ϕ_{tg}, were calibrated with quasielastic scattering from a single carbon foil with events having to pass through the sieve plate. This calibration data was taken with beam energy of 1.2 GeV; the sieve plate was never used during the physics data-taking at 4.6 GeV. The reconstructed data is projected to the plane of the sieve plate and then compared to the known location of each hole in the sieve plate. Several iterations were required, with tuning individual groups of matrix elements before finally adjusting all matrix elements together. The improvement for the angle reconstruction in the electron spectrometer is shown in Fig. 4-5; the intersections of the lines on the plots of x_{sieve} versus y_{sieve} indicate the locations of the holes in the sieve plate. A sieve slit plate was not available for the proton spectrometer and so the T_{ijkl} and P_{ijkl} matrix elements for the proton could not be improved upon.

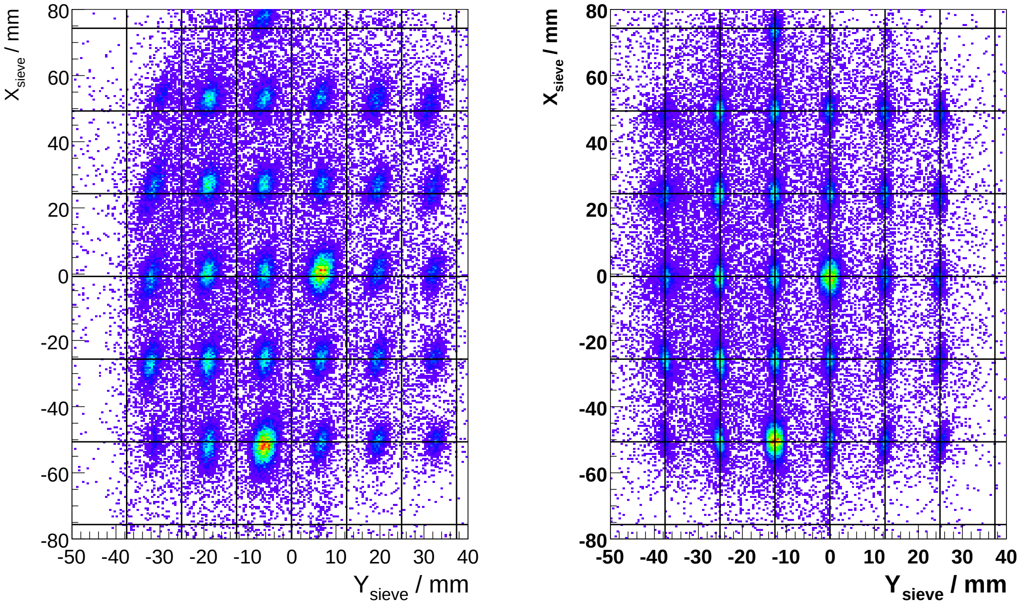

Figure 4-5: The reconstruction of the sieve hole locations before (left figure) and after (right figure) the calibration for the T_{ijkl} and P_{ijkl} matrix elements.

The D_{ijkl} matrix elements (for determining the δ_{tg} coordinate) were adjusted simultaneously for both spectrometers by reconstructing the ground state missing energy peak for the $^{12}\mathrm{C}(e,e'p)^{11}\mathrm{B}$ reaction. The data used was from the first kinematic of the physics dataset, with beam energy of 4.63 GeV. The experimental resolution and the statistics obtained meant that the initial database matrix elements could not be improved upon.

4.2 Spectrometer Mispointing

The HRSs are not constrained to remain along a radius to the hall center as they rotate around the central pivot. This means the spectrometer central ray can miss the hall center by as much as ± 3 mm in the horizontal plane and ± 0.5 mm in the vertical plane; this is known as *spectrometer mispointing*. Unfortunately, these displacements are not reproducible—moving the spectrometer to the same angular location at different times leads to different horizontal and vertical displacements[3]. However, these displacements can be measured and corrected for with two different methods.

1. A full survey of the spectrometers, accurately giving the location of the central axis of the spectrometer relative to the hall center, allowing the vertical offset and horizontal mispointing to be determined.

2. Using the known location of a carbon foil target (given by a survey of the target system), the horizontal mispointing can be found from the reconstructed position of the foil target along the beam line.

The spectrometers were only surveyed at the beginning of the experiment, therefore the spectrometer mispointing for each kinematic used during the physics data taking period had to be determined from the foil target reconstruction. This required knowing the target foil offset from the hall center, z_{lab}, provided by a survey of the target system. The spectrometer central angle with respect to the beam line, $\theta_\circ$ is determined from floor marks in the hall. The horizontal mispointing, Δl, is then found by,

$$\Delta l = S \cdot y_{tg} + z_{lab} \sin\theta_\circ \tag{4.13}$$

where S equals 1 (-1) for the electron (proton) spectrometer and y_{tg} is the reconstructed target position perpendicular to the central axis of the spectrometer. These quantities are illustrated in Fig. 4-6. The correction to the central scattering angle of each spectrometer, $\Delta\theta_\circ$ is found from the mispointing Δl by,

$$\Delta\theta_\circ = \frac{\Delta l}{L_m} \tag{4.14}$$

where $L_m = 8.458$ m and is the distance from the hall center to the floor marks used to determine the spectrometer central angle.

---

[3] This is observed to be true for the right HRS, however the left HRS position has been reasonably reproducible

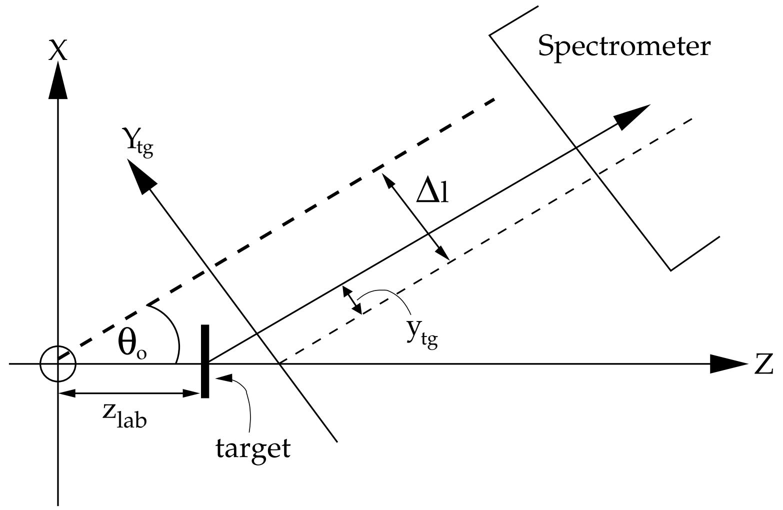

Figure 4-6: Definition of the mispointing variables, in the Hall coordinate system; the Y-axis in the hall frame is pointing out of the page.

4.3 HRS Coincidence Time Calibration

The coincidence time for an event is defined as the time difference between particles detected in each of the HRS spectrometers; it allows the time-of-flight of particles to be determined, allowing protons detected in coincidence with scattered electrons to be identified. The individual time for each particle is the mean time registered by a bar in the S2 scintillator plane relative to that spectrometer's trigger signal projected back to the target. The trigger signals in each HRS spectrometer are passed redundantly between each other, and so there are two possible measurements of the coincidence time—one each from separate TDCs located in each HRS spectrometer.

$$t^L_{S2} = t^L_{vertex} + \frac{d^L}{\beta^L c} \tag{4.15}$$

$$t^R_{S2} = t^R_{vertex} + \frac{d^R}{\beta^R c} \tag{4.16}$$

where t_{vertex} is the time at the interaction vertex relative to the trigger time, d is the pathlength from the vertex and β is the particle speed relative to the speed of light. The timing resolution is maximized by modifying the detector databases for the S1 and S2 scintillator planes, which form the event triggers in each spectrometer, to minimize the width of the coincidence time peak.

The database calibration changes the ADC pedestals, time-offsets and timewalk corrections for each photomultiplier on all of the scintillator bars in the S1 and S2 detectors in both spectrometers. The ADC pedestal is the value of the ADC readout when there is no signal in the scintillator. The pedestals are found from specific runs taken with a pulser trigger when there is no beam on target and the data acquisition system (DAQ) is forced to read out all ADC channels. The ADC channels are corrected by subtracting the pedestal value from the raw ADC value. During ordinary running, a threshold is set on all ADC channels, usually the pedestal plus ten channels, such that channels below threshold are not read out by the DAQ; this is referred to as *pedestal suppression* and decreases the data file size and the readout time per event, thus reducing the deadtime.

The timewalk correction reflects the variations in the amplitude and/or risetime of the raw PMT signals leading to time differences being registered between signals when they trigger the discriminator in the analog-to-digital converter.

The timing offset in each scintillator bar reflects the time delays in the PMT and signal cables for each channel. Timing offsets were introduced to align the time difference between signals from the left and right PMTs on each scintillator bar in both the S1 and S2 detectors, to be zero.

A computer code has been written to adjust the database parameters for the S1 and S2 detectors based on an input database and to then output a new database. Several iterations are usually required to complete the adjustment for all scintillators such that the width of the coincidence time peak does not change.

After adjustment of the database parameters, the resolution in coincidence time was found to be much better for the measurement from the left (electron) HRS compared to the right (proton) HRS; $\sigma \simeq 457$ ps for the left HRS and $\sigma \simeq 586$ ps for the right HRS. Therefore, in all the data analysis which follows, the only coincidence time cut used is on that measured by the TDC in the left HRS. The difference in resolution is shown in Fig. 5-1.

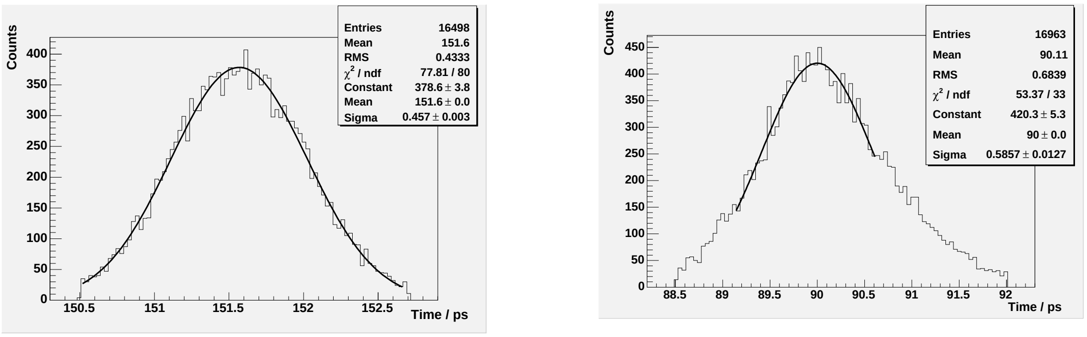

Figure 4-7: The coincidence time calibration for the left and right spectrometers; note the left arm measurement (left figure) has better resolution than the right arm measurement.

4.4 Efficiency Determination

4.4.1 Trigger Efficiency

The trigger efficiency for each spectrometer provides a measure of the probability of the production trigger firing in response to a passing charged particle. Since the trigger is generated by the scintillator planes in each spectrometer, the trigger efficiency is representative of the *inefficiency* of the scintillators and the electronics associated with the triggers being generated by these detectors. The scintillator inefficiency can be caused by inefficiencies in the photomultiplier tubes on each scintillator bar, deficient transmission of scintillation light along the bars to the photomultiplier tubes, geometric *holes* between scintillator bars in the detectors and fluctuations in the energy deposited by charged particles passing through the scintillator bars.

The trigger efficiency ϵ_e (ϵ_p) for electron (proton) detection is determined by the ratio of the number of primary event triggers to the total number of triggers. The primary trigger for the electron (proton) spectrometer is T_3 (T_1), while the auxiliary trigger for the electron (proton) spectrometer is T_4 (T_2); T_5 is the logical AND of the T_1 and T_3 primary triggers. The individual trigger types are discussed in section 3.7.

$$\epsilon_p = \frac{T_1 + T_5}{T_1 + T_2 + T_5} \tag{4.17}$$

$$\epsilon_e = \frac{T_3 + T_5}{T_3 + T_4 + T_5} \tag{4.18}$$

For both electron and proton event triggers, the efficiency was determined to be better than 0.999. This was consistent for data taken for all kinematics.

4.4.2 Tracking Efficiency

The tracking efficiency is the probability for a charged particle to be observed and measured by the vertical drift chambers (VDC) and the tracking software and thus has two components. The analyzer software finds the clusters of struck wires in each wire plane for each event and then fits various trajectories through these clusters. The single trajectory corresponding to the best fit through all four wire planes of each VDC pair is selected as the *golden track*. By using only the golden track events, the track reconstruction efficiency allows the VDC efficiency, the software event reconstruction efficiency and any other inefficiencies in the spectrometer which affect the track reconstruction to be combined in a single efficiency number.

Since the VDCs are used to determine the particle tracks, the sample dataset used to calculate the track reconstruction efficiency should not include any cuts on quantities that use VDC information. A sample dataset of electron (proton) events was defined by selecting events in the electron (proton) spectrometer without using any information from the electron (proton) spectrometer's VDCs. The cuts used to define the sample dataset for each spectrometer were,

1. A cut on the raw TDC values which are used to form the coincidence time.
2. Particle identification cuts; these are discussed in detail in Section 4.4.3.
3. Acceptance cuts on the θ_{tg}, ϕ_{tg} and δ_{tg} variables of the particle in the opposing spectrometer for which the track reconstruction efficiency was *not* being determined. Thus, when calculating the efficiency for the electron spectrometer, acceptance cuts on the proton spectrometer were used and vice-versa.
4. Cuts on the trigger scintillator planes of the spectrometer in question, such that only events that struck the scintillators well within their active areas were included.

After applying these cuts, the number of events remaining in the sample dataset is N_{sample}. Once the sample data were selected, the track reconstruction efficiency was defined as,

$$\epsilon_{e(p)} = \frac{N_{cut}}{N_{sample}} \tag{4.19}$$

where N_{cut} is the number of events remaining *after* applying cuts based upon VDC information in the spectrometer for which the track reconstruction efficiency is being determined. Thus, for the electron track reconstruction efficiency, N_{sample} is determined without using any cuts on the electron acceptance variables, θ_e, ϕ_e and δ_e. However, N_{cut} is determined by including the cuts on the electron acceptance variables as well as those used to determine N_{sample}. By varying the cuts on the θ, ϕ and δ acceptance variables, the efficiency can be determined as these cuts are made progressively narrower, so that events which are reconstructed well outside the spectrometer acceptance are removed. The efficiency gradually decreases until a limit is reached near the outer edge of the nominal spectrometer acceptance[4]. Making further cuts to a narrower acceptance range results in a very sharp drop in the efficiency as larger number of good events are rejected. The electron (proton) track reconstruction efficiency was then calculated as the average value of the efficiencies found for the series of progressively decreasing acceptance cuts used on the electron (proton) sample data. These efficiencies are used to correct the data yield for events lost due to incorrect track reconstruction by dividing the detected data yield by the efficiency found for the electron and proton spectrometers. A separate track reconstruction efficiency was determined for data at each kinematic and the values used are given in Table 4.1.

4.4.3 Particle Identification Efficiency

The efficiency with which each spectrometer correctly identifies the particle type is determined by selecting an event sample containing electrons (protons) and then

---

[4] The nominal acceptance is given in Table 3.2 and is defined such that it is within the edges of the actual spectrometer acceptance. Therefore, good tracks can be reconstructed within a reasonable range outside the nominal acceptance.

Efficiency	Kinematic		
	I	II	II
ϵ_e	0.973 ± 0.8%	0.9762 ± 0.7%	0.9716 ± 0.9%
ϵ_p	0.972 ± 0.8%	0.9717 ± 1.0%	0.974 ± 0.9%

Table 4.1: Track reconstruction efficiencies for electron and proton spectrometers, for each kinematic setting.

finding the fraction of events that are misidentified as other particle types.

For the left HRS, the preshower-shower detectors (discussed in Section 3.5.1) are used to differentiate between electrons and pions. Electrons will deposit more energy in the preshower-shower detectors than the pions. This means that pions will be detected at lower ADC channels in both the preshower and shower detectors than electrons. Therefore, by looking at the sum of the ADC distributions from both the preshower and shower detectors together, the distributions of pions and electrons are easily separated, as shown in Fig. 4-8.

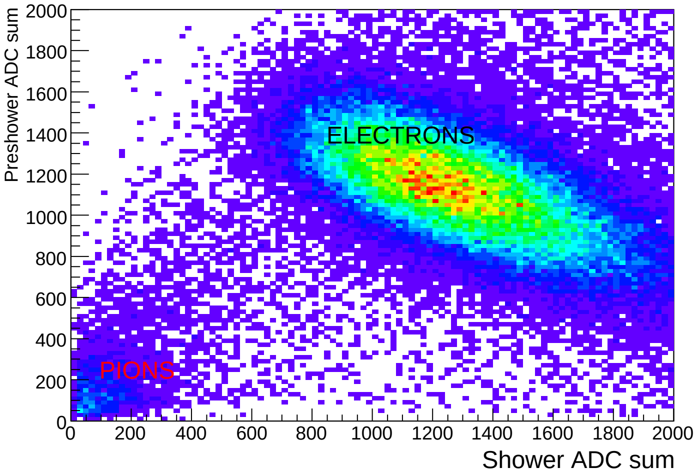

Figure 4-8: The sum of ADC signals from the preshower versus shower detectors allows electrons and pions in the left HRS to be easily separated.

The electron event sample is further refined by using a cut on the gas Čerenkov detector to check the events in the preshower-shower detectors. As explained in Section 3.5.1, the gas Čerenkov cannot detect pions directly because a pion would have to have a momentum of $\sim$ 4.8 GeV/c to produce Čerenkov light due to the refractive index of the carbon dioxide gas in the detector (n=1.00041); this is larger than the momentum of particles being detected in the electron spectrometer. Instead, a pion can create secondary electrons through collisions in the gas, which are moving much slower and thus creating much less Čerenkov light in the detector. A suitable cut on the sum of the ADCs for all of the photomultiplier tubes on the gas Čerenkov easily separates the pions from the electrons. To define a cleaner sample of electrons, a cut on the Čerenkov ADC sum between 1000 and 2000 ADC channels was used.

The particle identification efficiency was determined by selecting a sample of good electron events by applying the coincidence time cut for $(e, e'p)$ events discussed in Section 4.3, acceptance cuts on θ_e, ϕ_e and δ_e and a cut on the ADC sum of the gas Čerenkov. Then, a suitable cut on the preshower-shower ADC sum distribution to separate electrons and pions was chosen. The efficiency is then defined as,

$$\epsilon_{pid} = 1 - \frac{N_{misidentified}}{N_e} \tag{4.20}$$

where $N_{misidentified}$ is the number of electrons misidentified by the preshower-shower (i.e. the number of events inside the cut on the pion event region); N_e is the total number of electrons in the sample. The particle identification efficiency was determined to be 0.997.

For the proton spectrometer (right HRS), the particle identification is achieved by using the time-of-flight of particles between the trigger scintillator planes to calculate the value of β for each event. This allows protons to be separated from deuterons and pions. However, it was observed that the coincidence time cut removed the deuteron and pion events from the proton spectrometer β distribution. This is shown in Fig. 4-9, where the upper (lower) plot shows the distribution of events before (after) the coincidence time cut was applied. This meant that no further proton particle identification cut was necessary and so no proton particle identification efficiency is required. Further discussion of this is presented in Section 5.2.

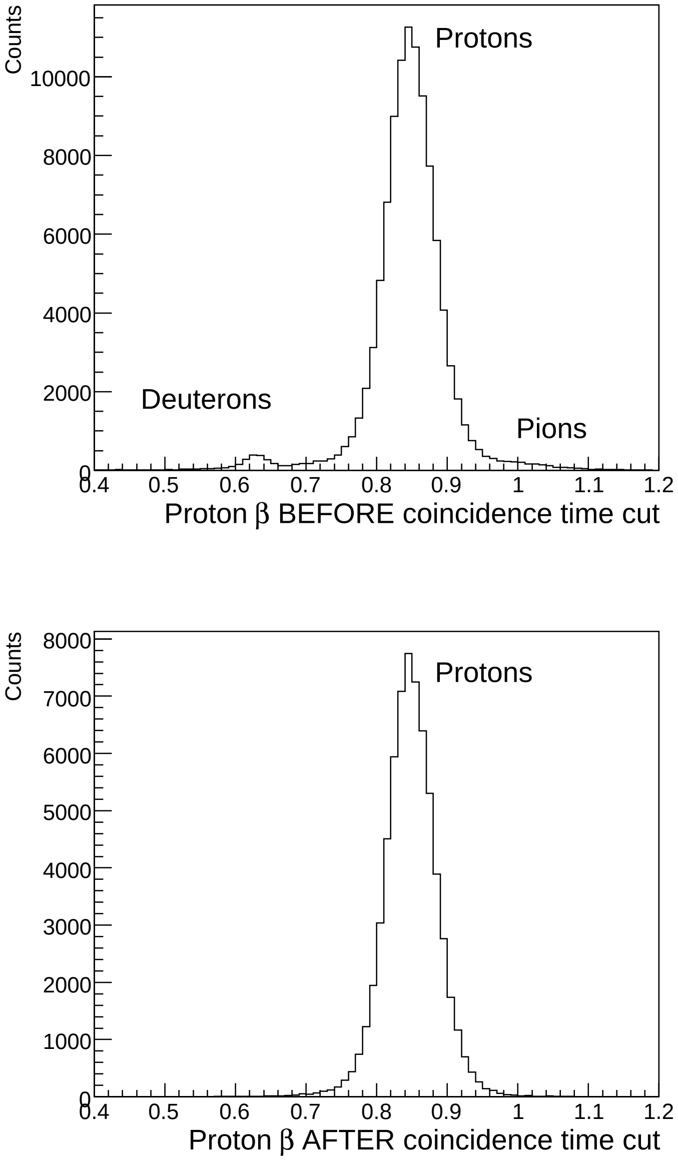

Figure 4-9: Comparison of the β value of particles detected in the proton spectrometer before (upper plot) and after (lower plot) the coincidence time cut is applied. Events corresponding to detected deuterons, protons and pions are shown in the upper plot. After applying the coincidence time cut, only the distribution corresponding to protons survives and so no further proton particle identification cut was necessary.

4.4.4 Data Acquisition System Deadtime

When the data aquisition system (DAQ) is reading out events detected in the spectrometers, it requires a small finite time to record the data. This is referred to as its *deadtime* because during this period the DAQ cannot record information from subsequent events. Even though the DAQ is dead for this short period of time, the number of events of each trigger type is continuously counted by scalers. This means that the deadtime can be accounted for by comparing the number of events of each trigger type registered on the scalers with the number recorded in the data file.

For each trigger type, the DAQ can be set to record only a fraction of those triggers by applying a suitable prescale factor for that trigger. Applying a prescale factor P_i to trigger type i results in only the P_i^{th} event of type i being recorded. Therefore, the deadtime is calculated by,

$$\epsilon_{DT}^{i} = 1 - \frac{P_i \cdot N_i}{S_i} \tag{4.21}$$

where N_i is the number of events recorded by the DAQ and S_i is the number counted by the scalers. The deadtime averaged around 13%. During the data analysis, the *livetime* ($\epsilon_{lt} = 1 - \epsilon_{DT}$) was calculated for each run and then used to correct the total charge accumulated for each kinematic. The corrected total charge is then used in the simulations of each dataset and the determination of the cross-section.

An *electronic deadtime* also exists where the time required by the electronics to process signals from the detectors is greater than the interval between events. This results in signal pile-up at the electronics and loss of data before the event is registered by the scalers. For this experiment, the highest event rate ($\sim<$ 4 kHz) was small enough for the electronic deadtime to be neglected [50].

Chapter 5

Analysis of $^{12}C(e, e'p)$ Data

This chapter describes the data analysis in detail. After completing the optimization and calibration measurements described in the previous chapter, the analysis code ROOT [48] was used to produce histograms of measured yields after various cuts were applied. The MCEEP Monte Carlo code [51] was used to simulate the measured yields and then to extract the radiatively corrected cross-sections and distorted spectral functions from the data. The software cuts applied to the data, the analysis methods used and the radiative corrections to the data are discussed.

5.1 Coincidence Time

The coincidence time is the time difference between the electron and proton detected in the two HRS spectrometers. Since both the electron and proton are relativistic and the detected proton has a narrow range of momenta, the coincidence time for true $(e, e'p)$ events is expected to form a sharp peak. An accidental coincidence event can be caused by random events in each spectrometer which happen to occur within the coincidence time window; these can contribute to background events observed in the coincidence time spectrum. A cut around this coincidence time peak is used to select the $(e, e'p)$ data in each kinematic setting. The limits of the cut were chosen as $\pm 3\sigma$ from the peak location of a gaussian function fitted to the peak in the coincidence time spectrum. Fig. 5-1 shows the coincidence time spectrum for the K1 dataset with the limits on the cut around the peak denoted by the dotted lines. For the kinematics used in this experiment, the contribution from random background events was evaluated by taking the same width of coincidence time cut as used around the peak and applying it to the region of the spectrum where there was only background events. The resulting background contribution was only 0.46%. Such a small background contribution in the coincidence time spectrum meant it was not necessary to subtract background events from the coincidence event data.

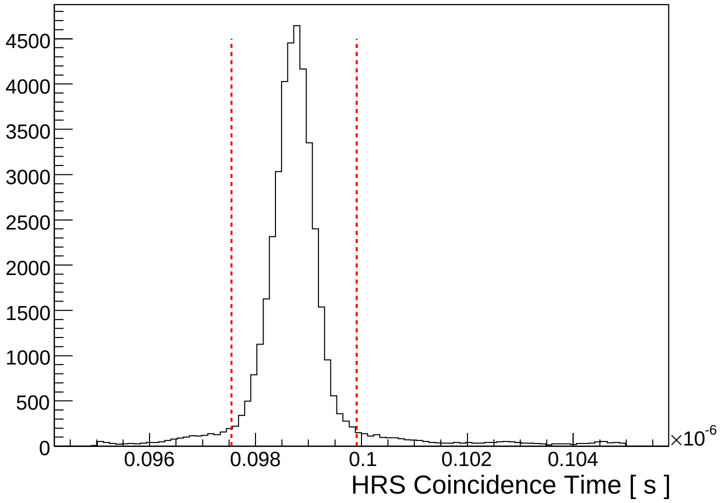

Figure 5-1: The HRS coincidence time spectrum from the first dataset. The limits on the cut were chosen by fitting a gaussian function to the peak of the distribution and then finding the limit as $\pm 3\sigma$ of the fitted gaussian. Note, the only part of the coincidence time window is shown here, to highlight the peak region. Background contribution was found to be $\sim 0.46\%$ by taking the same cut as used around the peak and applying it to a region of background events only.

5.2 Particle Identification

The $(e, e'p)$ coincidence event data was further refined by using particle identification in each spectrometer to reject events which were not electrons or protons. In the electron spectrometer, the preshower and shower detectors were used to separate electrons and pions. The distribution of events in the ADC sum for the preshower detector versus the ADC sum for the shower detector, as shown in Fig. 5-2, clearly shows a separation between electrons (in summed ADC channels > 800) and pions (in summed ADC channels <800). The pions are removed by applying a suitable two dimensional cut on the ADC sum of the preshower and shower, as indicated by the boxed region in the figure. This pion removal cut resulted in a pion contamination of the electron event sample of $\sim 0.075\%$.

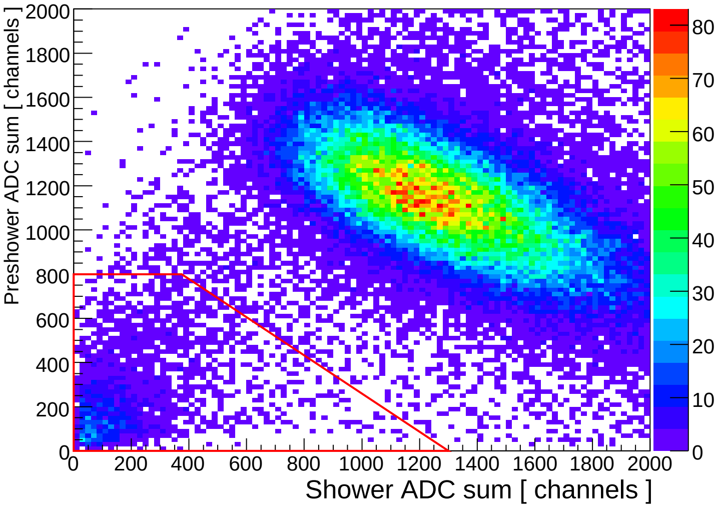

Figure 5-2: The sum of ADC channels for the preshower versus shower detectors shows the clear separation of electron and pion events. The pions are excluded by removing the events in the region indicated by the red line. With this cut, the electron detection efficiency is 0.997 and the resulting pion contamination was found to be $\sim 0.075\%$.

The majority of events detected in the proton spectrometer were observed to be protons by virtue of the fact that the energy deposited in the scintillator detectors was the same for most events. The calculated β value (v/c) for these events was as expected for each momentum setting of the proton spectrometer—$\beta \sim 0.8-0.85$. The full distribution of β for all events detected in the proton spectrometer showed events at values corresponding to detection of deuterons ($\beta \sim 0.6$) and pions ($\beta \sim 1.0$). However, once the coincidence time cut was applied to the dataset, only events with β values corresponding to protons remained. This is shown for the kinematic I dataset in Fig. 5-3, where the upper (lower) plot shows the β distribution before (after) the coincidence time cut is applied. The coincidence time cut on the β distribution provided sufficient proton particle identification and no further proton particle identification cut was necessary. Our calibration data for the proton spectrometer limited our ability to improve the reconstructed proton momentum, for example, by minimizing the width of the peak in missing energy for the $^{12}C(e,e'p)^{11}B$ reaction. Therefore, the width of the β distribution could not be minimized further than is shown in Fig. 5-3.

5.3 Spectrometer Acceptance

The coincidence event data was further refined by applying cuts to the angular acceptance (θ, ϕ) and momentum acceptance (δP) of both the electron and proton spectrometers. After calibration of the databases for the analysis software (as discussed in Section 4.1), events were still observed to have reconstructed outside the physical acceptance of the spectrometers and so were excluded using suitable acceptance cuts. The cuts were chosen to limit the data to a region of the θ, ϕ and δP distributions away from the edges of the acceptance where the distributions vary rapidly; the cuts are illustrated on the one-dimensional plots in Fig. 5-4. This means that the applied cuts were inside the nominal spectrometer acceptance limits as defined in Table 3.2. The distributions of events for both spectrometers for the angular and momentum acceptances are shown in Fig. 5-5 and Fig. 5-6; the lines indicate the cuts applied in each variable.

5.3.1 Pion and Delta-resonance Event Rejection

The missing energy spectra for all three kinematics appeared to have two peaks in the continuum. The second peak was always at a missing energy larger than 140 MeV and was likely due to pion production reaction channels becoming accessible. At missing energy values still higher again, it is possible contributions from delta-resonance channels were occuring. A suitable two-dimensional cut applied only to the continuum data analysis was developed to reject events at higher missing energies which were likely due to pion or delta-resonance production. Many combinations of

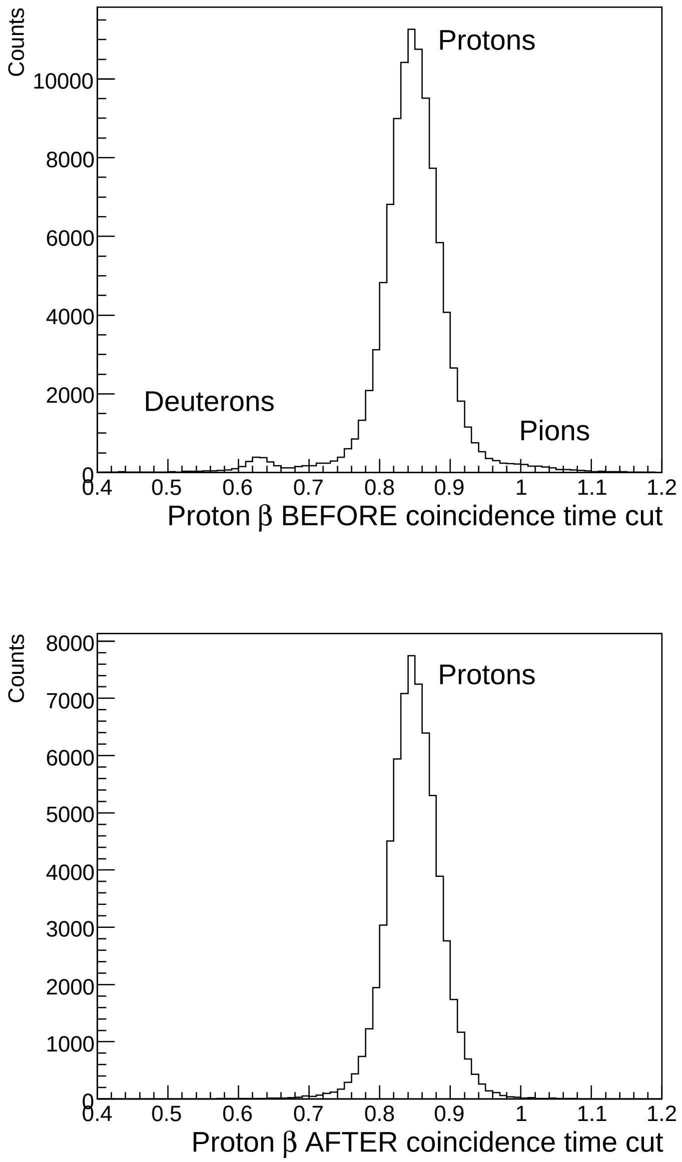

Figure 5-3: Comparison of the β value of particles detected in the proton spectrometer before (upper plot) and after (lower plot) the coincidence time cut is applied. Events corresponding to detected deuterons, protons and pions are shown in the upper plot. After applying the coincidence time cut, only the distribution corresponding to protons survives and so no further proton particle identification cut was necessary.

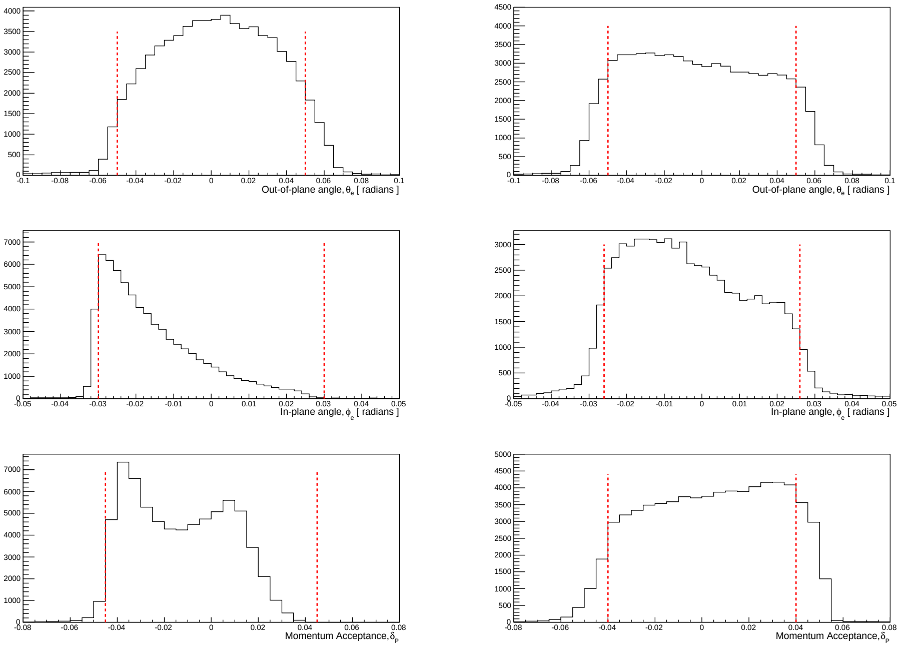

Figure 5-4: One dimensional distributions of out-of-plane angle (ϕ), in-plane angle (θ) and momentum (δ) acceptances; left plots are for the electron spectrometer, right plots are for the proton spectrometer. The dashed lines indicate the acceptance cuts used on each quantity. Data shown are from kinematic I.

variables and multi-dimensional spectra were investigated and the effect of chosing cuts on these variables evaluated. It was found that the most reliable method of removing the pion and delta-resonance events was a two-dimensional cut placed on a histogram of energy transfer, ω, versus the y-scaling variable. In a similar manner that the Bjorken-X variable, x_B represents the momentum carried by a struck quark in an electron scattering reaction, the y-scaling variable is the equivalent when considering nucleons instead of quarks. The momentum of the struck nucleon (which has absorbed the virtual photon) is given by y; the kinematic regime of $x_B > 1$ is equivalent to $y < 0$. The y-scaling variable derived for $(e, e'p)$ reactions is defined in [52] as,

$$y(\vec{q}, \omega) = [(M_A + \omega)\sqrt{\Lambda^2 - M_{A-1}^2 W^2} - \vec{q}\Lambda]/W^2 \tag{5.1}$$

where $W = \sqrt{(M_A + \omega)^2 - q^2}$ is the center-of-mass energy and $\Lambda = (M_{A-1}^2 - M^2 + W^2)/2$. The two-dimensional plot of ω versus y for the kinematic I data is illustrated

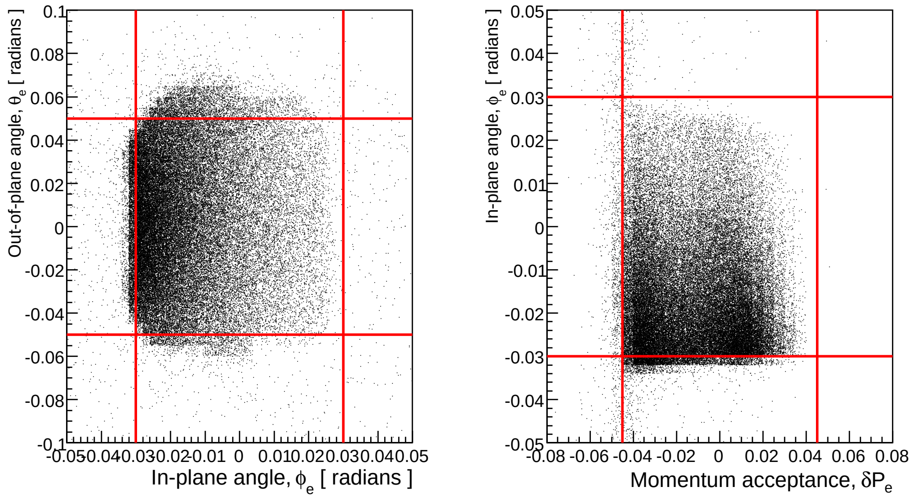

Figure 5-5: Distributions of electrons in the left spectrometer acceptance with the applied acceptance cuts shown by the solid lines. Left plot shows the out-of-plane angle versus the in-plane angle. Right plot shows the in-plane angle versus the momentum acceptance (given as a percentage of the spectrometer momentum setting). Note that some events reconstruct outside the physical acceptance of the spectrometer.

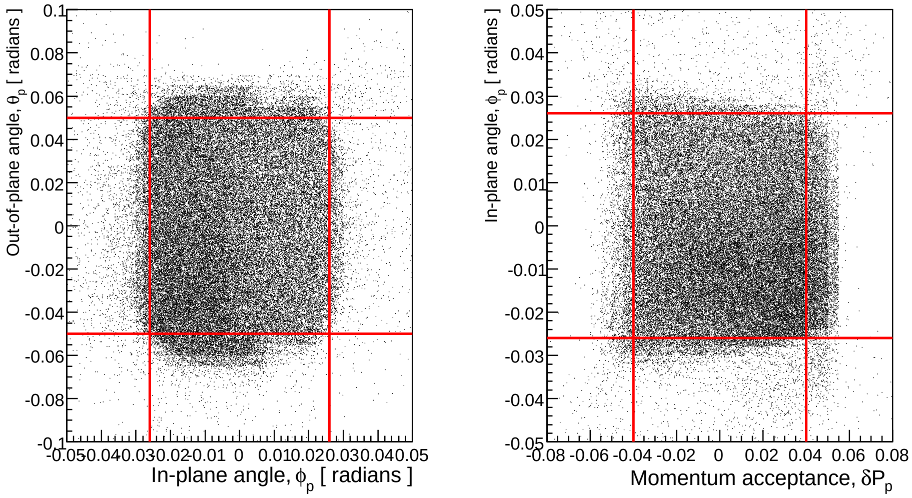

Figure 5-6: Distributions of proton in the right spectrometer acceptance with the applied acceptance cuts shown by the solid lines. Left plot shows the out-of-plane angle versus the in-plane angle. Right plot shows the in-plane angle versus the momentum acceptance (given as a percentage of the spectrometer momentum setting). Note that some events reconstruct outside the physical acceptance of the spectrometer.

in Fig. 5-7; the solid line indicates the location of the cut and events with higher ω and higher y values are rejected. Fig. 5-8 shows the ω-y distribution in three dimensions for kinematic I data, with the red line illustrating the cut location; the cut provides a separation at the minimum contour between the two peaks.

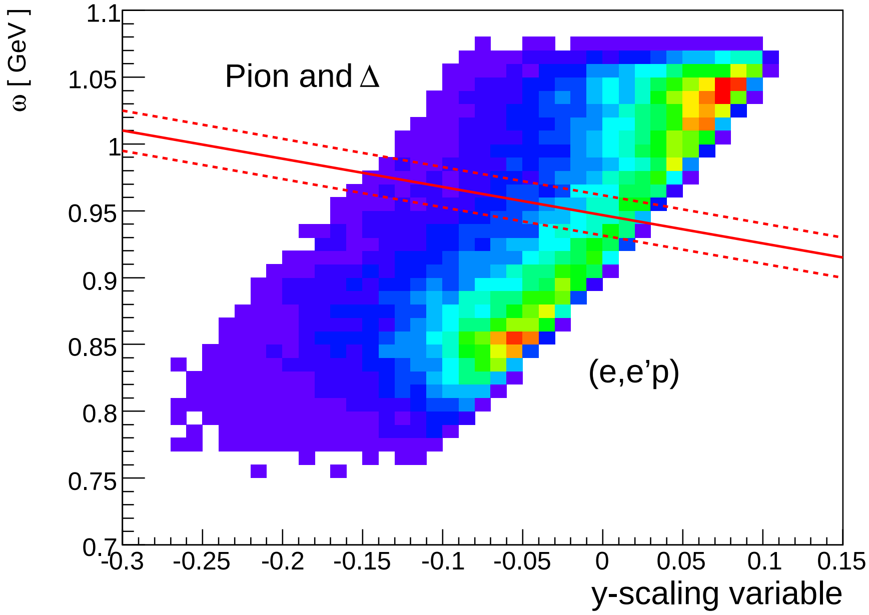

Figure 5-7: Two dimensional plot of ω versus y-scaling variable with the solid line representing the chosen empirical cut to reject possible pion or delta-resonance events. All events above the solid line were removed by this cut. The two dashed lines represent variations of this cut used to evaluate the systematic error associated with using this cut.

After applying the two-dimensional cut to the data, the resulting missing energy distribution is shown in Fig. 5-9 for kinematic I. The dashed (red online) line shows the events which survive the cut while the dotted (green online) line shows the events rejected by the cut. This cut allows events at missing energy higher than the pion production threshold to be analysed and included in the cross-section extraction.

Since y is a function of $\vec{q}$ and ω then this cut is dependent on the electron kinematics in the experiment. As the electron kinematics did not change during the experiment, once the cut was defined, it could be applied to all three kinematic without being changed. The two-dimensional distributions of ω versus y are shown in the

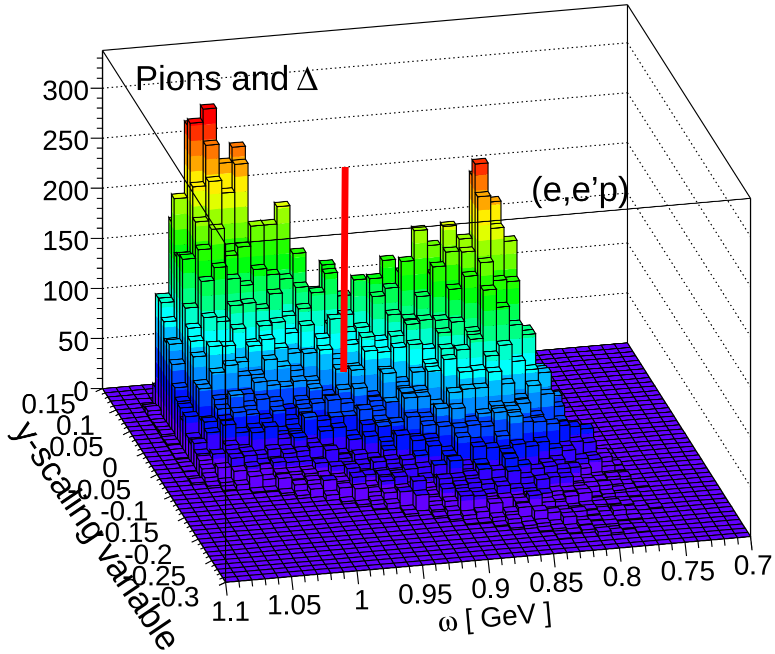

Figure 5-8: Three dimensional view of ω-y distribution showing the location of the empirical cut used. Events located to the left of the solid line, in the "pion and Δ" region were removed by this cut.

upper plots of Figs. 5-10 and 5-11 respectively; the lower plots show the resulting missing energy distributions, showing events which survive or are rejected by the ω-y cut.

5.4 Measured Data Ranges

The $^{12}C(e, e'p)$ kinematics used in this experiment and analysed in this thesis are summarised in Table 5.1. In each kinematic setting, the beam energy, electron spectrometer angle and momentum setting were unchanged. The angle and momentum setting of the proton spectrometer were changed to span a wide range of missing momenta. Two-dimensional plots of missing momentum versus missing energy for each kinematic are shown in Figs. 5-12, 5-13 and 5-14, illustrating the range of missing momentum covered.

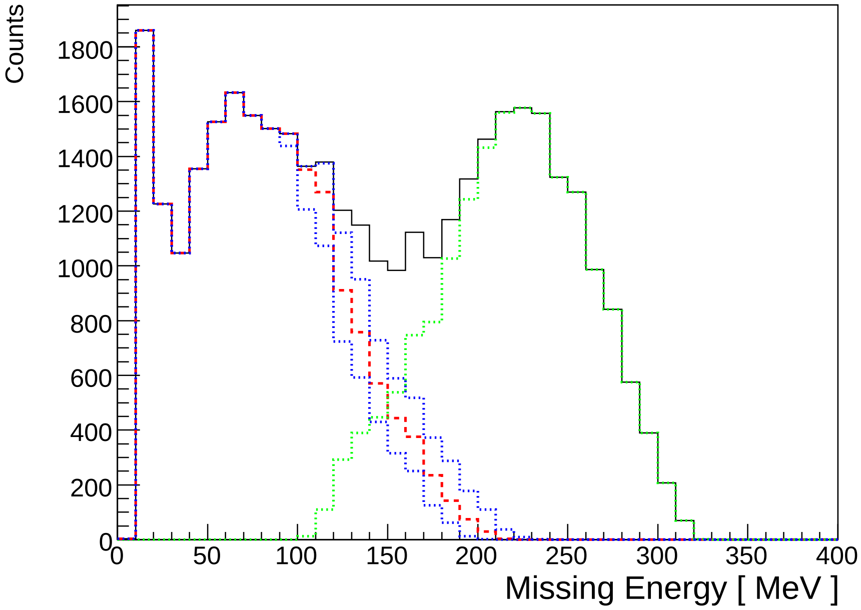

Figure 5-9: Missing energy distribution for kinematic I showing the events passing the empirical ω-y cut (dashed line - red online) and those rejected by the cut (dotted line - green online). The two dotted (blue online) lines around the dashed (red) line show the effect of using the upper and lower limiting cuts on the $\omega - y$ distribution and are used to evaluate the systematic error associated with this cut.

KIN	Electron Arm		Proton Arm		P_{miss} range
	$\frac{\theta_e}{deg}$	$\frac{\vec{k}_f}{MeV/c}$	$\frac{\theta_p}{deg}$	$\frac{\vec{p}_p}{MeV/c}$	MeV/c
I	19.5	3762	40.1	1450	200-450
II	19.5	3762	35.8	1420	300-550
III	19.5	3762	32.0	1360	400-650

Table 5.1: Kinematic settings of the electron and proton spectrometer used in this experiment.

5.5 Simulation of the Experiment

The MCEEP (**M**onte **C**arlo for **e,e′p**) simulation program was used to simulate the data. Originally written by Paul Ulmer [51] and developed with contributions from many others, this program simulates experiments which utilise the Hall A high resolution spectrometers. MCEEP allows many experiment specific options to be chosen,

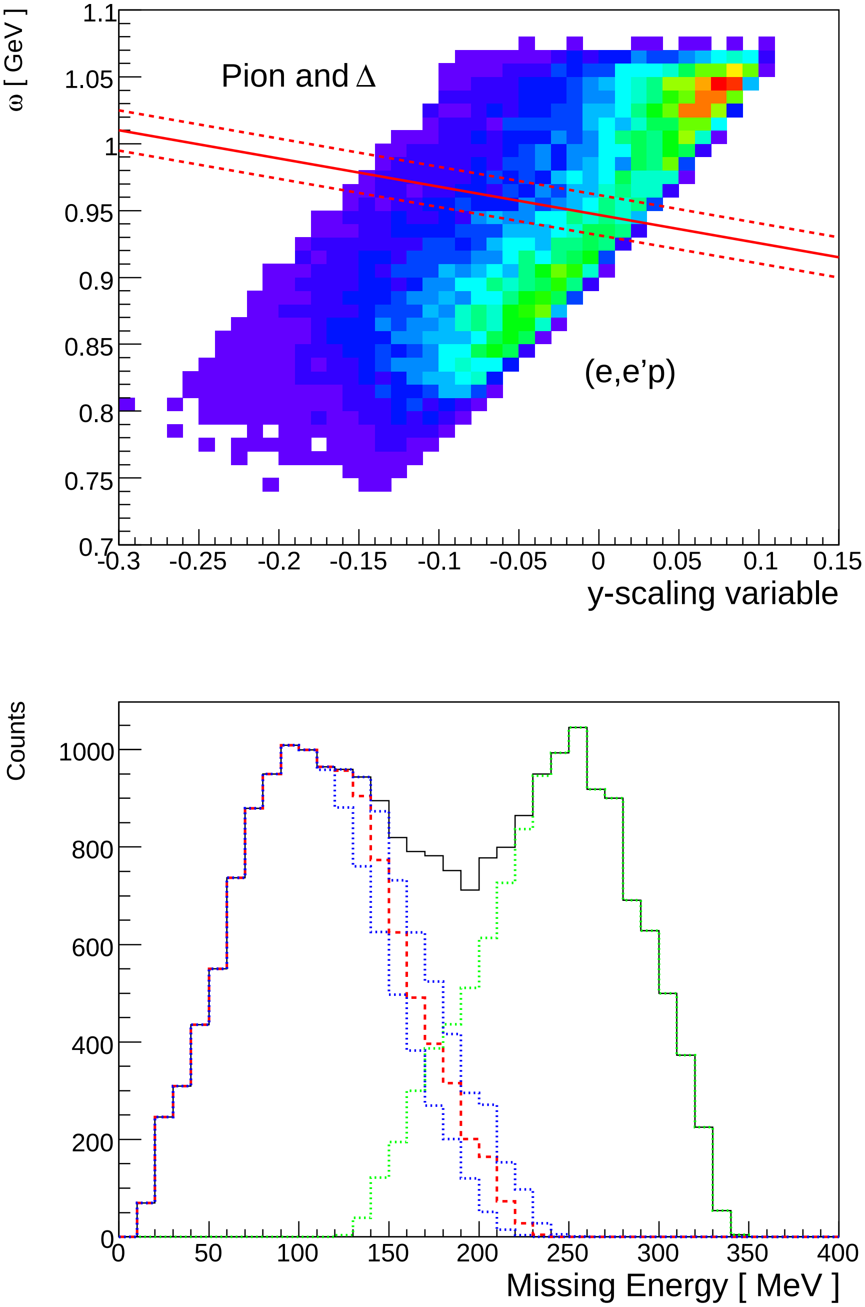

Figure 5-10: Upper Plot: Two-dimensional distribution of events in kinematic II of ω versus y-scaling variable, with empirical cut selected; dotted lines give limits of the systematic check of this cut on the final cross-section result. Lower Plot: Full missing energy distribution for kinematic II; dashed line (red online) shows the distribution after the ω-y cut is applied; dotted line (green online) shows the data rejected by this cut. The two dotted (blue) lines around the dashed (red) line show the effect of the upper and lower limits of the $\omega - y$ cut and are used to evaluate the systematic error associated with this cut.

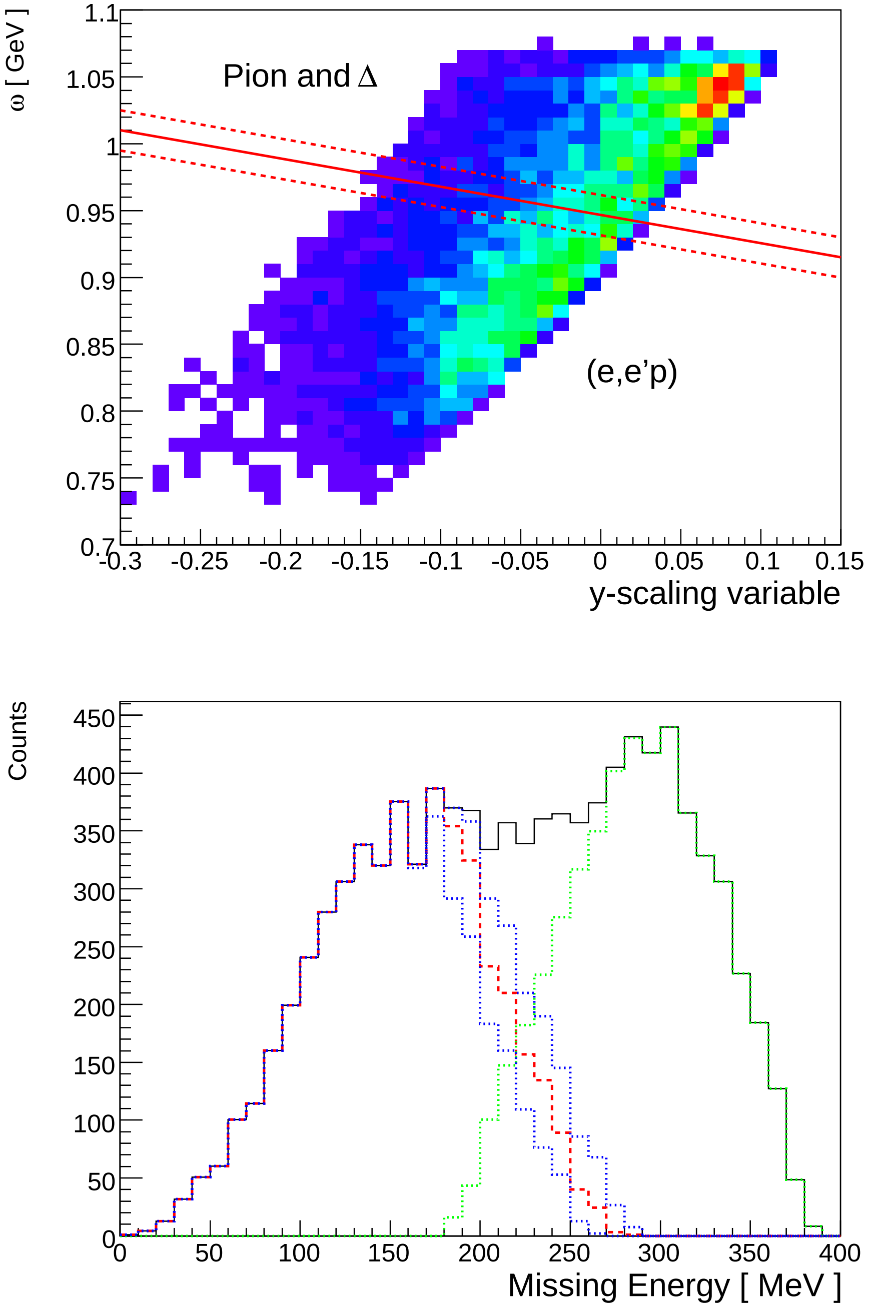

Figure 5-11: Upper Plot: Two-dimensional distribution of events in kinematic III of ω versus y-scaling variable, with empirical cut selected; dotted lines give limits of the systematic check of this cut on the final cross-section result. Lower Plot: Full missing energy distribution for kinematic III; dashed line (red online) shows the distribution after the ω-y cut is applied; dotted line (green online) shows the data rejected by this cut. The two dotted (blue) lines around the dashed (red) line show the effect of the upper and lower limits of the $\omega - y$ cut and are used to evaluate the systematic error associated with this cut.

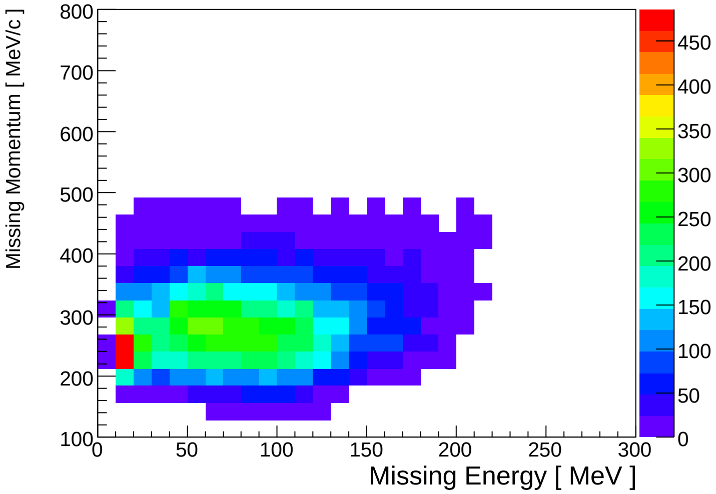

Figure 5-12: Distribution of missing momentum versus missing energy for kinematic I after all the described cuts have been applied. Note that this dataset shows clearly the bound state peak at low missing energy and momentum.

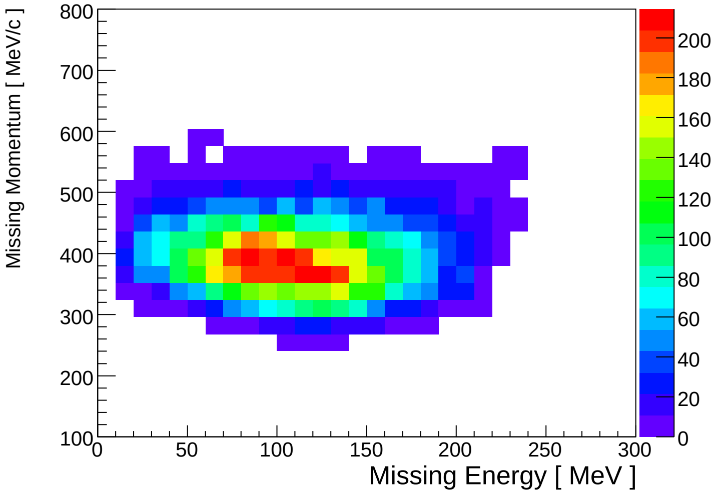

Figure 5-13: Distribution of missing momentum versus missing energy for kinematic II after all cuts applied.

such as target orientation, target density, energy losses, internal and external radiation, multiple scattering and spectrometer resolution. This meant that our input to the simulation could be tailored specifically for our experimental set-up.

For each event, a vector in the laboratory coordinate system is created for each

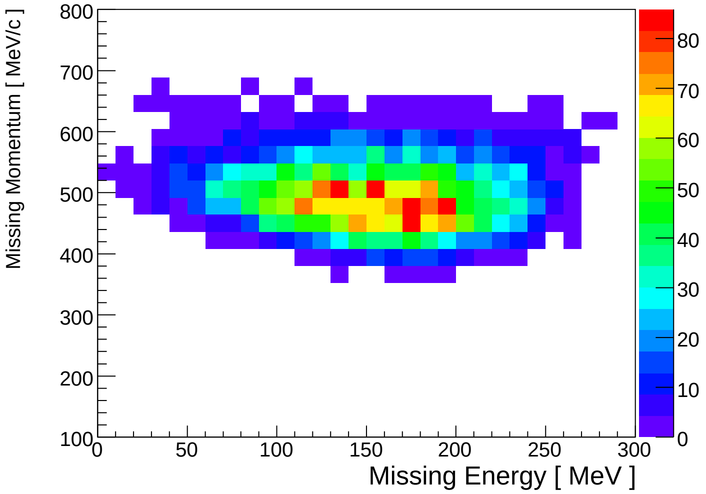

Figure 5-14: Distribution of missing momentum versus missing energy for kinematic III after all cuts have been applied.

spectrometer; these vectors are then converted to vectors in the reference frame of each spectrometer. The spectrometer resolution is simulated by applying several actions on these transport vectors. A forward transfer function is applied to particles at the target to transport them through the spectrometer to the focal plane. Multiple scattering in air and the spectrometer exit windows is simulated by applying gaussian smearing functions to the transport coordinates. A track reconstruction matrix is applied at the focal plane to simulation the position resolution of the vertical drift chambers. Finally, an inverse transfer function is applied to transport particles back to the target.

By comparison with the bound state $^{12}C(e,e'p)^{11}B$ peak in the missing energy spectrum, it was observed that an extra momentum resolution smearing was required to reproduce the FWHM of the peak. A gaussian smearing function with FWHM 0.07% was applied to δ_{tg} for each spectrometer in the simulations.

The spectrometer acceptances are simulated by applying aperture tests at five internal locations as particles are transported through the spectrometer. Particles which are outside or which strike the aperture at each point are discarded; those which pass proceed to the next aperture test, until only particles which have successfully passed through all five apertures remain and are tranported to the focal plane. However, it was observed that MCEEP could not reproduce the data around the edges of the nominal spectrometer acceptance; this may be due to some differences between the acceptance models and aperture models used by MCEEP and reality. Instead, the aperture tests were not applied in the simulations and the acceptance was defined by the software cuts discussed in Section 5.3. The acceptance cuts used were applied to the in-plane angle (ϕ), out-of-plane angle (θ) and momentum (δ) data distributions for both the electron and proton spectrometers. The events detected in each spectrometer are reconstructed by the analysis software back to the target, producing the distributions of angle and momentum of events at the interaction point. Therefore, by applying cuts to the data distributions in θ, ϕ and δ defines the acceptance used. Then, the same cuts which are applied to the data, are also applied to the simulations. The cuts used are smaller than the nominal spectrometer acceptances and are relevant for the region of uniform acceptance in the spectrometer. The acceptance cuts used can lead to a systematic error in the cross-section results, which can be evaluated by changing the cuts by a certain amount and determining the subsequent change in the cross-section results. The systematic errors are discussing in Section 5.8.

5.6 Experimental $(e, e'p)$ Cross-sections

The ${}^{12}C(e,e'p)^{11}B$ bound state and ${}^{12}C(e,e'p)$ continuum cross-sections were extracted from the data by modifying the plane wave impulse approximation ${}^{12}C(e,e'p)$ cross-section model in the MCEEP simulation until the simulated yield matched the number of counts detected in the data.

For each kinematic, the set of real coincident $(e,e'p)$ events are found by applying all the cuts described above to the data. A complete MCEEP simulation, including energy losses, multiple scattering, internal and external radiation and spectrometer resolutions was made for each kinematic. The same sets of cuts applied to the data, was also applied to the simulation, except for the coincidence time and particle identification cuts. For analysis of the ${}^{12}C(e,e'p)^{11}B$ bound state, the data is binned in missing momentum, $\vec{P}_{miss}$. For the $^{12}C(e,e'p)$ continuum analysis, the data is binned in both missing momentum and in missing energy, E_{miss}.

An iteration procedure was used to adjust the radiated $^{12}C(e,e'p)$ cross-section until the simulated yield agreed with the experimental yield in each bin. The details of this procedure as it was applied to the bound state and continuum data analyses is discussed in Sections 5.6.1 and 5.6.2. After agreement was reached for each kinematic, the non-radiated $^{12}C(e,e'p)$ cross-sections were extracted. The cross-section model used in this analysis was based on the factorised plane wave impulse approximation, as described in Section 2.5.2 and used the σ_{cc2} single-nucleon offshell cross-section prescription of DeForest [30]. The σ_{cc2} prescription is a current conserving offshell extrapolation of the on-shell current obtained from the Dirac equation for relativistic scattering interactions. This prescription includes explicitly the four-momentum transfer in the nucleon current calculation; further details are given in [30]. This method allows the radiatively corrected cross-section to be extracted from the data.

5.6.1 $^{12}C(e,e'p)^{11}B$ Five-fold Differential Cross-section

The $^{12}C(e,e'p)^{11}B$ two-body breakup channel appears as a peak in the missing energy spectrum; this was only observed in kinematic I, while kinematics II and III covered the continuum. The cross-section for the bound state reaction is obtained by integrating the continuum six-fold differential cross-section over the missing energy of the two-body breakup peak; essentially, the integral over the missing mass of the bound state system. The cross-section was defined in equation 2.18 as,

$$\frac{d^6\sigma}{d\Omega_e d\Omega_p dE_e dE_p} = E_p \, p_p \, \sigma_{ep} \, S(\vec{p}_m, E_m) \tag{5.2}$$

and so the five-fold differential cross-section is,

$$\frac{d^5\sigma}{d\Omega_e d\Omega_p dE_e} = \int \frac{d^6\sigma}{d\Omega_e d\Omega_p dE_e dE_p} \frac{1}{\left|\frac{\partial E_m}{\partial E_p}\right|} dE_m \tag{5.3}$$

where the partial derivative Jacobian is given by,

$$\frac{\partial E_m}{\partial E_p} = -1 + \frac{E_p \vec{p}_p \cdot \vec{p}_B}{p_p^2 E_B} \tag{5.4}$$

where $\vec{p}_B$ and E_B are the momentum and energy of the recoiling (A-1) system. Rewriting the cross-section in terms of the factorised components,

$$\frac{d^5\sigma}{d\Omega_e d\Omega_p dE_e} = E_p \, p_p \, \sigma_{cc2} \int S(\vec{p}_m, E_m) dE_m \tag{5.5}$$

In this case, the spectral function is assumed to factorise into two functions,

$$S(\vec{p}_m, E_m) = n(\vec{p}_m) f(E_m) \tag{5.6}$$

allowing the cross-section to be written as,

$$\frac{d^5\sigma}{d\Omega_e d\Omega_p dE_e} = E_p \, p_p \, \sigma_{cc2} \, n(\vec{p}_m) \int f(E_m) dE_m \tag{5.7}$$

Since the missing mass distribution function for a bound state is a delta function, this integral leads to the Jacobian given in equation 5.4 and the cross-section becomes five-fold differential. This means that the model cross-section can be modified by adjusting the input momentum distribution $n(\vec{p}_m)$ to the simulation.

Since the data in kinematic I is a mixture of bound state and continuum, a cut on the missing energy was placed at 20 MeV to define the bound state dataset. This limit was chosen as it is higher in missing energy than the peak location, but is lower than the onset of the continuum. Although the cut in missing energy is used to define the bound state data, the comparison between simulation and experimental data is made for the missing momentum distributions.

The procedure used to modify the input momentum distribution for each simulation, was to fit a function to the data and fit another function to the simulation yield for the missing momentum distributions. A polynomial of 5^{th} or 6^{th} order was used to fit the data and simulated distributions, depending on which function produced the lowest χ^2 per degree of freedom value. Then a new rational function was defined as,

$$F_i(\vec{p}_m) = \frac{f_i^{data}(\vec{p}_m)}{f_i^{sim}(\vec{p}_m)} \tag{5.8}$$

where $f^{data}(\vec{p}_m)$ and $f^{sim}(\vec{p}_m)$ were the functions fitted to the data and simulation yields respectively and the index i denotes the particular iteration number. This new rational function $F(\vec{p}_m)$ then multiplied the input momentum distribution used for the previous simulation to create a new input momentum distribution. The simulation was then run again with the new updated momentum distribution and the procedure repeated again. This iteration procedure continued until the simulated yield agreed with the experimental data; the rational function $F(\vec{p}_m)$ became approximately uniform with values ranging from 0.99 - 1.01 for all missing momentum bins. The experimental cross-section is obtained from normalising the factorised cross-section model in the simulation to it by,

$$\frac{d^5\sigma}{d\Omega_e d\Omega_p dE_e} = K\, \sigma_{cc2}\, F_0(\vec{p}_m) \prod_{i=1}^{i=n} F_i(\vec{p}_m) \tag{5.9}$$

where $F_0(\vec{p}_m)$ is the initial input momentum distribution and n iterations have been performed. The evolution of the simulated yield compared with the data is shown in Fig. 5-15.

The resulting missing energy distribution after the iteration procedure is complete is shown in Fig. 5-16; the right hand plot illustrates how the radiative tail from the bound state events penetrate into the continuum missing energy data. This allows us to subtract contributions from the bound state from the continuum dataset, which will be discussed in section 5.6.2.

5.6.2 $^{12}C(e, e'p)$ Six-fold Differential Cross-section

The six-fold differential cross-section for the $^{12}C(e, e'p)$ continuum data is extracted in a similar way to the five-fold differential cross-section. The cross-section model in the simulation is iteratively modified until the yield from the simulation matches the

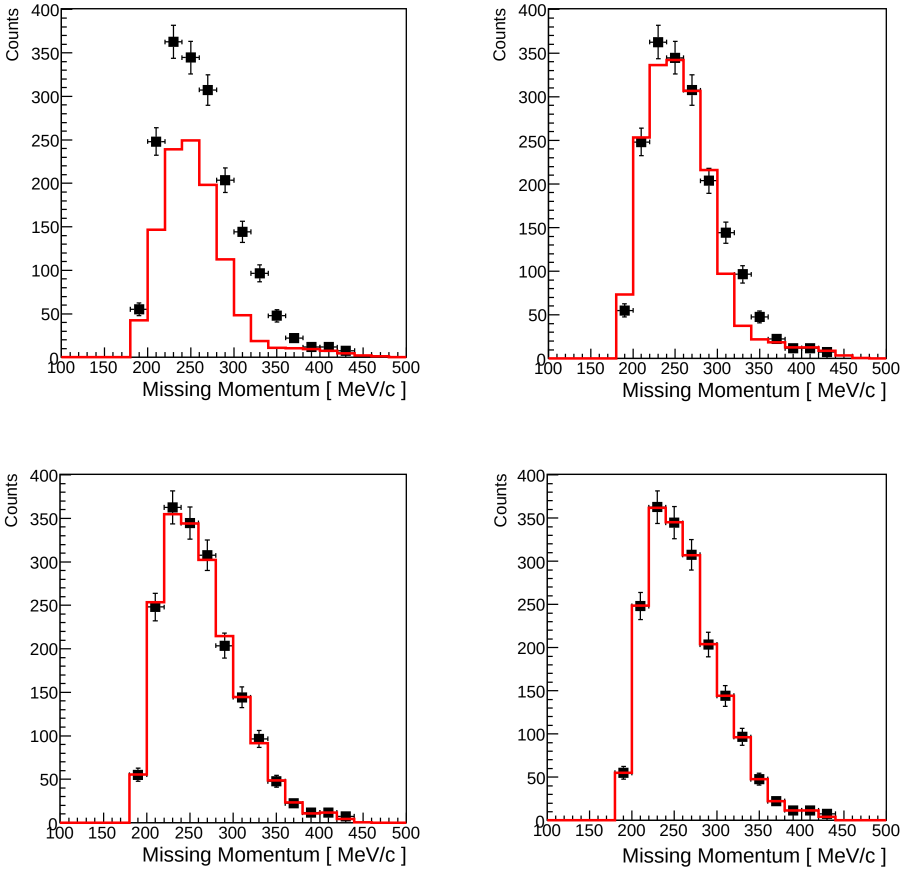

Figure 5-15: An illustration of how the simulation (red line) evolves after each iteration compared with the measured counts in the data (black squared). Note, error bars on the data are statistical only.

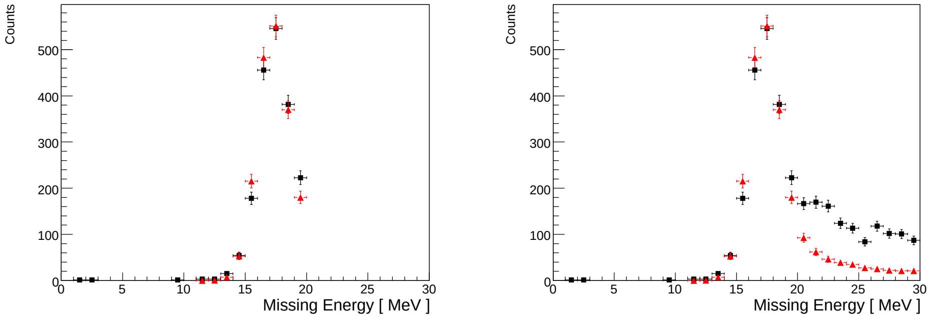

Figure 5-16: Comparison of the missing energy distribution for the data (black squares) and simulation (red triangles). Left plot shows the distribution with the cut at $E_{miss} = 20$ MeV to define the bound state dataset. Right plot shows the full data and simulation distribution; note how the radiative tail from the simulation contributes in the continuum region at higher missing energy values.

number of counts in the data for a given bin in both missing momentum and missing energy. Each missing energy and missing momentum bin, $B_{ij}(E^i_m, P^j_m)$ spans a range of values,

$$E_{miss} = E^i_m \pm \frac{\Delta E_m}{2} \;,\; P_{miss} = P^j_m \pm \frac{\Delta P_m}{2} \tag{5.10}$$

In order to have smoother variations of data between different bins, the width of each bin was chosen as $\Delta E_m = 20$ MeV and $\Delta P_m = 50$ MeV/c. The full range of missing energy and missing momentum spanned by each dataset was shown in Figs. 5-12, 5-13 and 5-14. Since the six-fold differential cross-section is defined as,

$$\frac{d^6\sigma}{d\Omega_e d\Omega_p dE_e dE_p} = E_p \, p_p \, \sigma_{cc2} \, S(\vec{p_m}, E_m) \tag{5.11}$$

the cross-section model in the simulation can be modified by revising the spectral function $S(\vec{p}_m, E_m)$; again the σ_{cc2} prescription of DeForest [30] is used for the single-nucleon offshell cross-section.

The simulation uses a representation of the input spectral function in the form of a two-dimensional rectangular grid in missing momentum and missing energy; this means the grid has a spectral function value for each missing energy and missing momentum point. For each simulated event, MCEEP performs a two-dimensional interpolation between the input grid points to determine the value of the spectral function at the particular values of missing energy and missing momentum of the simulated event. Since the continuum data has a distribution in both missing energy and missing momentum (see for example Figs. 5-12, 5-13 and 5-14), for each missing momentum bin there is a corresponding missing energy distribution. Therefore, for a chosen missing momentum bin P_m^j, functions are fitted to the missing energy distribution in both the data and simulation. In most cases a polynomial of 5th, 6th or 7th order was used, depending on which function produced the lowest χ^2 per degree of freedom value; a few distributions were better fit with a combination of Gaussian functions instead. Then, for the given missing momentum bin P_m^j, a new rational function is defined as,

$$F(E_m|P_m^j) = \left.\frac{f^{data}(E_m)}{f^{sim}(E_m)}\right|_{P_m^j} \tag{5.12}$$

where $f_k^{data}(E_m)$ and $f_k^{sim}(E_m)$ are the functions fitted to the data and simulation missing energy distributions respectively, for the given missing momentum bin P_m^j. Thus, for each dataset, there is a missing energy distribution for each missing momentum bin and so there will be a set of rational functions $F(E_m|P_m^j)$, with one for each missing momentum bin.

At each iteration, the cross-section model in the simulation is modified by changing the input spectral function using the set of rational functions, $F(E_m|P_m^j)$. The revised input spectral function is the product of the rational function and the previous input spectral function evaluated at the same missing energy, for a given missing momentum bin. So for iteration k, the new input spectral function is given by,

$$S_k(\vec{p}_m^j, E_m) = S_{k-1}(\vec{p}_m^j, E_m) \cdot F_k(\vec{p}_m^j, E_m) \tag{5.13}$$

Thus, the six-fold differential cross-section for the continuum data will finally be given by,

$$\frac{d^6\sigma}{d\Omega_e d\Omega_p dE_e dE_p} = E_p\, p_p\, \sigma_{cc2}\, S_0(\vec{p}_m^j, E_m^i) \prod_{k=1}^{k=n} F_k(\vec{p}_m^j, E_m^i) \tag{5.14}$$

where S_0 is the initial input spectral function and F_k is the rational function for missing momentum bin P_m^j, corresponding to the iteration k.

Contributions from Scattering to $^{12}C(e,e'p)^{11}B$ Excited States

The missing energy distribution for the data shown in Fig. 5-16, has a *shoulder* to the right of the bound state peak. This is likely due to proton knockout from carbon resulting in the boron nucleus being left in an excited state. The lowest three energy levels in boron-11 are 2.21 4.4 and 5.0 MeV respectively above the ground state; see Fig. 5-17. Given the energy resolution in the experiment is only ∼3 MeV, then it is likely that the large bound state peak in missing energy is due to a combination of the boron-11 nucleus being left in the ground state or the first excited state at 2.1 MeV. The shoulder which is observed in the data is then likely due to the boron-11 nucleus being left in the slightly higher 4.4 and 5.0 MeV excited states. These states cannot be resolved as their energy separation is smaller than the experimental resolution.

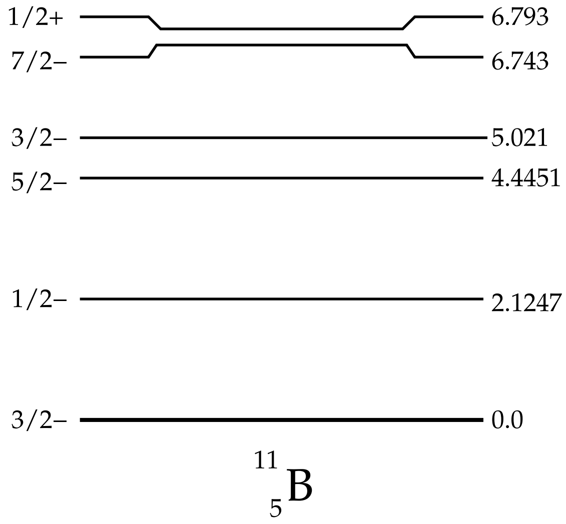

Figure 5-17: Nuclear shell energy level diagram for boron-11 showing the lowest lying levels above the ground state [8].

Further investigation of the events in the shoulder of the missing energy distribution showed that while there were insufficient statistics to make a reasonable cross-section extraction, the counts in this region did have an approximately 30% contribution to the $^{12}C(e,e'p)$ continuum data for kinematic I in the missing energy bin 20< E_m <40 MeV[1]. Therefore, when analysing kinematic I, both the contribution from the large bound state peak and the small shoulder were added to the continuum simulation and compared with the data.

The simulation was matched to the data for events in the shoulder by following the same procedure for iterating the model cross-section for the ground state peak. In this case, the simulation was compared with measured counts in the data after the counts from the ground state simulation were subtracted. A cut in the missing energy spectrum at 23 MeV was used to limit the dataset (to which the simulation was matched) to be just above the peak in events in the shoulder region. The resulting fitted simulations for the ground and excited states are shown in Fig. 5-18 along with the sum of both compared with the data.

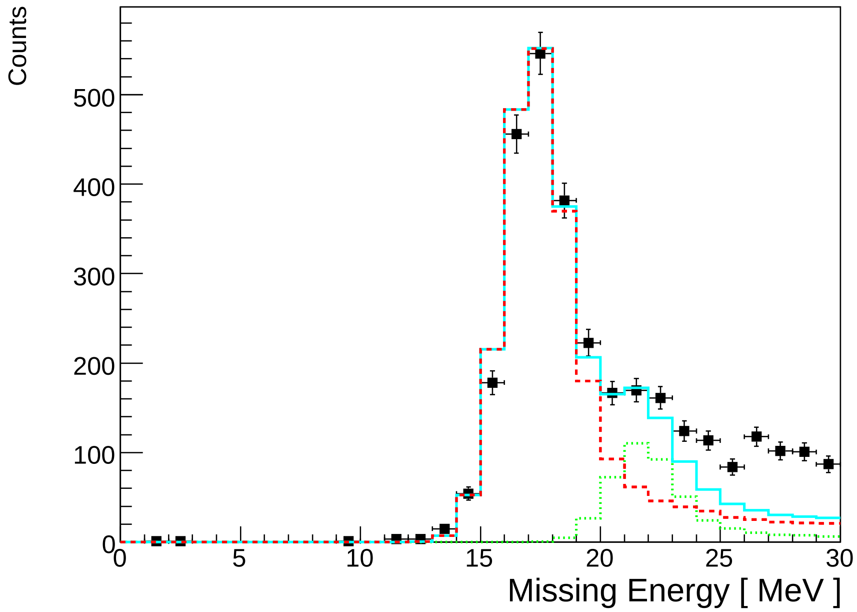

Figure 5-18: Missing energy distribution for the kinematic I bound states data. Dashed line (red online) is the simulated yield for the ground state of boron-11; dotted line (green online) is the simulated yield for the excited states at 4.4 and 5.0 MeV; solid line (blue online) is the sum of the ground and excited states simulations.

---

[1] The $^{12}C(e, e'p)$ continuum data was binned in 20 MeV wide bins in missing energy; bins of 50 MeV/c width in missing momentum were used as well.

5.6.3 Kinematic I: $\vec{P}_{miss} = 200 - 450$ MeV/c

The simulations for the ground and excited states which had been iterated to match the bound state data at low missing energies were then added to the continuum simulation for this kinematic. The total simulated yield was then compared with the data as a function of missing energy for each missing momentum bin. Using the procedure described in section 5.6.2, the cross-section model in the continuum simulation ONLY was then modified until the total (i.e. bound states simulations plus continuum simulation) simulated yield matched the data. The contributions for each simulation are shown compared with the data yield in Fig. 5-19. By including the simulated yields to the bound states, the events arising from the radiation tail in the bound states distributions are taken account of when iterating the model for the continuum cross-section. The comparison of the total simulated yield to the data yield for this kinematic is shown in Fig. 5-20.

5.6.4 Kinematic II: $\vec{P}_{miss} = 300 - 550$ MeV/c

After the continuum simulation for kinematic I was matched to the data, the resulting input spectral function to the data was used as the initial starting input spectral function for kinematic II. This kinematic did have some counts in data at low missing energies which may have been due to $^{12}C(e,e'p)^{11}B$ scattering. However, there were insufficient statistics to warrant a complete bound state simulation fit for this kinematic as there had been for kinematic I. Instead, ground and excited state simulations for this kinematic were run using the input momentum distributions which had been found for the simulations fit to the bound state data in kinematic I. The resulting contributions from the bound state simulations for this kinematic are shown as the dashed (green online) and dotted (blue online) lines in Fig. 5-21. Since the input momentum distributions were only valid upto a maximum missing momentum of 420 MeV/c, so there were no bound state simulations contributions at higher missing momentum bins.

The iteration procedure for modifying the model cross-section in the simulation

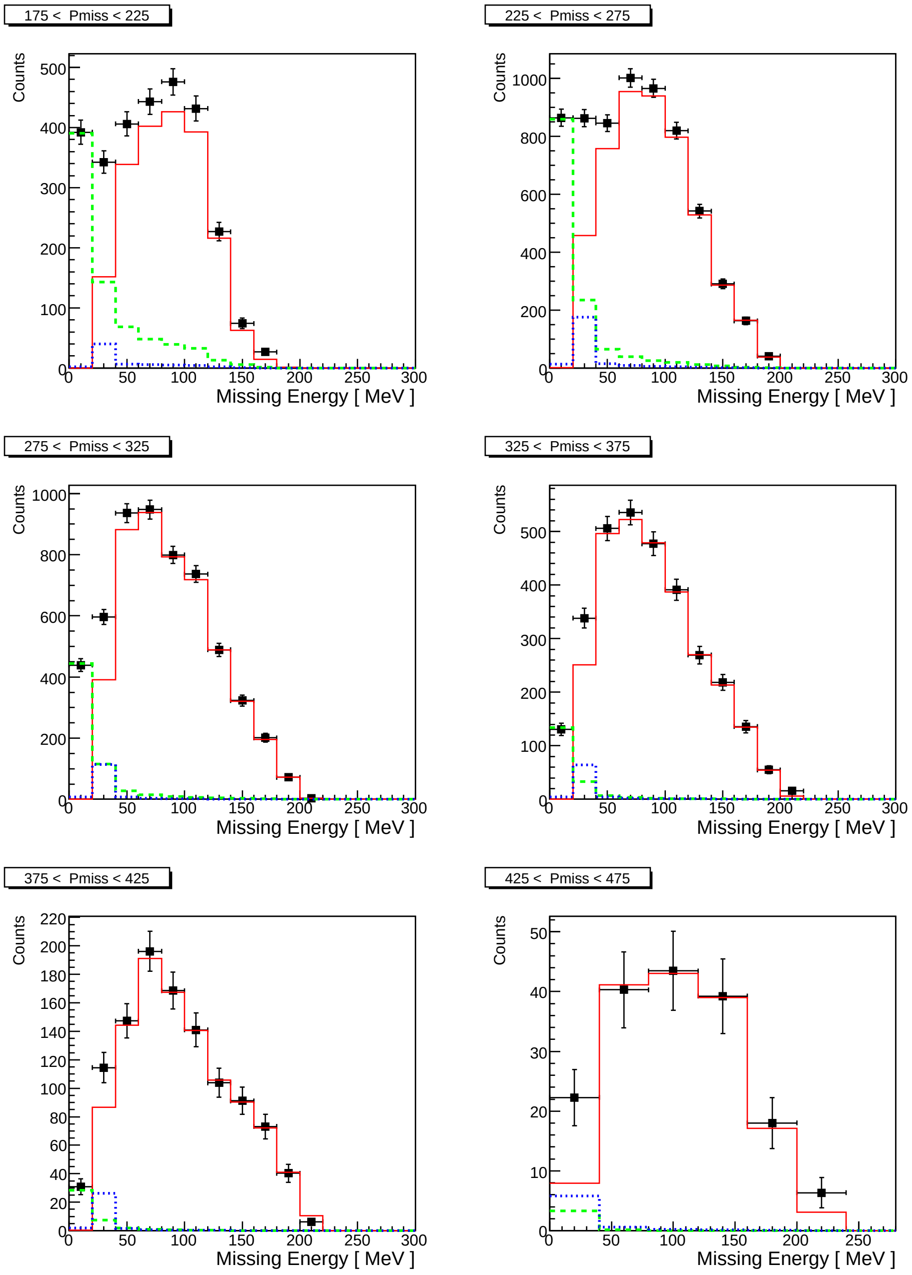

Figure 5-19: Kinematic I missing energy distributions for each missing momentum bin. Black squares are data. Solid line (red online) shows the continuum simulation yield. Dashed line (green online) shows the ground state simulation yield contribution. Dotted line (blue online) shows the excited state simulation contribution.

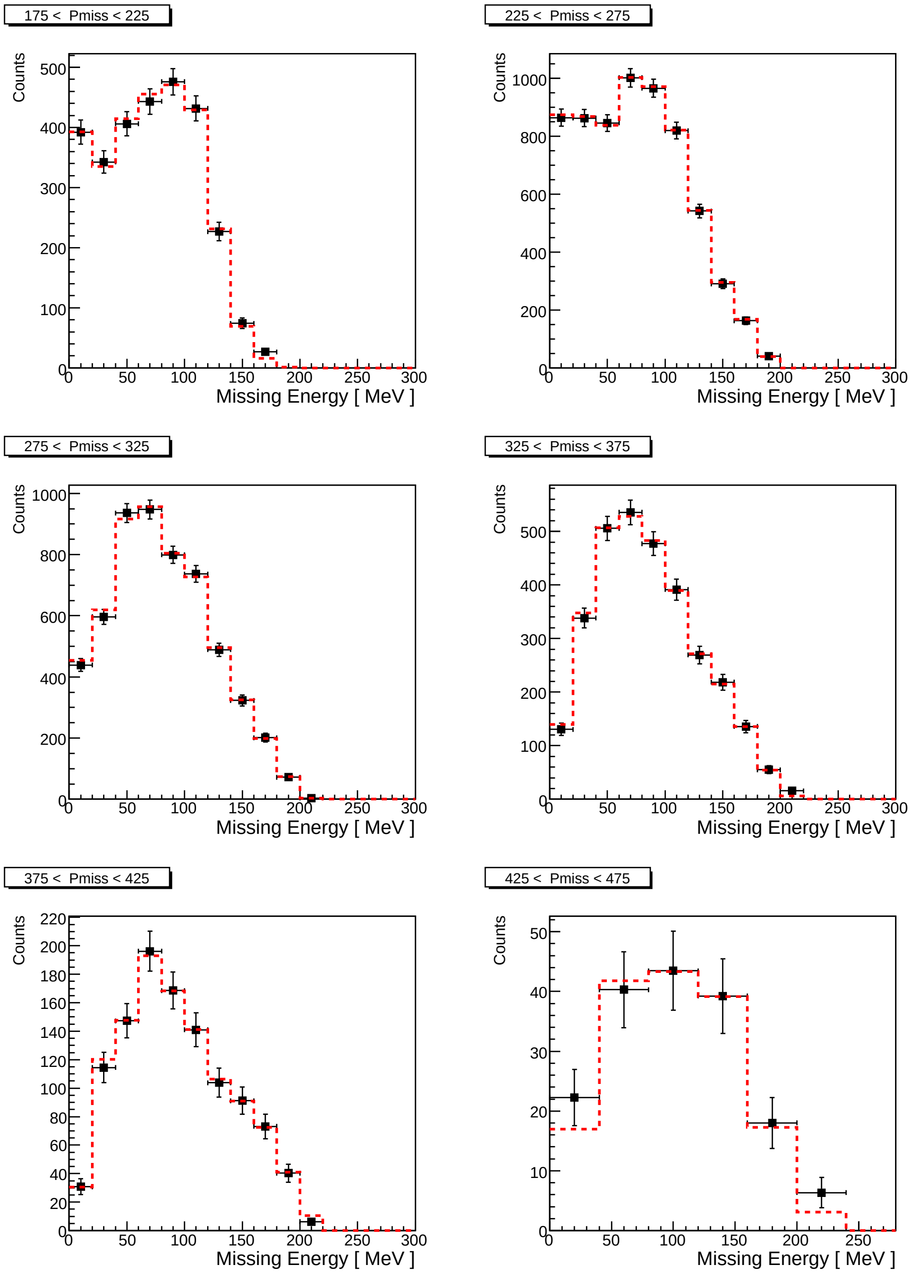

Figure 5-20: Kinematic I missing energy distributions for data compared with the total yield from continuum and bound state simulations summed together.

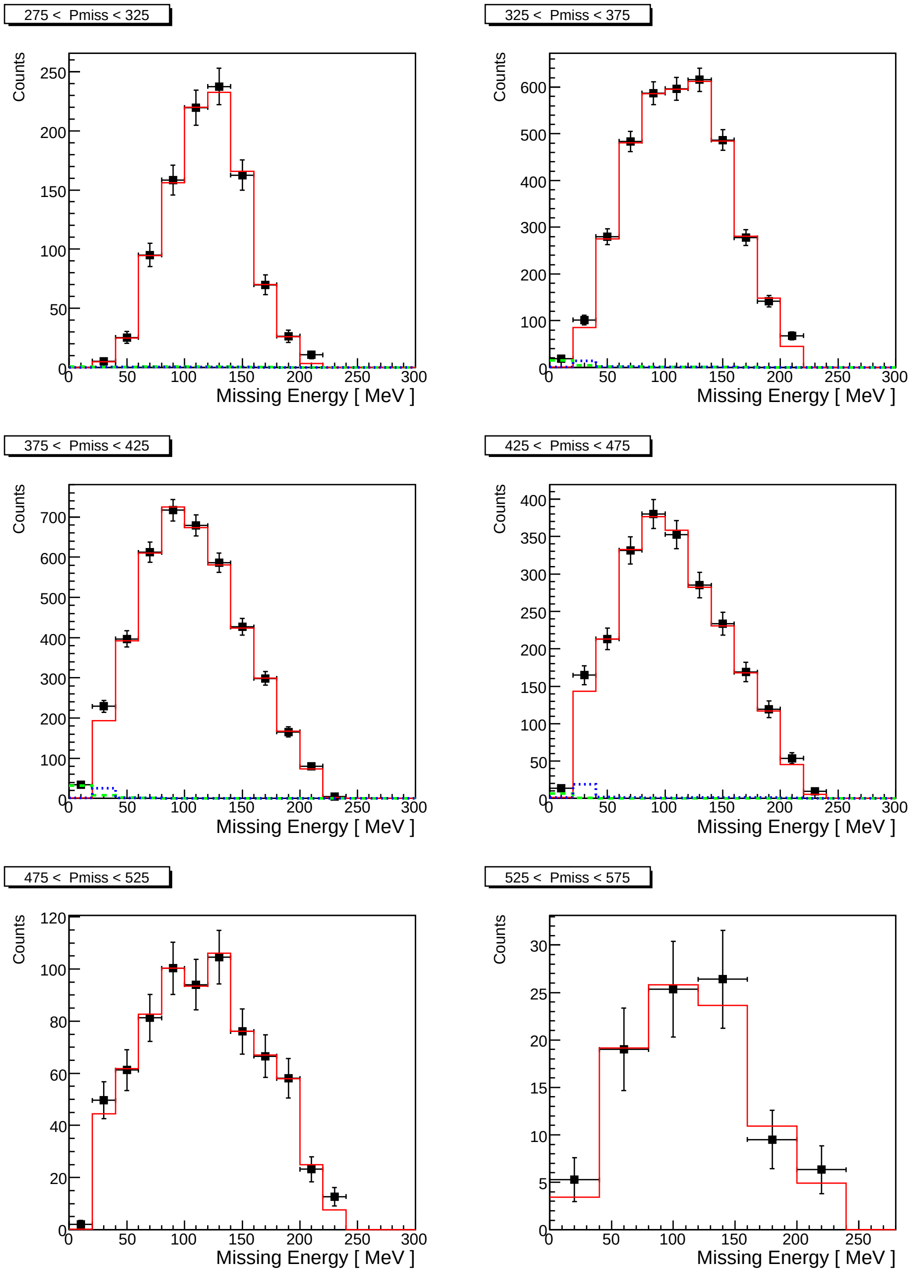

Figure 5-21: Kinematic II missing energy distributions for each missing momentum bin. Black squares are data. Solid line (red online) shows the continuum simulation yield. Dashed line (green online) shows the ground state simulation yield contribution. Dotted line (blue online) shows the excited state simulation contribution.

was repeated for the continuum simulation. The total simulated yield compared with the data for this kinematic is shown in Fig. 5-23.

5.6.5 Kinematic III: $\vec{P}_{miss} = 400 - 650$ MeV/c

The data for this kinematic did not have a small enough missing energy for any possible contributions from bound state scattering. Therefore, only a continuum simulation was compared with data and the iteration procedure repeated again. The initial input spectral function used was the resulting final input spectral function found after matching the simulation to data in kinematic II. For this kinematic, the resulting simulated yield is shown compared with the data in Fig. 5-23 after the iteration procedure was complete.

5.7 Radiative Corrections

In any electron scattering experiment, the incoming and outgoing charged particles radiate real and virtual photons which are not observed. This means the measured energies and momenta of the detected particles and hence, the extracted cross-sections, are modified by the energy lost to radiation effects. However, theoretical calculations do not include radiation effects. Thus, experimental data must be *radiatively unfolded*, producing a corrected spectrum which can then be compared with a suitable theoretical calculation.

The MCEEP simulation program was used to produce the radiative corrections for this experiment. The radiation effects included in MCEEP are primarily,

- *Internal Bremsstrahlung*: radiation is emitted during the interaction with the nucleus involved in the $(e, e'p)$ reaction.
- *External Bremsstrahlung*: radiation is emitted due to interaction with the Coulomb field of other nuclei in the target.
- *Ionisation Loss*: energy is lost through excitation or ionisation of atoms along the charged particles' path.

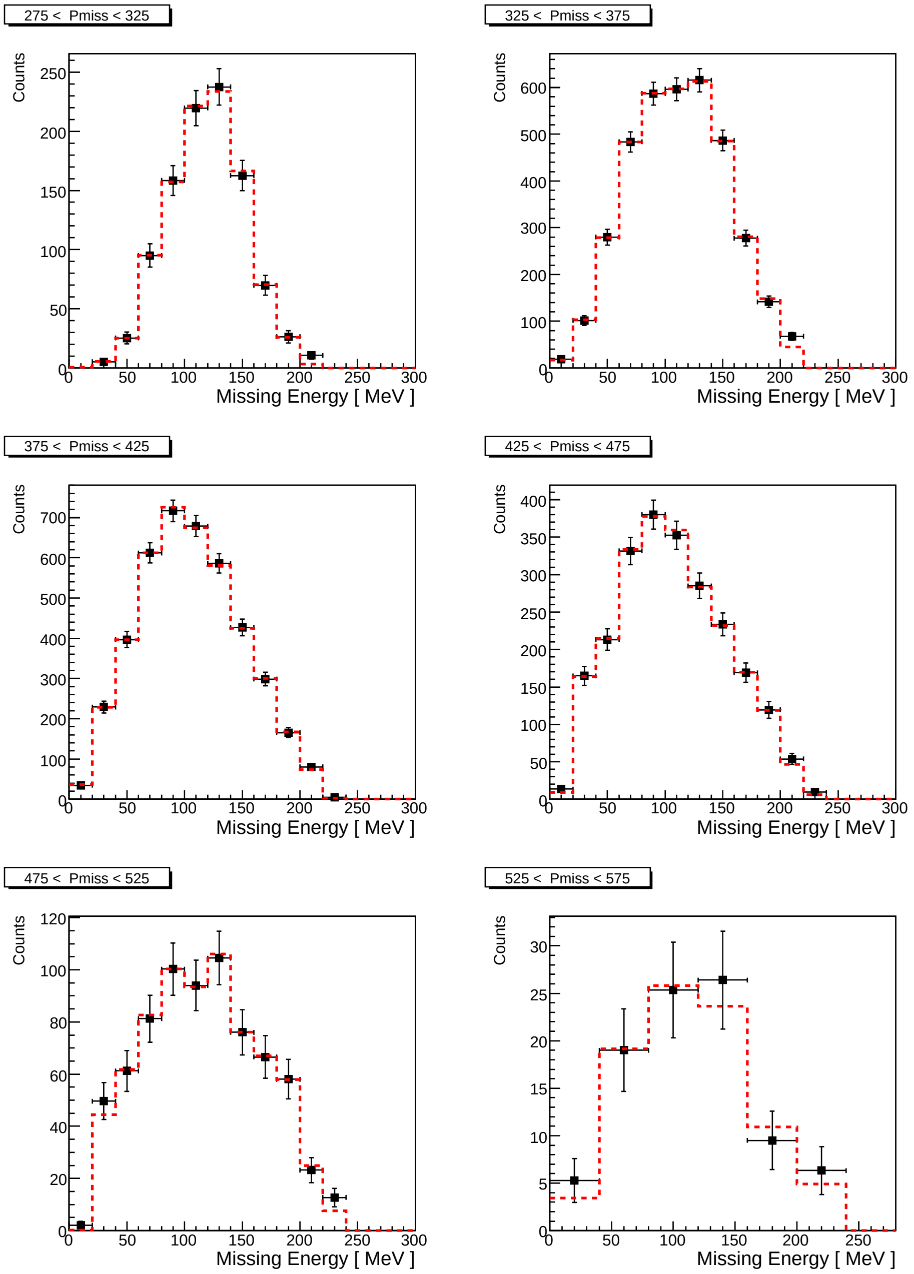

Figure 5-22: Kinematic II missing energy distributions for data compared with the total yield from continuum and bound state simulations summed together.

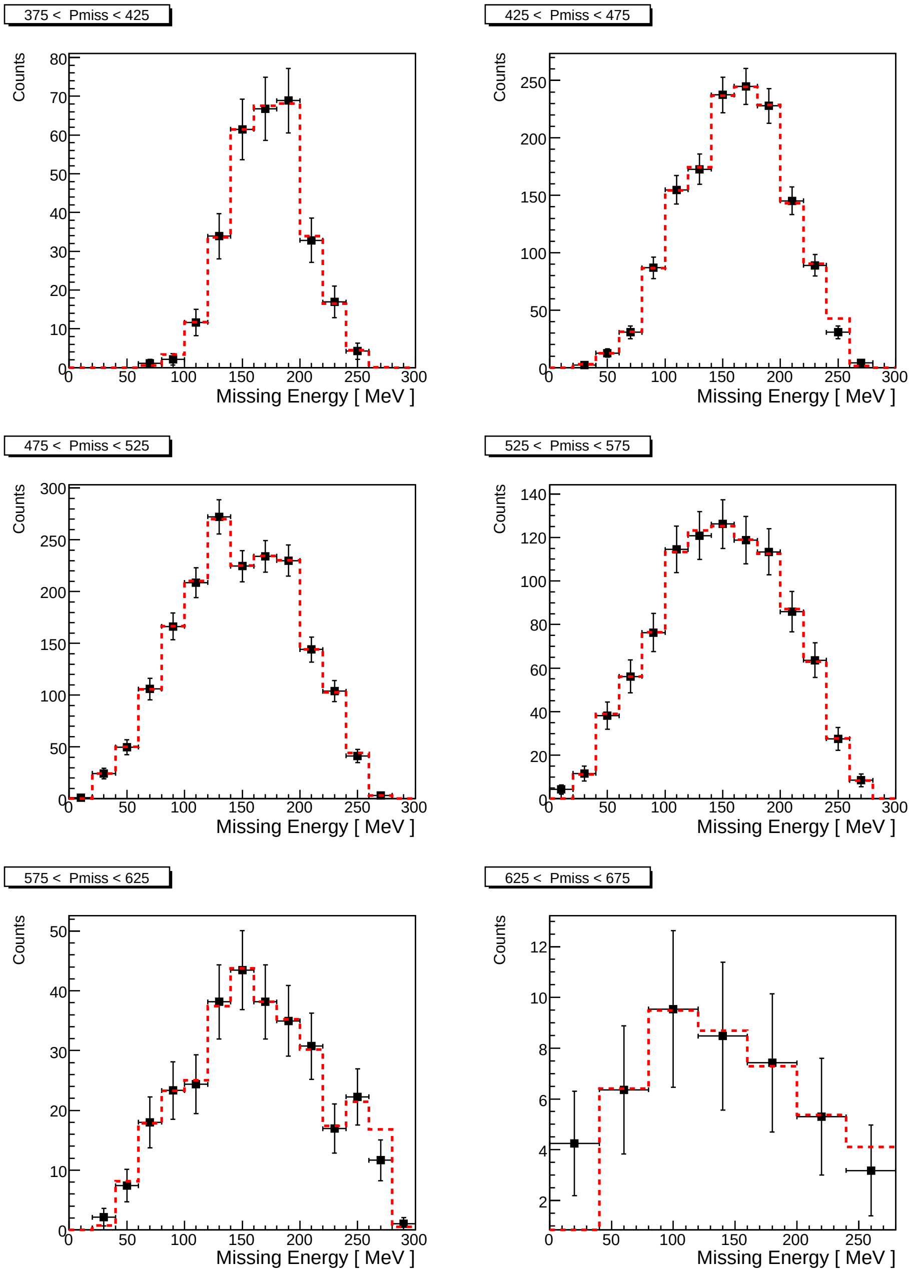

Figure 5-23: Kinematic III missing energy distributions for each missing momentum bin. Black squares are data points. Dashed line (red online) is the yield from the continuum simulation.

The energy lost to radiation from external bremsstrahlung and ionisation are considered as external radiation processes. The advantages of using the simulation to calculate the radiation effects are that the effects of acceptance-averaging the measured quantities is taken into account and also that the radiative correction can be calculated on an event-by-event basis.

5.7.1 Internal Bremsstrahlung

The internal bremsstrahlung is radiation emitted during the primary $(e, e'p)$ nuclear interaction and includes the radiation of both real and virtual photons. The real photons radiated can be classified as either *soft* or *hard*, depending on whether the photon energy is above (hard) or below (soft) a cutoff energy, ΔE. The cutoff energy is usually taken as the experimental energy resolution and so for this analysis $\Delta E = 3.0$ MeV. The emission of hard photons with energies above ΔE gives rise to the radiation tail.

The emission of soft and virtual photons is taken account of by the *Schwinger* correction [53]; this factor reduces the cross-section in kinematic bins for which the energy radiated away by real photons is less than ΔE, to account for energy lost to the radiative tail. The form of the Schwinger correction used is,

$$C_{Schwin} = e^{-\delta r}(1 - \delta_v) \tag{5.15}$$

where δ_r is the real photon contribution and δ_v is the virtual photon contribution; further details are given in [54]. The Schwinger correction is an overall multiplicative factor which is applied to the cross-sections evaluated without any radiation. This form of the correction neglects any radiation from hadrons in the reaction.

The radiative tail is calculated using the prescription of Borie and Drechsel [55]. Although the photons can be emitted in any direction, the *peaking approximation* is used, which assumes the photon is radiated along either the direction of the incident or scattered electrons. However, the prescription used is derived only to first order and so another correction to account for multiphoton emission is also included [56].

The multiphoton correction is a multiplicative factor which is calculated using the *unradiated* kinematics event-by-event and applied to the cross-section in the radiative tail. The multiphoton correction factor is given by,

$$f_{mp} = (1 - \delta_v)\frac{1 - e^{-\delta_r}}{\delta_r} \tag{5.16}$$

where δ_r and δ_v are the real and virtual photon contributions calculated for the Schwinger correction in eqn. 5.15.

5.7.2 External Radiation Processes

External bremsstrahlung occurs when charged particles are accelerated in the Coulomb field of nuclei other than the target nucleus. Energy is lost through radiation of photons and the amount lost depends on the thickness of the material traversed. MCEEP determines the thickness of material traversed in radiation lengths from randomly choosing the interaction vertex within the intersection of beam and target volumes. The resulting electron energy is determined using the probablity distribution for bremsstrahlung from a thin radiator determined by Tsai [57, 58].

The average energy loss through collisions is calculated using the Bethe-Bloch formula [59], including density and shell corrections, for both electrons and protons. However, the collision energy loss will have a distribution arising from fluctuations in the number of collisions and the actual amount of energy lost in each collision. The energy loss straggling distribution is approximated using either a Landau, Vavilov or Gaussian distribution depending on the ratio between the mean energy loss and the maximum possible energy transferable in a single collision. The energy lost to multiple scattering through small angles is calculated using a Gaussian approximation to the Moliere theory of Coulomb scattering [51].

The effect of radiative unfolding from the simulation fit to the data is shown in Fig. 5-24 for data in kinematic III in a particular missing momentum bin; the dashed line is the simulation yield with radiation included while the dotted line is the simulation yield after the radiation effects are removed. Fig. 5-24 shows how the yield distributions change, with larger numbers of counts at lower energy values when radiation is unfolded. The radiation effects cause data to have a larger measured missing energy and missing momentum values since energy is lost to radiation. When the radiation is unfolded, the counts in each kinematic bin are corrected for the number which were radiated out of that bin.

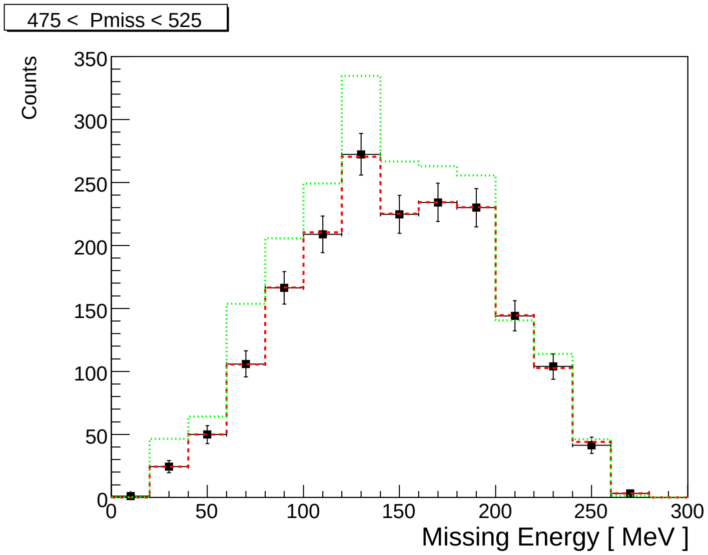

Figure 5-24: An example of the effect of radiation on the data and simulated yields; data are shown for a single missing momentum bin from kinematic III by the black squares. Dashed line (red online) is the yield from the radiated simulation which has been fitted to the data. Dotted line (green online) is the radiatively corrected simulation yield, from which the cross-section is extracted from. The dotted (green) line for the radiatively corrected simulated yield shows more counts at lower missing energy values as radiation causes events to have a larger missing energy and missing momentum values.

The resulting ratio of the non-radiated (corrected) simulation to the radiated simulation in Fig. 5-24 is shown in Fig.5-25. The radiation correction factor distribution varies between both missing energy and missing momentum bins in the same kinematic and also varies between different kinematics. The cross-section results are extracted from the non-radiated simulations after the iteration process of matching yields from the radiated simulations to the data have been completed.

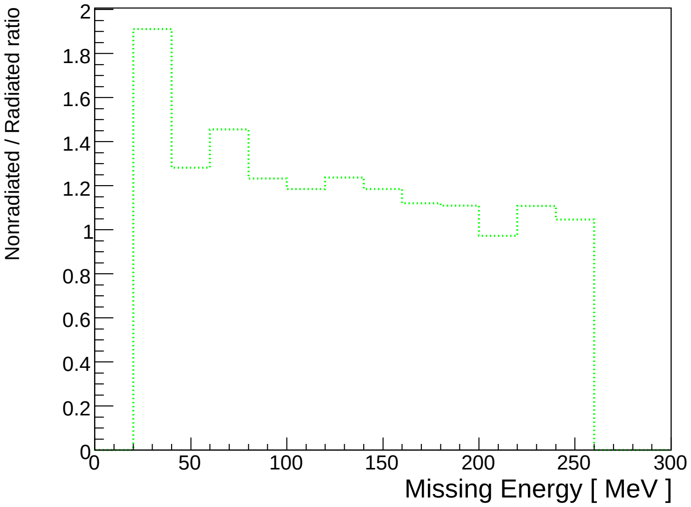

Figure 5-25: The ratio of the radiative corrected yield to non-corrected yield from Fig. 5-24, giving the radiation correction factor bin-by-bin in the missing energy distribution for the given missing momentum bin.

5.8 Systematic Uncertainies

There are several types of systematic uncertainties present in this analysis, namely *normalisation*, *kinematic* and *event selection* uncertainties. The normalisation uncertainties arise from quantities which are multiplicative in the cross-section calculation; for this analysis, these are the elastic cross-section determination ratio, luminosity, tracking efficiency corrections and radiative corrections; the systematic errors on these quantities are summarised in Table 5.2. The elastic cross-section determination error arises from the deviation of the elastic cross-section extracted from $^1H(e, e')$ elastic scattering data compared with the known elastic cross-section. This systematic error is the dominant error in the overall normalisation errors. The kinematic uncertainties arise from small variations in the kinematic quantities used in calculating the cross-section. These are evaluated using the *systerr* code [7] which works in conjunction with MCEEP to evaluate the effect of small variations in the energy and angles of the incoming electron beam, scattered electron and knocked-out proton. The event selection uncertainties arise from cuts used in the data analysis and the effect on the extracted cross-section when changing any of the cuts used.

The total systematic error is quoted for each data point in the tables of results in Section 6.6. The total value of the systematic error is the sum in quadrature of all the individual systematic errors for each data point. On all of the plots of results, two error bars are shown. The lower error bar is statistical only and the upper error bar is the sum in quadrature of the statistical plus systematic errors.

Quantity	Uncertainty
Elastic cross-section	4.5%
Luminosity	0.5%
Tracking	1.1%
Radiative Correction	1.0%
Total	4.77%

Table 5.2: Systematic normalisation uncertainties applicable throughout the data analysis; the total is the sum in quadrature of the individual normalisation uncertainties.

5.8.1 Uncertainties in the $^{12}C(e,e'p)^{11}B$ Analysis.

The systematic uncertainties for each data point arising from the event selection cuts used are evaluated by changing the cut in the missing energy distribution to define the bound state data to which the simulation was then fit; the cut was changed by ± 1 MeV and the cross-sections re-evaluated. The relative difference between the cross-section extracted from each of the fits using the modified missing energy cut, to the original extracted cross-section value was calculated. Then for each data point, the systematic error due to changing the missing energy cut was taken as the average of the relative differences.

A second systematic error due to event selection arose from the acceptance cuts applied to the in-plane, out-of-plane angles and momentum acceptance of the electrons and protons detected in the HRS. This systematic error was evaluated for each data point by changing the acceptance cuts and re-evaluating the cross-sections; the acceptance cuts were modified by ±10% in the θ, ϕ and δ variables for each spectrometer. Again the systematic error value was taken as the average of the relative difference of each of the revised set of acceptance cuts with the original extracted cross-section.

The total systematic error quoted is the sum in quadrature of all systematic error values, including the normalisation systematic errors quoted in Table 5.2.

5.8.2 Uncertainties in the $^{12}C(e, e'p)$ Continuum Analysis

The cross-section was extracted for separate fits of the simulation to the data for the two limiting $\omega - y$ cuts (see for example Fig. 5-10). Then the relative differences of the resulting cross-sections were evaluated against the original extracted cross-section. The average of these two relative errors was taken as the systematic error value for each data point arising from the location of the two-dimensional cut on $\omega - y$.

Similarly, the effect of modifying the acceptance cuts applied to the θ, ϕ and δ variables for both spectrometers by $\pm 10\%$ was also evaluated. The relative difference between the original extracted cross-section and the cross-section for the revised acceptance cuts was determined for each data point. The average of the two resulting relative errors was taken as the systematic error for each point due to the acceptance cuts used.

The total error quoted is the sum in quadrature of all systematic errors for that particular missing momentum bin, including the normalisation systematic errors quoted in Table 5.2.

Chapter 6

Experimental Results

The analysis methods described in the previous chapter were used to extract the $^{12}C(e,e'p)$ cross-sections for the two-body breakup and continuum reaction channels. The kinematic settings for each dataset are summarised in Table 5.1. The results are presented in the following order: the five-fold differential cross-section and extracted distorted momentum distribution for the $^{12}C(e,e'p)^{11}B$ reaction; the six-fold differential cross-sections for the $^{12}C(e,e'p)$ continuum reaction; the distorted spectral functions extracted from the continuum cross-section results; a comparison of reduced cross-sections for overlapping kinematic bins between each dataset; tabulated results of the extracted cross-sections and spectral functions. The systematic errors are discussed in section 5.8.

6.1 $^{12}C(e,e'p)^{11}B$ Cross-section Results

The cross-section for the $^{12}C(e,e'p)^{11}B$ reaction was extracted using the procedure described in Section 5.6.1. The cross-section as a function of missing momentum is shown in Fig. 6-1 and compared with theoretical calculations courtesy of J. M. Udias [60]. The solid curve (red online) is the result of a fully-relativistic mean field calculation with final state interactions calculated using a phenomenological optical potential [61] to determine the wavefunction of the outgoing particle. The calculation is described as being *fully-relativistic* because it uses a relativistic formalism for the electron and proton interaction vertices; the formalism is described in detail in [9]. The dashed curve (blue online) is for a plane wave impulse approximation calculation.

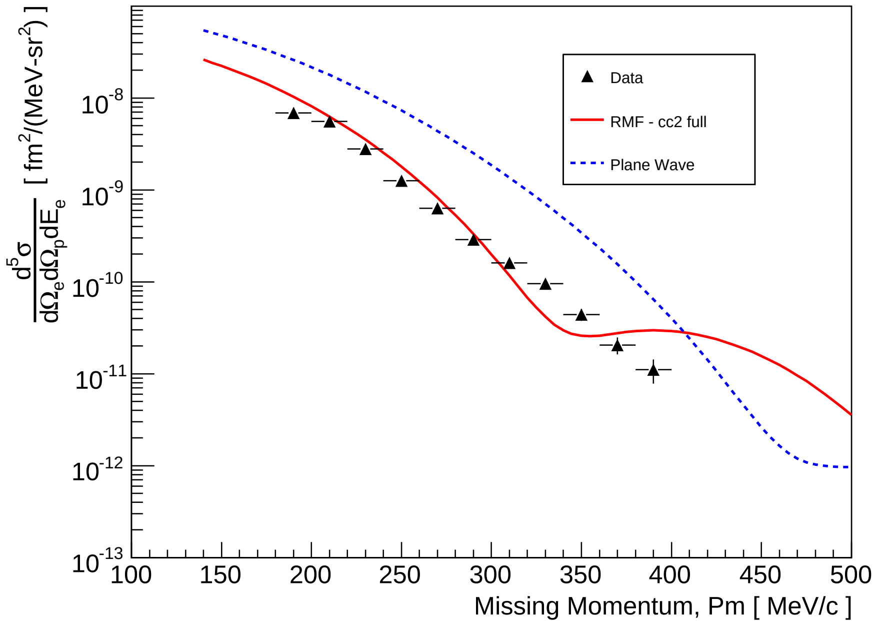

Figure 6-1: Five-fold differential cross-section extracted for the kinematic I data as a function of missing momentum. The solid curve (red online) is a fully-relativistic mean field theoretical calculation; the dashed curve (blue online) is plane wave impulse approximation calculation. Data shows good agreement with the relativistic calculation for $P_m < 300$ MeV/c but disagrees at larger momenta. Both theoretical calculations are courtesy of J. M. Udias [9].

The relativistic mean field calculation shows good agreement with the data for $P_{miss} < 300$ MeV/c but deviates from the data for larger missing momenta values. The plane wave impulse approximation calculation does not agree with the data at all and predicts a significantly larger cross-section than the relativistic calculation at lower missing momenta. One contributing factor is that the relativistic calculation includes the effects of final state interactions, while the plane wave calculation does not. The observed agreement between the relativistic calculation and the data for $P_{miss} < 300$ MeV/c demonstrates the importance of final state interactions in the reaction. The lack of agreement between the experimental cross-section and the theoretical calculations for $P_{miss} > 300$ MeV/c indicates that there are processes occuring which are not taken account of by the calculations. Given the extreme set of kinematics used for this experiment, it is not surprising that the plane wave calculation does not agree with the data. The relativistic mean field calculation shows an increase in cross-section strength at higher missing momenta values ($P_{miss} >$ 400 MeV/c) which theorists have attributed to the effect of short-range correlations. Unfortunately, there are no data above 400 MeV/c to compare with, although the trend appears to be decreasing monotonically. The data in the second kinematics had insufficient statistics at low missing energy to extract the bound state cross-section.

6.1.1 Extracted Momentum Distribution

Assuming the plane wave impulse approximation model, the extracted five-fold differential cross-section can be factorised as,

$$\frac{d^5\sigma}{d\Omega_e d\Omega_p dE_e} = K\sigma_{cc2} n(P_m)\delta(E_m - E_{bound}) \tag{6.1}$$

where the delta function arises from the integral of the spectral function (see eqn. 5.7); σ_{cc2} uses the DeForest prescription of the single-nucleon offshell cross-section [30]. The experimental distorted momentum distribution can be extracted from the cross-section by dividing out the kinematic factor and the single-nucleon offshell cross-section. This was accomplished by running a MCEEP simulation (previously described in Section 5.5) for a unit input momentum distribution with all other input parameters kept identical to those used for the cross-section extraction. The *unit* cross-section obtained is then acceptance averaged in the same way as the extracted experimental cross-section. Then the distorted momentum distribution was extracted as,

$$n_{distorted}(P_m) = \left\langle \frac{d^5\sigma}{d\Omega_e d\Omega_p dE_e} \right\rangle_{exp} / \, \langle K\sigma_{cc2} \rangle_{unit} \tag{6.2}$$

The acceptance averaged unit cross-section is shown in Fig. 6-2. Dividing the extracted experimental cross-section by the unit cross-section - $K\sigma_{cc2}$ - produces the experimental distorted momentum distribution, which is shown in Fig. 6-3. A reduced cross-section can be obtained in the same manner from the theoretical cross-section calculation, by dividing the theoretical curve by the same unit cross-section as the data. The resulting reduced cross-section obtained from the theoretical calculated cross-sections are compared with the reduced cross-section (or the distorted momentum distribution) extracted from the data in Fig. 6-3. The extracted distorted momentum distribution (black data points) does agree with the reduced cross-section from the relativistic theoretical calculation (solid line—red online) for $P_m < 300$ MeV/c, but deviates at larger momentum. This is the same trend observed in the cross-section comparison. Unfortunately, the data does not extend beyond 400 MeV/c in missing momentum, otherwise, it would be interesting to see if there is a change in shape of the experimental momentum distribution. The tabulated results for the $^{12}C(e,e'p)^{11}B$ reaction are given in Table 6.1. As well as the cross-section and momentum distribution values, the average Q^2 and ω values for each missing momentum bin are given as well. Note the statistical and systematic errors for the extracted momentum distribution values are the same as those for the cross-section and thus are only quoted once for each data point.

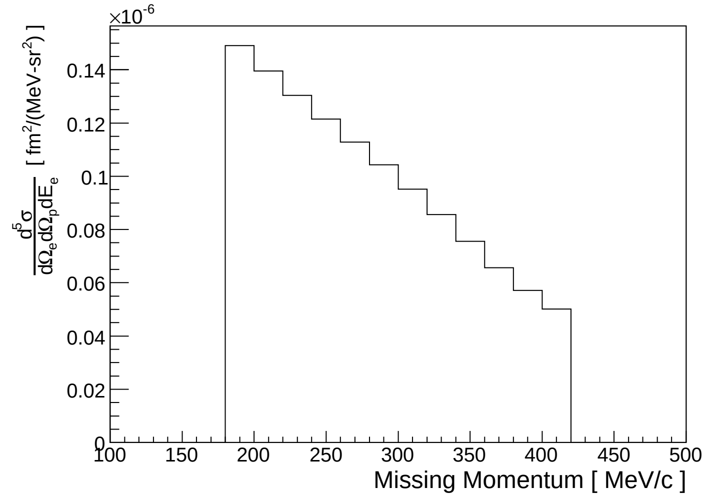

Figure 6-2: Acceptance averaged unit cross-section, $K\sigma_{cc2}$, used as a divisor of the experimental extracted cross-section to produce the extracted distorted momentum distribution.

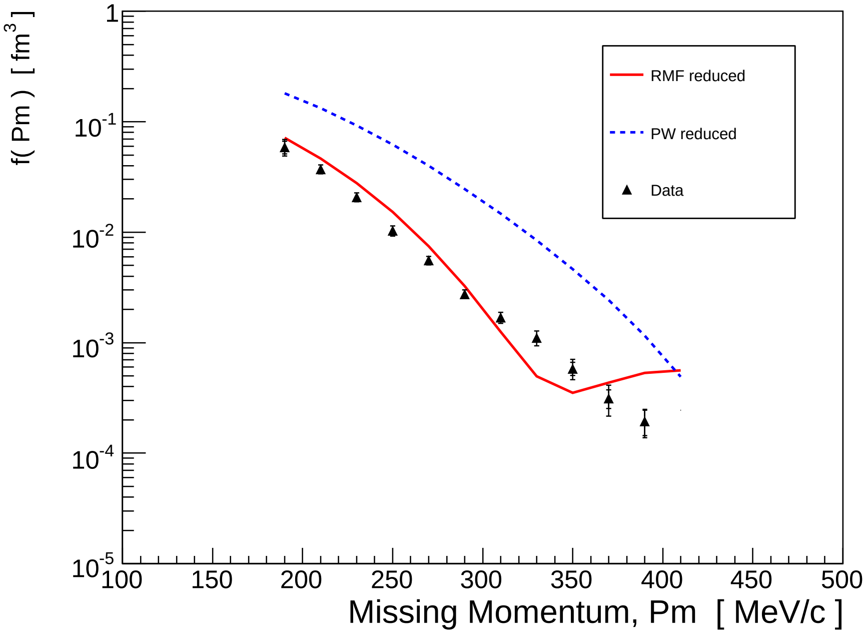

Figure 6-3: Extracted distorted momentum distribution from kinematic I data for $^{12}C(e,e'p)^{11}B$ reaction. The solid line (red online) is the reduced cross-section from the relativistic mean full calculation of the cross-section. The dotted line is the reduced cross-section for the plane wave calculation.

P_{miss} $[MeV/c]$	$\frac{d^5\sigma}{d\Omega_e d\Omega_p dE_e} \pm \delta_{stat} \pm \delta_{sys}$ $[fm^2/(MeV-sr^2)]$	$n(P_m)$ fm^3	$\bar{Q}^2 \pm \sigma_{Q^2}$ $[(GeV/c)^2]$	$\bar{\omega} \pm \sigma_\omega$ $[MeV]$
190	6.8905e-09 ± 13.1% ± 10.9%	0.04624	1.697 ± 0.018	851.1 ± 4.3
210	5.5654e-09 ± 6.2% ± 7.1%	0.03989	1.715 ± 0.031	846.1 ± 8.2
230	2.7860e-09 ± 5.0% ± 7.7%	0.02136	1.737 ± 0.043	841.2 ± 12.4
250	1.2616e-09 ± 5.2% ± 9.2%	0.01039	1.760 ± 0.057	835.6 ± 16.6
270	6.3154e-10 ± 5.5% ± 6.8%	0.005597	1.784 ± 0.070	828.9 ± 20.8
290	2.8967e-10 ± 6.8% ± 4.9%	0.002777	1.812 ± 0.083	822.1 ± 24.1
310	1.6079e-10 ± 8.0% ± 7.9%	0.001690	1.849 ± 0.098	816.4 ± 26.1
330	9.522e-11 ± 9.5% ± 12.1%	0.001111	1.890 ± 0.112	812.1 ± 27.0
350	4.4083e-11 ± 13.2% ± 16.2%	0.0005830	1.946 ± 0.125	809.8 ± 27.6
370	2.0564e-11 ± 19.0% ± 24.4%	0.0003133	2.009 ± 0.134	808.8 ± 27.7
390	1.1096e-11 ± 26.0% ± 12.1%	0.0001941	2.085 ± 0.133	808.4 ± 27.5

Table 6.1: Results for $^{12}C(e,e'p)^{11}B$ reaction in kinematic I; statistical and systematic errors are given for each data point; errors on the Q^2 and ω values are the standard deviation of the distribution for that missing momentum bin.

6.2 $^{12}C(e,e'p)$ Continuum Cross-section Results

Using the methods described in Section 5.6.2, the cross-section for the $^{12}C(e,e'p)$ continuum reaction has been extracted for each of the three kinematic settings used in the experiment. The yield, phase-space and resulting cross-section distributions (all radiatively corrected) are shown in three-dimensional plots in Fig. 6-4 (kinematic I), Fig. 6-5 (kinematic II) and Fig. 6-6 (kinematic III). The extracted cross-sections for each dataset are shown in Figs. 6-10, 6-11 and 6-12. These figures show the cross-section extracted for each missing momentum bin as a function of missing energy; the values of the Bjorken-X and y scaling variables are also shown for each missing momentum bin.

The motivation for this experiment was to measure short-range nucleon-nucleon correlations through a triple coincidence experiment. As described in Section 2, the simple reaction mechanism assumes that two nucleons spatially close together inside the nucleus form a nucleon-nucleon pair; these nucleons have an equal and opposite momentum in the center-of-mass which increases as the nucleon-nucleon separation decreases. An electron scattering off a proton belonging to such a nucleon pair will transfer energy ω and momentum $\vec{q}$. Then, in the plane wave impulse approximation (PWIA) all final state interactions are neglected. Neglecting the momentum of the pair relative to the residual nucleus, the knocked-out proton has momentum $\vec{P}_p = \vec{q} - \vec{P}_m$ and the partner nucleon recoils in the opposite direction with momentum equal to the missing momentum $\vec{P}_m$. This model is sometimes referred to as scattering from a *quasideuteron* - i.e. a proton-neutron pair [62]. In this model, the recoil partner nucleon and the (A-2) spectator nucleons which are assumed to be at rest form the recoiling system. The mass of this recoiling system is then given by,

$$M^2_{recoil} = \left[M_{A-2} + \sqrt{m_N^2 + p^2_{recoil}}\right]^2 - p^2_{recoil} \tag{6.3}$$

where M_{A-2} is the mass of the spectator (A-2) system, m_N and p_{recoil} are the mass and momentum of the recoil partner nucleon of the pair. This means that in PWIA, a signature for short-range correlations will be a peak in the continuum cross-section

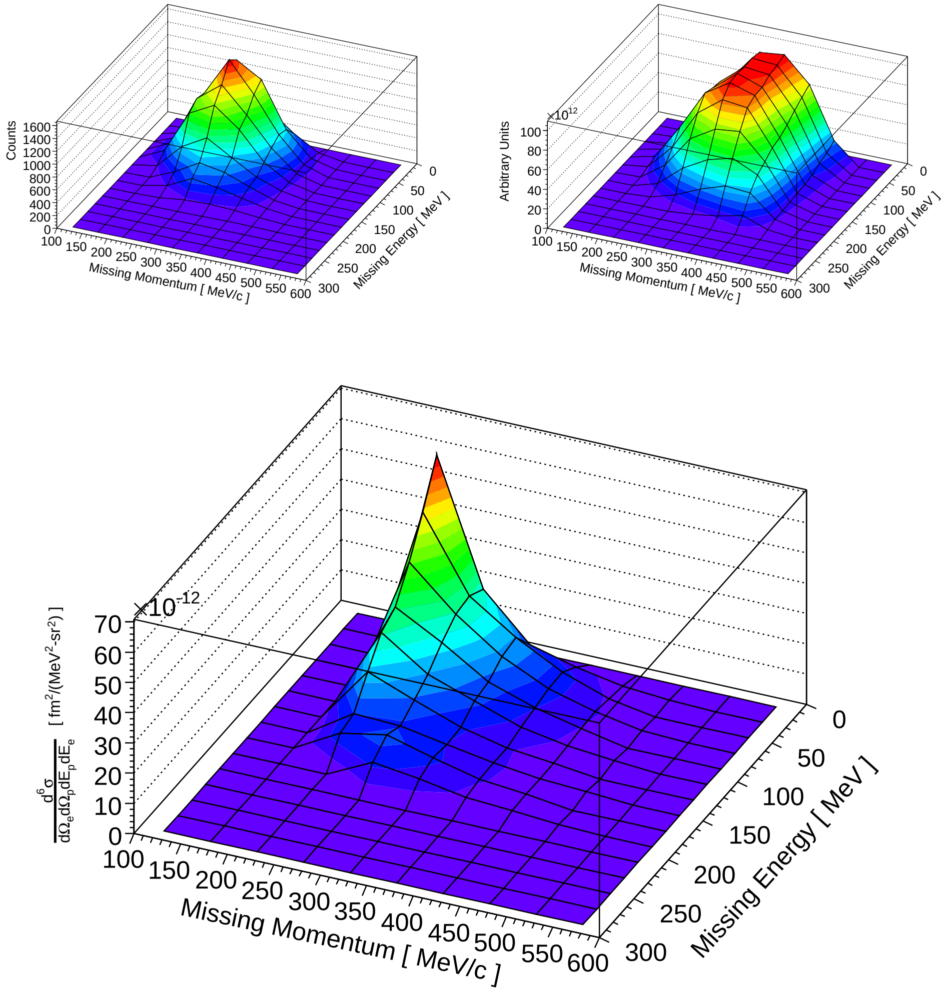

Figure 6-4: Three dimensional plots of yield (upper left), phase space (upper right) and cross-section (lower plot) extracted from MCEEP for kinematic I continuum data.

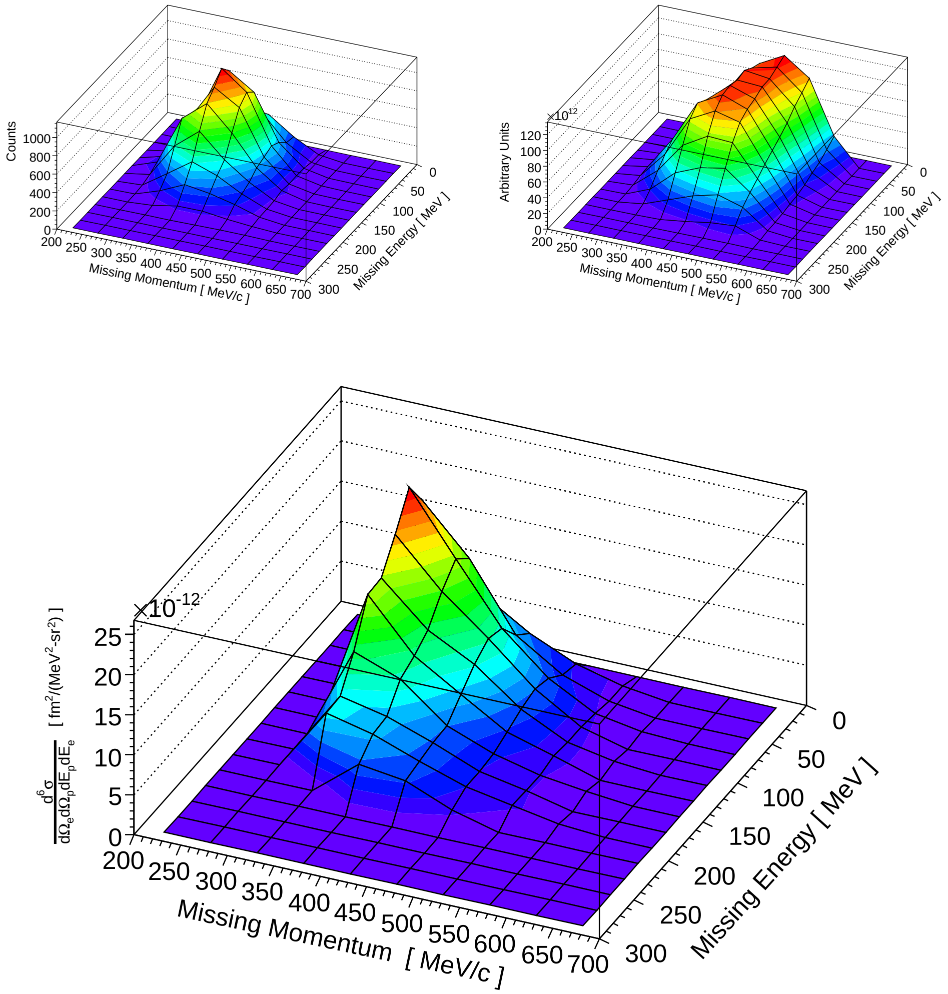

Figure 6-5: Three dimensional plots of yield (upper left), phase space (upper right) and cross-section (lower plot) extracted from MCEEP for kinematic II continuum data.

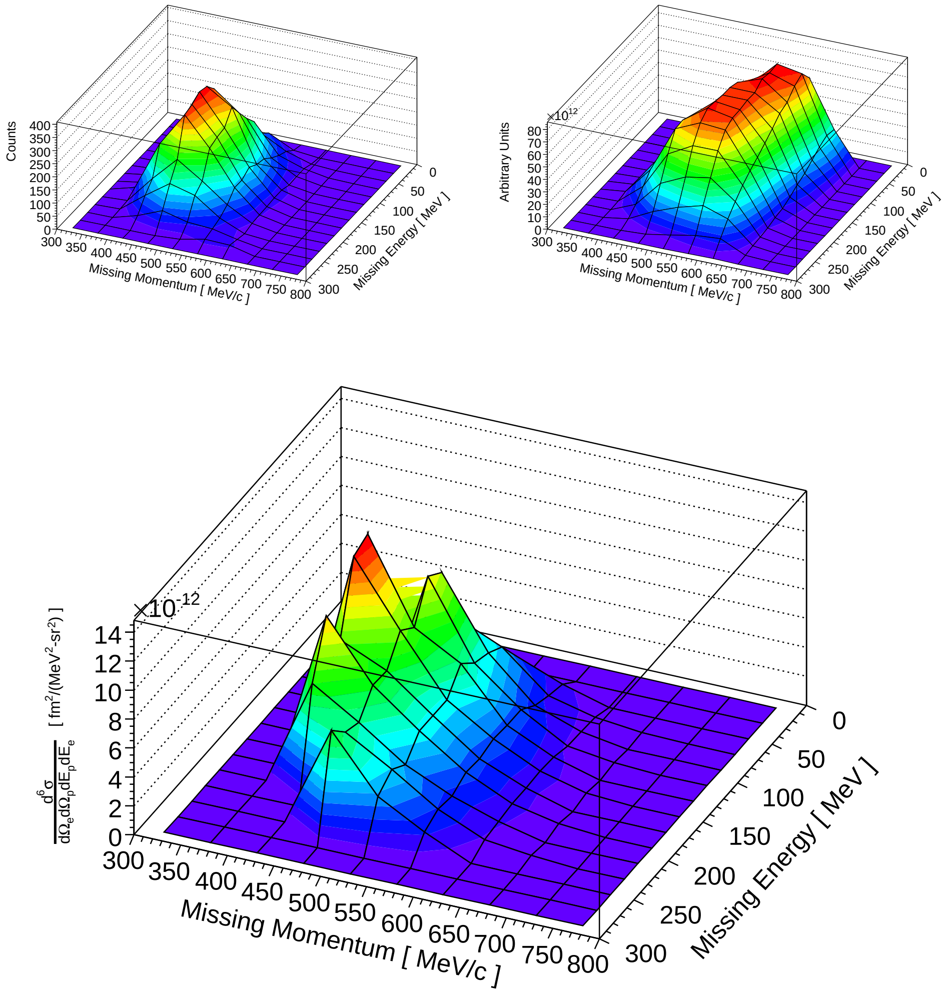

Figure 6-6: Three dimensional plots of yield (upper left), phase space (upper right) and cross-section (lower plot) extracted from MCEEP for kinematic III continuum data.

as a function of missing energy, with the peak location dependent on the momentum of the partner recoil nucleon, p_{recoil}. Following the kinematic definitions given in Section 2.5.1, the missing energy is given by,

$$E_{miss} = M_{recoil} + m_p - M_A \tag{6.4}$$

where M_A is the target mass and m_p is the mass of the proton knocked out and detected in the $(e, e'p)$ reaction; so the peak location in terms of missing energy can be calculated from kinematics. Previous experiments at both Saclay [63, 62] and JLab [3] on ^3He and ^4He have observed such a peak in the cross-section; the peak location was usually in reasonable agreement with missing energy values predicted by this quasideuteron model, assuming $\vec{P}_{recoil} = \vec{P}_{miss}$. An example was shown earlier in Fig. 2-3.

Using eqns. 6.6 and 6.4, the expected peak location for the extracted $^{12}C(e, e'p)$ continuum cross-sections has been calculated and is shown on Figs. 6-10, 6-11 and 6-12 by the solid (red online) arrow. As can be seen, as the missing momentum increases, the expected and actual peak locations begin to diverge. This model assumes that the residual (A-2) system is at rest and that the recoiling partner nucleon has momentum equal to the missing momentum of the reaction. Therefore, an improvement to the model would be to assume that $\vec{P}_{recoil} \neq \vec{P}_{miss}$ and $\vec{P}_{A-2} \neq 0.0$, i.e. that the (A-2) nucleons are not simply at rest—the (A-2) system may act as a spectator in the sense that it does not take part in the interaction, but still carries a non-zero momentum. Thus, the mass of the recoil (A-1) system can be rewritten as,

$$M^2_{recoil} = \left[\sqrt{M^2_{A-2} + p^2_{A-2}} + \sqrt{m^2_N + p^2_{recoil}}\right]^2 - p^2_{miss} \tag{6.5}$$

However, the momentum of the recoil partner nucleon was measured by the BigBite spectrometer and neutron detector in the triple coincidence reaction. The results for the $^{12}C(e, e'pn)$ channel are shown for kinematic III data in Fig. 6-7. The upper plot shows the distribution of neutron momenta determined from the neutron time-of-flight measured in the neutron detector. The lower plot shows the distribution of neutron momenta assuming it is equal to the missing momentum $\vec{P}_{miss} = \vec{q} - \vec{P}_p$ defined for the $(e, e'p)$ reaction. The distribution of momenta in the lower plot assuming $\vec{P}_n = \vec{P}_{miss}$ is determined by the corresponding missing momentum value measured from the electron and proton detected in the HRS spectrometers for each neutron arising from the $(e, e'pn)$ reaction which is detected in the neutron detector. The results show that the measured neutron momentum is not equal to the missing momentum; the peak in the measured distribution (upper plot of Fig. 6-7) occurs at $\sim 80\%$ of the peak location in the missing momentum distribution.

The analyses of the $^{12}C(e, e'pn)$ and $^{12}C(e, e'pp)$ reaction channels [10, 11] determined the cross-section ratios (relative to the $(e, e'p)$ reaction) and extrapolated them for the limited acceptance in BigBite and the neutron detector to account for all possible nucleon-nucleon pairs available. The results for kinematic III data are shown in Fig. 6-8. Combining the two ratios gives (within errors) unity, suggesting that for each $(e, e'p)$ event, a recoil partner nucleon was also emitted from the nucleus. This means that the extracted cross-section for the $(e, e'p)$ reaction should be dominated by short-range correlation effects since a recoil partner nucleon is also being ejected from the nucleus. The fact that the expected location of the peak in the cross-section is not predicted by the simple quasideuteron model may indicate that the reaction mechanism is more complicated than the mechanism upon which the quasideuteron model is based.

To illustrate the effect of assuming $\vec{P}_{recoil} \neq \vec{P}_{miss}$, the calculation of expected peak location was repeated using the simple assumption that $\vec{P}_{recoil} = 0.8\vec{P}_{miss}$; this is a crude approximation motivated by the results shown in Fig. 6-7. This also means that $\vec{P}_{A-2} \neq 0.0$. In Figs. 6-10, 6-11 and 6-12, the dashed (green online) arrow shows the expected location in missing energy of the cross-section peak assuming the (A-2) system is not a spectator at rest and $\vec{P}_{recoil} = 0.8\vec{P}_{miss}$. In each case, the expected peak location has moved to lower missing energy values; for some cross-section distributions this improves the agreement with the cross-section peak.

A further revision to this model can be made by including any excitation energy the (A-2) system might have. This means the equation for the mass of the recoil

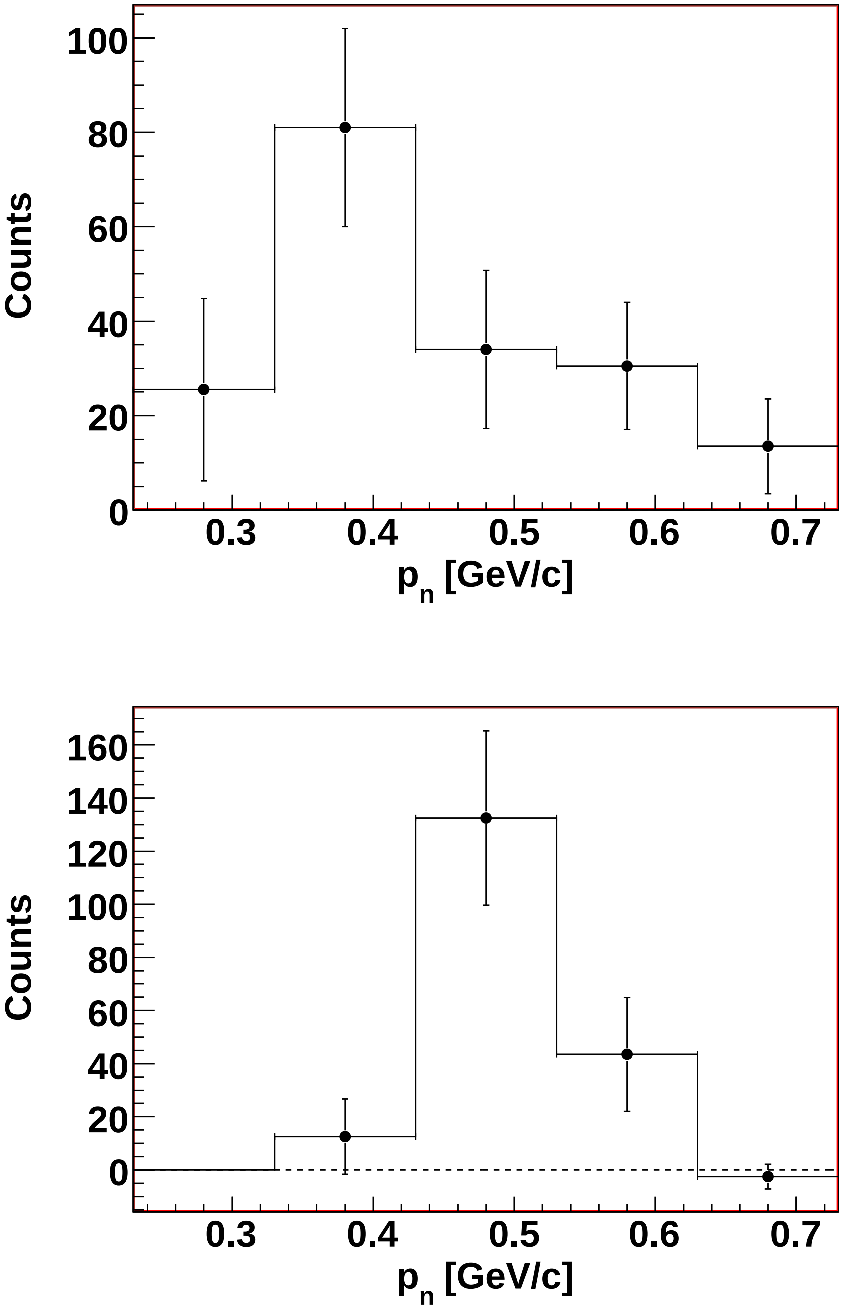

Figure 6-7: Upper plot: Momentum of the recoil partner neutron determined from time-of-flight measurements in the neutron detector. Lower plot: Momentum of recoil partner neutron if assumed to be equal to the missing momentum $\vec{P}_{miss}$. This data is for kinematic III only and figure is courtesy of R. Subedi [10].

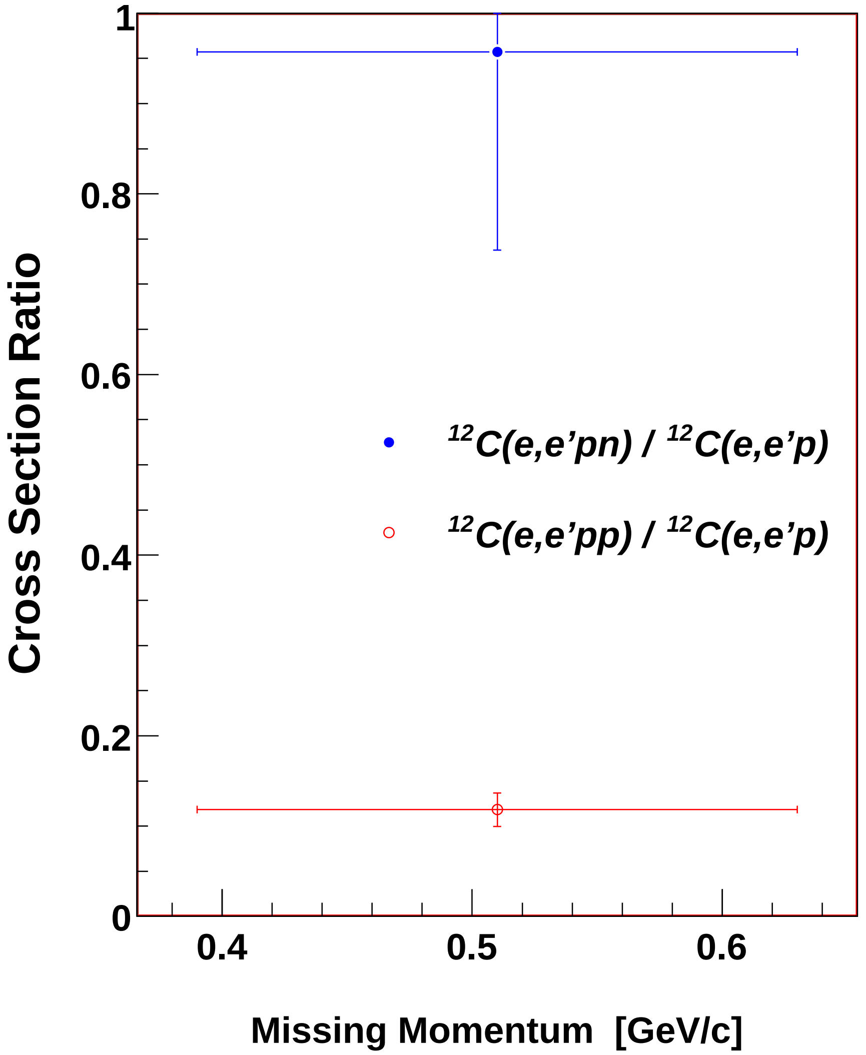

Figure 6-8: The cross-section ratios of $(e, e'pn)/(e, e'p)$ (blue, upper point) and $(e, e'pp)/(e, e'p)$ (red, lower point) corrected for acceptance and extrapolated for all possible partner nucleons available. Together the sum is (within errors) equal to unity, meaning that a recoil partner nucleon is emitted for every $(e, e'p)$ event. This data is for kinematic III only and courtesy of R. Subedi [10].

(A-1) system can be rewritten again as,

$$M^2_{recoil} = \left[\sqrt{(M_{A-2} + \epsilon_x)^2 + p^2_{A-2}} + \sqrt{m^2_N + p^2_{recoil}}\right]^2 - p^2_{miss} \tag{6.6}$$

where ϵ_x is the excitation energy of the (A-2) system. The revised calculation still assumes that the momentum of the partner recoil nucleon is not equal to the missing momentum defined by the $(e, e'p)$ reaction.

The excitation energy of the (A-2) system can be determined using the distribution of missing energy (referred to as E_{2m}) found for the (A-2) system. This is determined through the measurement of the recoil partner nucleon in BigBite (or the neutron detector). The measured E_{2m} distribution is shown in Fig. 6-9, showing the regions corresponding to two nucleon knockout from the p-shell only ($1p^2$) and from the s- and p-shells ($1s1p$). The excitation energy of the (A-2) system is taken relative to the threshold for two nucleon knockout, shown by the $1p^2$ region in Fig. 6-9 which is at $\sim$ 30 MeV. The value used for the calculation was taken as 25 MeV, which is the difference between the peaks in the $1s1p$ and $1p^2$ regions.

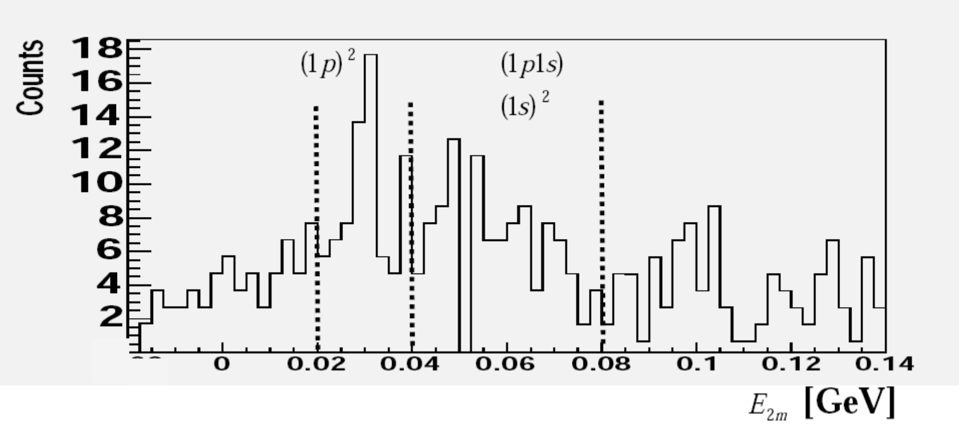

Figure 6-9: The distribution of missing energy of the (A-2) system as measured in BigBite through the $^{12}C(e, e'pp)$ reaction. The two proton knockout begins in the ($1p^2$) regime and continues to higher energy. Therefore, the excitation energy of the (A-2) system is taken relative to this region and for the purposes of a simple calculation is taken as 25 MeV ($1s1p - 1p^2$ regions)This data is for all three kinematics together and courtesy of R. Shneor [11].

The effect of this revised calculation is shown in the cross-section plots in Figs. 6-

10, 6-11 and 6-12, by the dotted (blue online) arrow. It is interesting to note, that for lower missing momentum values, including the excitation energy in the calculation predicts the cross-section peak at a *larger* missing energy than the original model (which kept the (A-2) system at rest in its ground state). However, as the missing momentum increases, this changes and the peak location predicted by including the excitation energy of the (A-2) system moves to a *smaller* missing energy than that predicted by the original model. Thus, as the missing momentum increases, the peak location observed in the data becomes in better agreement with the peak predicted by including the excitation energy of the (A-2) system.

Comparing both revisions of the model to the original, suggests that the data shows some transitions between the regimes where the (A-2) system has very little excitation energy to where it has a large enough excitation energy that it dominates the calculation of the cross-section peak location. Therefore, it seems for lower missing momenta, the peak location is more influenced by the momentum of the recoil partner nucleon, but as the missing momentum increases, so the excitation energy of the (A-2) system becomes increasingly important. It should again be noted that these are only an approximation for illustrative purposes. This is an interesting puzzle, that at the time of writing is still being investigated and could lead to an improved model for the reaction mechanism.

6.3 Extracted Experimental Spectral Function

As discussed in section 5.6.2, the six-fold differential continuum cross-section is given by,

$$\frac{d^6\sigma}{d\Omega_e d\Omega_p dE_e dE_p} = K\ \sigma_{cc2}\ S(\vec{p}_m, E_m) \tag{6.7}$$

Therefore, just as for the bound state case, the experimental spectral function (also referred to as the *reduced cross-section*) can be extracted by dividing the cross-section

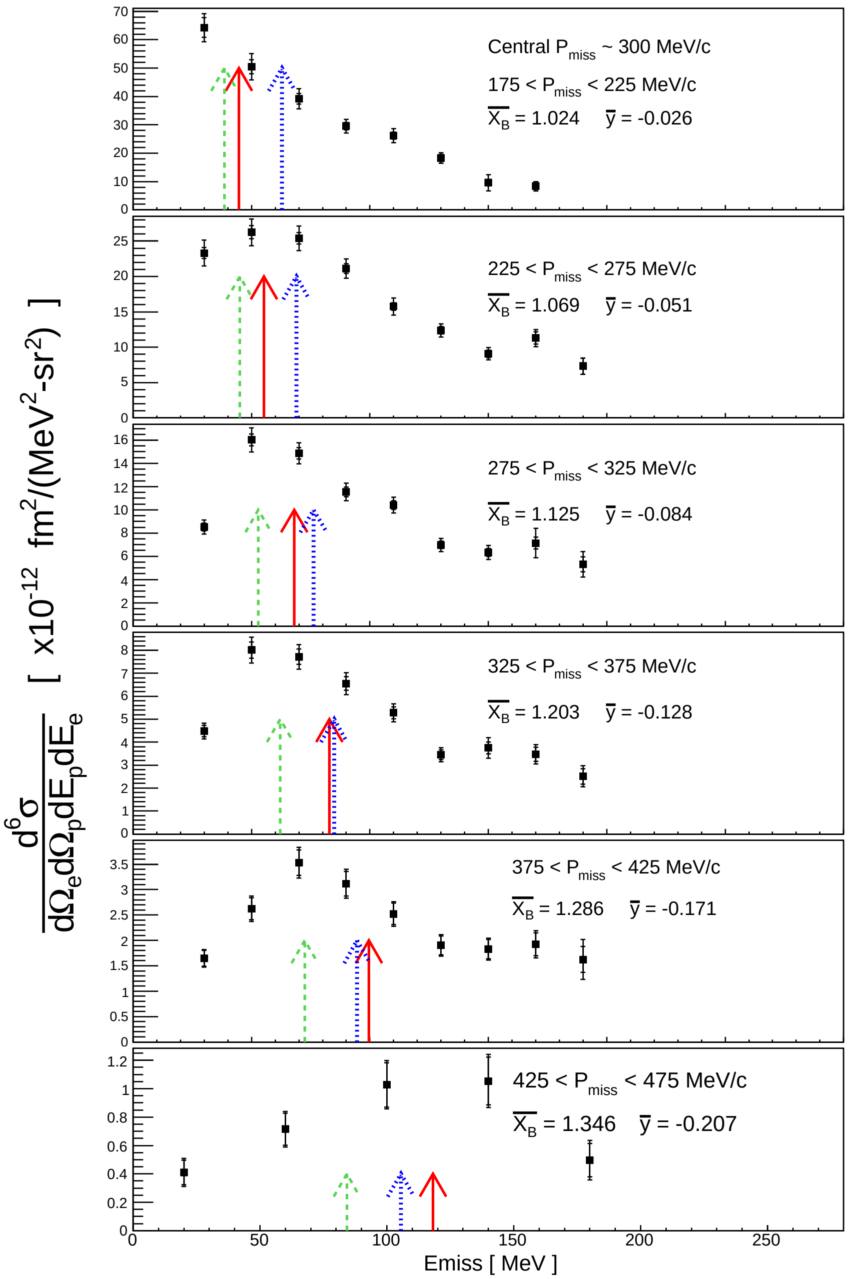

Figure 6-10: Kinematic I extracted cross-section as a function of missing energy for each individual missing momentum bin. The solid (red online) arrow shows the location of the peak in the cross-section based on the recoiling system being a spectator in the reaction; dashed arrow (green online) shows the expected peak location based on a model with the recoiling system having non-zero momentum; the dotted arrow (blue online) shows the expected peak location based on a model which includes the excitation energy of the (A-2) system.

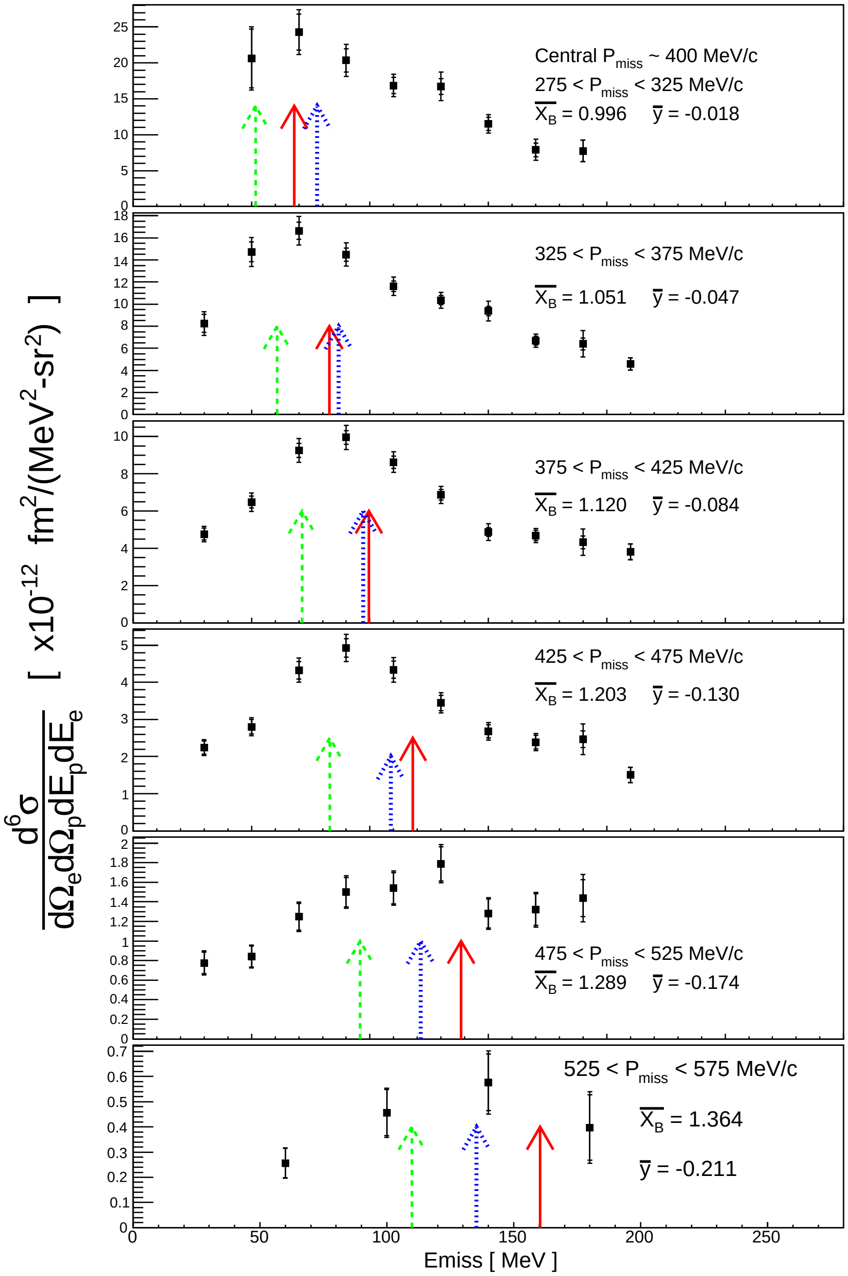

Figure 6-11: Kinematic II extracted cross-section as a function of missing energy for each individual missing momentum bin. The solid (red online) arrow shows the location of the peak in the cross-section based on the recoiling system being a spectator in the reaction; dashed arrow (green online) shows the expected peak location based on a model with the recoiling system having non-zero momentum; the dotted arrow (blue online) shows the expected peak location based on a model which includes the excitation energy of the (A-2) system.

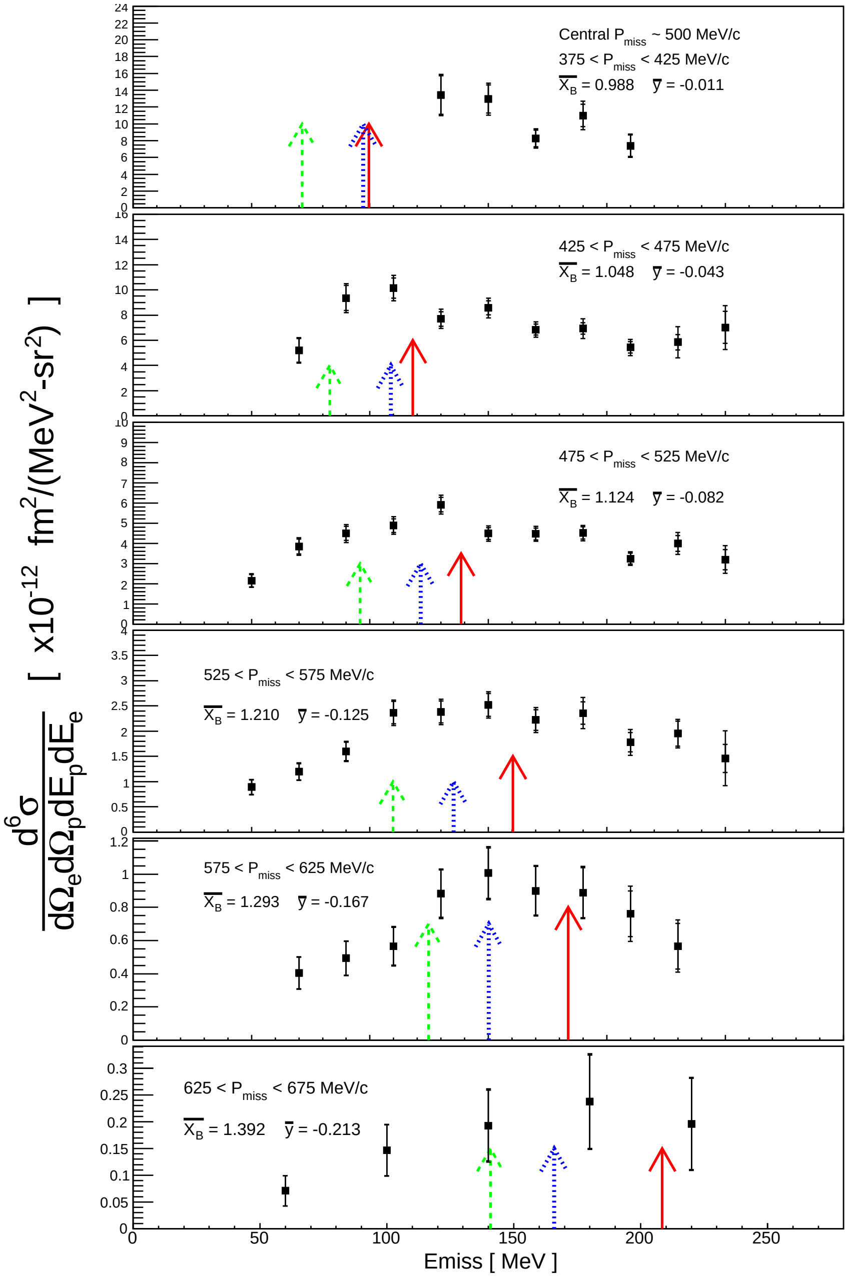

Figure 6-12: Kinematic III extracted cross-section as a function of missing energy for each individual missing momentum bin. The solid (red online) arrow shows the location of the peak in the cross-section based on the recoiling system being a spectator in the reaction; dashed arrow (green online) shows the expected peak location based on a model with the recoiling system having non-zero momentum; the dotted arrow (blue online) shows the expected peak location based on a model which includes the excitation energy of the (A-2) system.

by the single-nucleon offshell cross-section,

$$S(\vec{p}_m, E_m)_{distorted} = \left\langle \frac{d^6\sigma}{d\Omega_e d\Omega_p dE_e dE_p} \right\rangle_{exp} / \left\langle K\sigma_{cc2} \right\rangle_{unit} \tag{6.8}$$

where the acceptance averaged $K\sigma_{cc2}$ cross-section is obtained from a simulation using a unit input spectral function with all other input parameters unchanged from the cross-section extraction simulations. The $K\sigma_{cc2}$ cross-section is obtained for each kinematic setting and the distorted experimental spectral function is then extracted by dividing the extracted cross-sections by this unit cross-section. The experimental spectral functions are shown in Figs. 6-13, 6-14 and 6-15 as a function of missing energy for each missing momentum bin. Also shown in the figures are the same arrows as shown in Figs. 6-10, 6-11 and 6-12, which represent the peak location predicted by three simple models of the (A-1) recoiling system; red arrow is the original model assuming the (A-2) system is a spectator at rest in its ground state; green arrow is the model which uses the momentum of the recoil nucleon not equal to the missing momentum; the blue arrow is for a further refinement of the model by including the excitation energy of the (A-2) system.

In order to calculate the effective momentum density (which will be discussed in Section 6.4) by integrating the spectral function over the missing energy, each plot has been fitted by a function in the peak region with the tail extended to larger missing energy values which is shown by the dashed (red online) curve. In the PWIA, by dividing out the single-nucleon offshell cross-section, $K\sigma_{cc2}$, the resulting spectral function should be a function of only missing energy and missing momentum; all dependence on Q^2 and ω should have been removed. Therefore, the resulting spectral function or reduced cross-section should be consistent in overlapping missing energy and missing momentum bins between the three different kinematic settings. Such a comparison is shown in Fig. 6-16, for those missing momentum bins which are present in more than one kinematic. As can be seen in Fig. 6-16, the reduced cross-section is not consistent between kinematic settings for the same missing momentum bin. This means that the reduced cross-section is not just a function of missing energy and

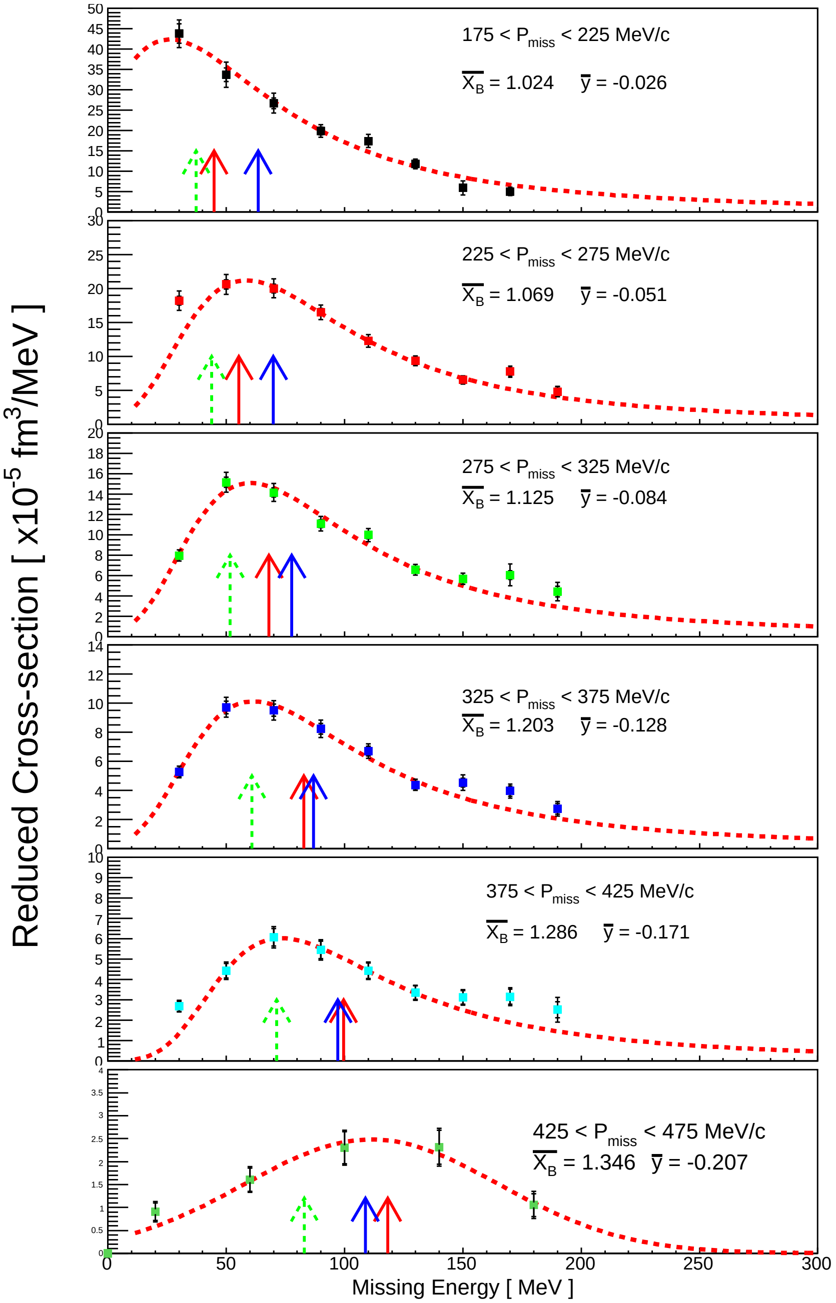

Figure 6-13: The extracted spectral function as a function of missing energy for each missing momentum bin in kinematic I. The average value of Bjorken-X and y scaling variables is also quoted for each plot. The dashed (red online) curve is fitted to the peak location to facilitate calculation of the integral of the spectral function over the missing energy range.

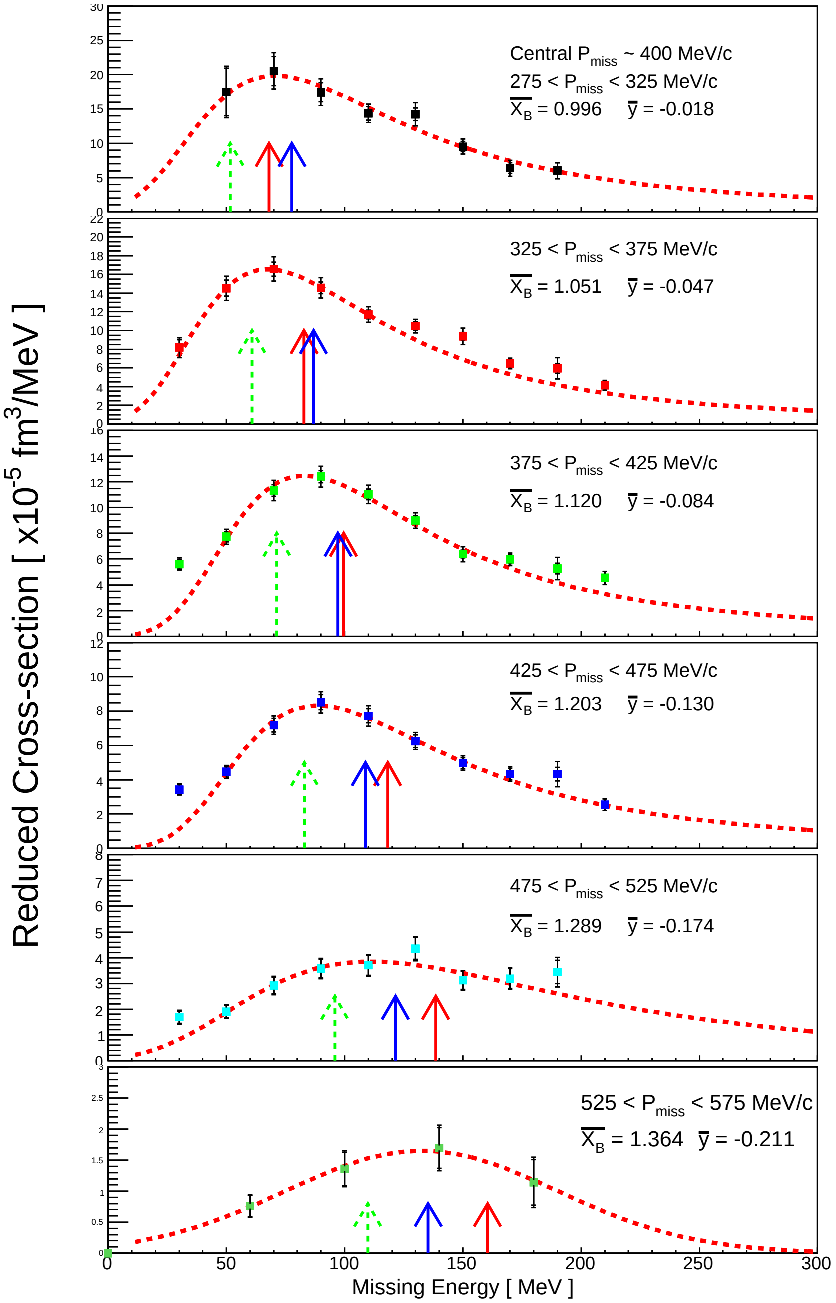

Figure 6-14: The extracted spectral function as a function of missing energy for each missing momentum bin in kinematic II. The average value of Bjorken-X and y scaling variables is also quoted for each plot. The dashed (red online) curve is fitted to the peak location to facilitate calculation of the integral of the spectral function over the missing energy range.

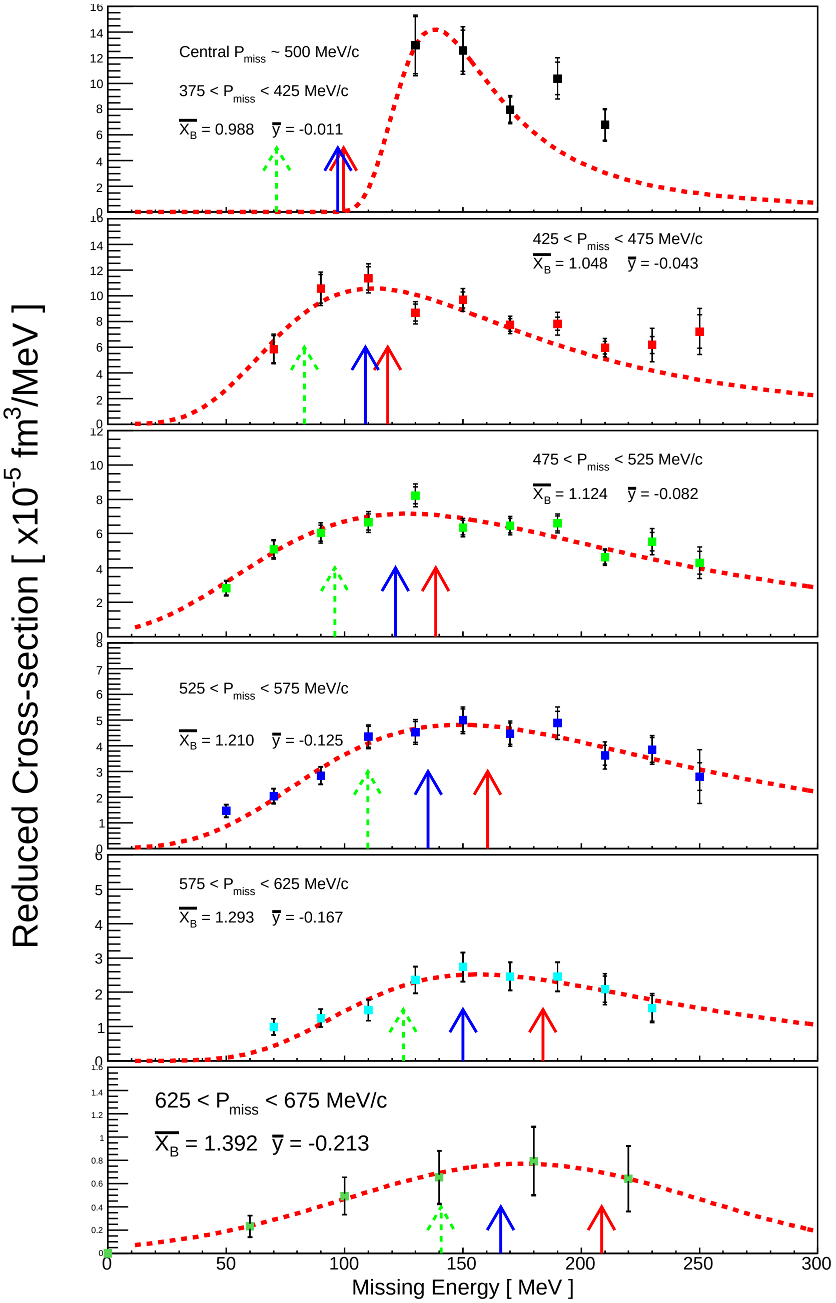

Figure 6-15: The extracted spectral function as a function of missing energy for each missing momentum bin in kinematic III. The average value of Bjorken-X and y scaling variables is also quoted for each plot. The dashed (red online) curve is fitted to the peak location to facilitate calculation of the integral of the spectral function over the missing energy range.

missing momentum and so the PWIA model does not completely describe the data. It is likely that the reduced cross-section is dependent on other kinematic variables, for example, the measured proton momentum. Given the results from the triple coincidence analyses, namely that each $(e, e'p)$ events has a recoil partner nucleon being ejected as well, it is not surprising that the impulse approximation model fails to describe the data. Indeed, even though the kinematics were chosen to try and reduce effects such as final state interactions, the results suggest that these effects are not negligible. Any suitable theoretical calculation to compare with this data ought to have effects such as final state interactions included.

6.4 Effective Momentum Density

The effective momentum density is defined as the integral of the experimental distorted spectral function over missing energy. The resulting integral is a function of missing momentum only and is useful to compare data between different kinematics together and to compare with theoretical calculations. The effective momentum density is given by,

$$\eta(p_{miss}) = \int_{E_{min}}^{E_{max}} S(\vec{p}_m, E_m)_{distorted} dE_{miss} \tag{6.9}$$

where E_{min} and E_{max} are the integral limits. Since the experimental distorted spectral function is given by dividing the extracted cross-section by the single-nucleon offshell cross-section,

$$S(\vec{p}_m, E_m)_{distorted} = \left\langle \frac{d^6\sigma}{d\Omega_e d\Omega_p dE_e dE_p} \right\rangle_{exp} / \left\langle K\sigma_{cc2} \right\rangle_{unit} \tag{6.10}$$

so the effective momentum density can be rewritten as an integral of the cross-section over missing energy,

$$\eta(p_{miss}) = \int_{E_{min}}^{E_{max}} \left\langle \frac{d^6\sigma}{d\Omega_e d\Omega_p dE_e dE_p} \right\rangle_{exp} / \left\langle K\sigma_{cc2} \right\rangle_{unit} dE_{miss} \tag{6.11}$$

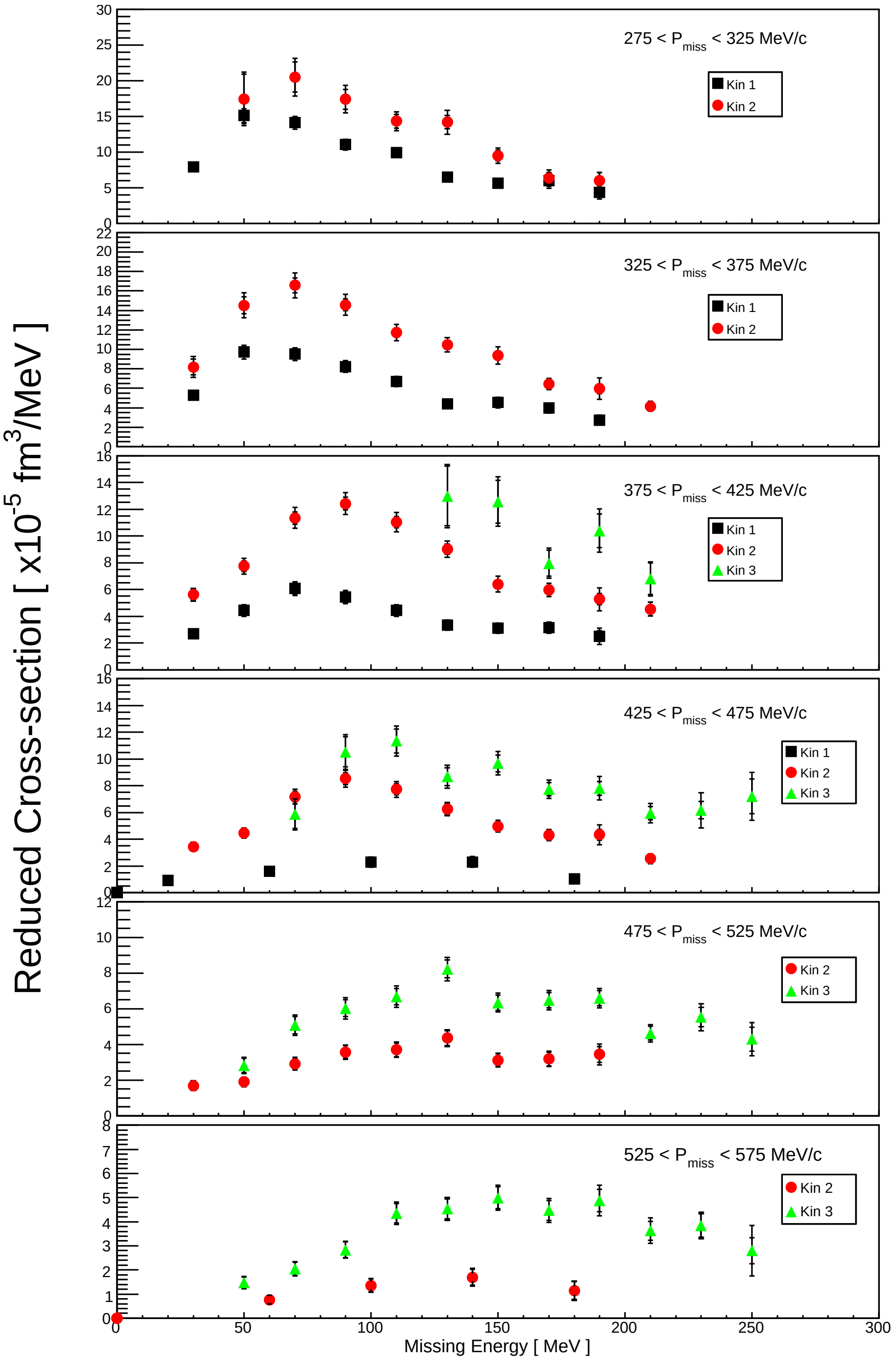

Figure 6-16: Comparison of reduced cross-section (spectral function) for missing momentum bins which overlap between two or more of the kinematic settings. Black squares are kinematic I data; red circles are kinematic II data; green triangles are kinematic III data.

In order to evaluate the integral for the $^{12}C(e,e'p)$ continuum data, a function was fit to each distribution of the extracted distorted spectral function; these are the dashed (red online) curves shown in Figs. 6-13, 6-14 and 6-15. The functions were fitted to the peak location such that their tails continued into the high missing energy regions, without specifically fitting the data at high missing energy. The lower limit of the integral was taken as $E_{min} = 30$ MeV which was the peak in the $1p^2$ regime for two nucleon knockout shown in Fig. 6-9—the missing energy of the (A-2) system. The upper limit of the integral was chosen as $E_{max} = 300$ MeV since for a larger limit, the integrals changed very little. Although the upper integral limit is far above the pion production threshold at 140 MeV, the data extends into the region above 140 MeV and so the function fit was extended into this region as well.

The resulting effective momentum density as a function of missing momentum is shown in Fig. 6-17. The extracted distorted momentum distribution for the $^{12}C(e,e'p)^{11}B$ data is also shown for comparison. The data clearly demonstrates the breakdown of the factorisation cross-section model, since the data from different kinematics for the same missing momentum value varies substancially. The data from the bound states reaction falls rapidly compared with the continuum data, again showing that other effects (such as correlations or final state interactions) are contributing to the cross-section at higher missing momentum values. The total error bars shown on the data arise from the combination of the overall normalisation systematic errors given in Table 5.2 and the error in the integral arising from modifying the fitted functions by their fitted parameter errors and re-evaluating the fit and integral.

6.5 Quasielastic Cross-section Comparison

The cross-section for the $^{12}C(e,e'p)$ continuum data at the quasielastic peak was extracted by using a cut on the Bjorken-X scaling variable of $x_B = 1 \pm 1\%$. This resulted in a smaller dataset for each kinematic, covering only a limited range of missing momenta. The resulting extracted cross-sections are shown in Fig. 6-18 as a function of missing energy and demonstate a linear decrease in cross-section with

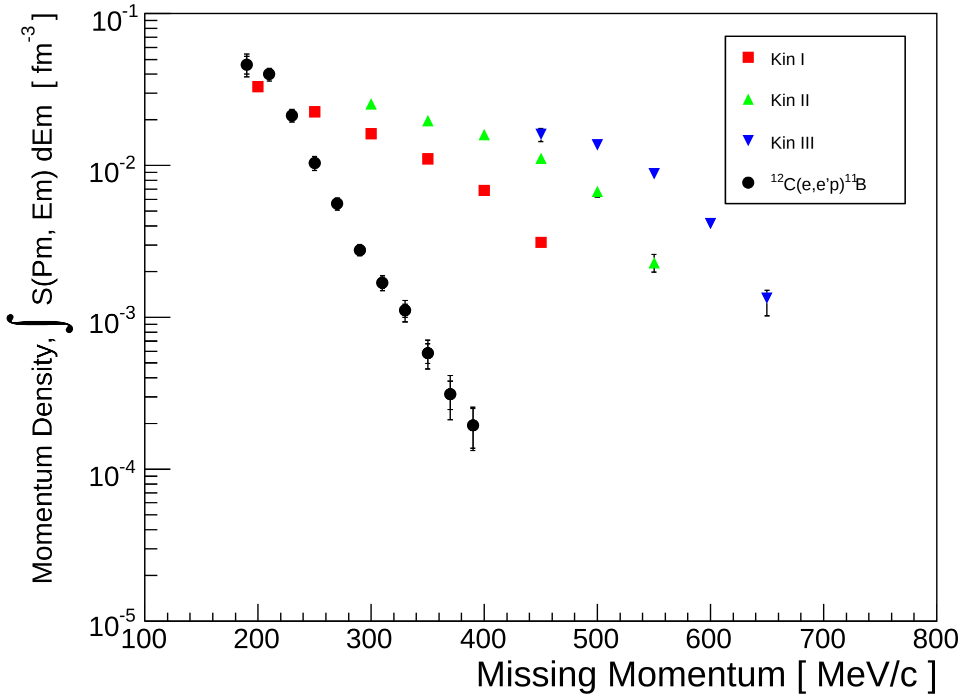

Figure 6-17: Comparison of the effective momentum density for each dataset from the continuum reaction (integrated reduced cross-section) as a function of missing momentum. The black squares are data the reduced cross-section for the $^{12}C(e,e'p)^{11}B$ reaction. The fact that the continuum datasets do not overlap for the same missing momenta values is another indication of the breakdown of the factorisation model of the cross-section and that other effects contribute significantly to the cross-section.

increasing missing energy. A further comparison of the quasielastic cross-sections with the full (not cut at $x_B = 1 \pm 1\%$) extracted cross-sections is shown in Fig. 6-19. It appears that the quasielastic cross-sections contribute to the tails of the full cross-sections at higher missing energy values and do not contribute to the peak regions.

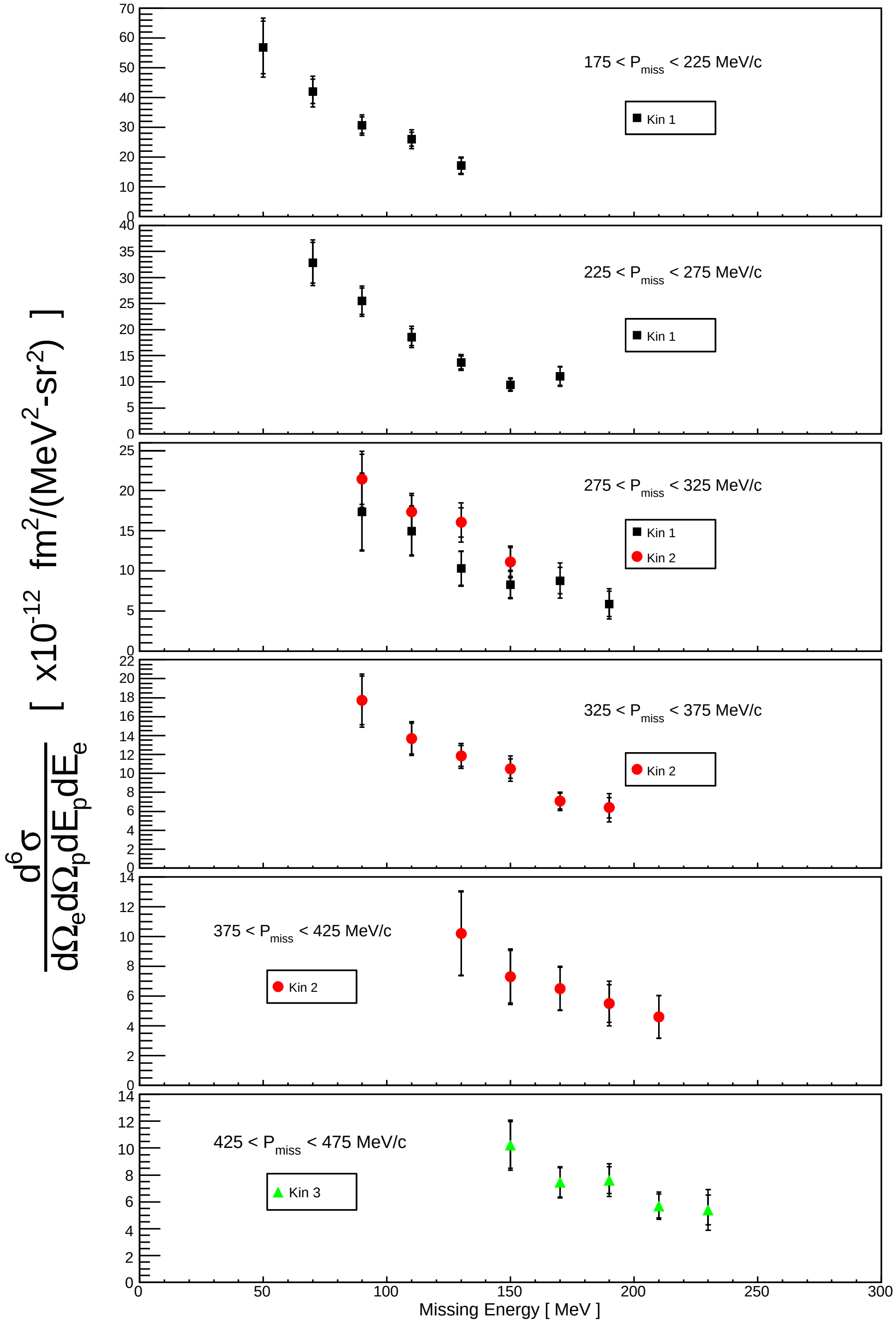

Figure 6-18: The extracted quasielastic cross-section as a function of missing energy for different missing momenta. A cut of $x_B = 1 \pm 1\%$ was used to extract these cross-sections and thus only a limited range of missing momentum is covered in each kinematic.

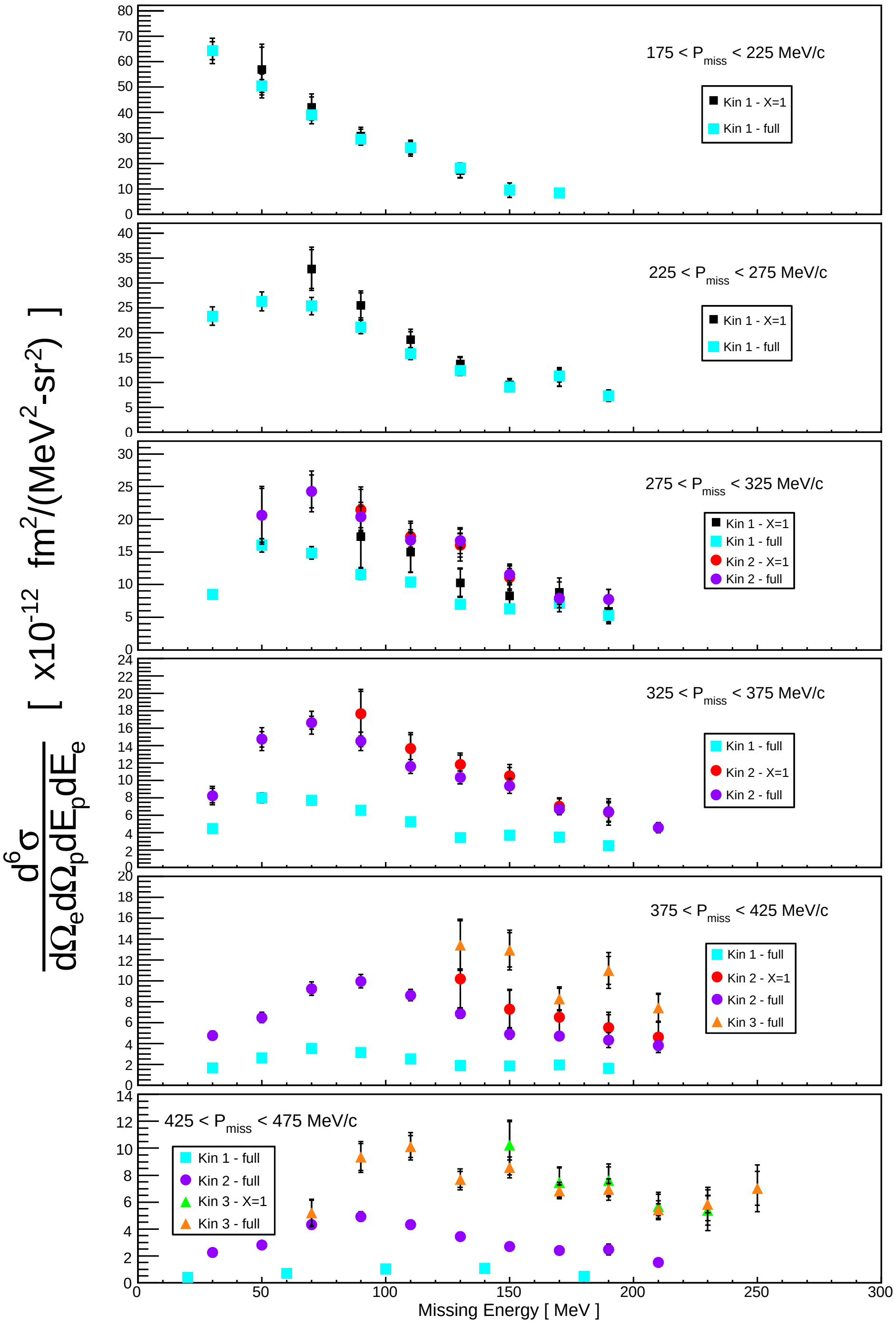

Figure 6-19: A comparison of the quasielastic cross-section extracted using $x_B = 1 \pm 1\%$ and the continuum cross-sections extracted without using this constraint on Bjorken-X. For the same missing momentum bin, the *full* cross-section (not using the x_B cut) has a tail arising from the data at $x_B = 1$.

6.6 Tabulated Results

The following tables of results present the extracted cross-sections, momentum distributions and spectral functions for all of the data analysed in this thesis. The statistical and systematic errors for each data point are quoted separately; systematic errors are discussed in section 5.8. Note, the statistical and systematic error values for the extracted spectral functions are the same as those for the cross-sections and thus are not quoted. The errors quoted for values of Q^2, ω and y bins are simply the standard deviations of the distributions for that particular missing momentum bin.

6.6.1 Kinematic I Results

E_{miss} $[MeV]$	$\frac{d^6\sigma}{d\Omega_e d\Omega_p dE_p dE_e} \pm \delta_{stat} \pm \delta_{sys}$ $[fm^2/(MeV^2 - sr^2)]$	$S_{exp}(E_m, P_m)$ $[fm^3/MeV]$	Kinematic Bin
30	6.4265e-11 ± 5.4% ± 5.6%	4.380e-4	$\bar{Q}^2 = 1.714 \pm 0.047\ (GeV/c)^2$ $\bar{\omega} = 900.7 \pm 27.4\ MeV$ $\bar{y} = -0.026 \pm 0.021$
50	5.047e-11 ± 5.0% ± 7.7%	3.376e-4	
70	3.9167e-11 ± 4.8% ± 7.8%	2.673e-4	
90	2.9543e-11 ± 4.6% ± 6.6%	1.993e-4	
110	2.6219e-11 ± 4.8% ± 8.1%	1.747e-4	
130	1.8323e-11 ± 6.6% ± 7.4%	1.182e-4	
150	9.6060e-12 ± 11.6% ± 27.2%	5.965e-5	
170	8.3893e-12 ± 19.4% ± >27.2%	5.078e-5	

Table 6.2: Results for kinematic I: $P_{miss} = 200 \pm 25$ MeV/c

E_{miss} $[MeV]$	$\frac{d^6\sigma}{d\Omega_e d\Omega_p dE_p dE_e} \pm \delta_{stat} \pm \delta_{sys}$ $[fm^2/(MeV^2 - sr^2)]$	$S_{exp}(E_m, P_m)$ $[fm^3/MeV]$	Kinematic Bin
30	2.3310e-11 ± 3.4% ± 7.2%	1.8225e-4	
50	2.6262e-11 ± 3.4% ± 6.3%	2.0607e-4	$\bar{Q}^2 = 1.77 \pm 0.076\ (GeV/c)^2$
70	2.5383e-11 ± 3.2% ± 6.1%	2.0014e-4	
90	2.1141e-11 ± 3.2% ± 5.6%	1.6515e-4	$\bar{\omega} = 888.0 \pm 33.8\ MeV$
110	1.5755e-11 ± 3.5% ± 6.8%	1.2284e-4	
130	1.2379e-11 ± 4.3% ± 6.3%	9.3276e-5	$\bar{y}$ = -0.051 ± 0.028
150	9.0756e-12 ± 5.9% ± 7.4%	6.5457e-5	
170	1.1307e-11 ± 7.8% ± 7.3%	7.7591e-5	
190	7.3169e-12 ± 15.6% ± >7.3%	4.8119e-5	

Table 6.3: Results for kinematic I: P_{miss} = 250 ± 25 MeV/c

E_{miss} $[MeV]$	$\frac{d^6\sigma}{d\Omega_e d\Omega_p dE_p dE_e} \pm \delta_{stat} \pm \delta_{sys}$ $[fm^2/(MeV^2 - sr^2)]$	$S_{exp}(E_m, P_m)$ $[fm^3/MeV]$	Kinematic Bin
30	8.5243e-12 ± 4.1% ± 5.7%	7.9412e-5	
50	1.6022e-11 ± 3.3% ± 5.6%	1.5143e-4	$\bar{Q}^2 = 1.855 \pm 0.106\ (GeV/c)^2$
70	1.4861e-11 ± 3.3% ± 5.3%	1.414e-4	
90	1.1546e-11 ± 3.5% ± 5.6%	1.1073e-4	$\bar{\omega} = 878.3 \pm 40.3\ MeV$
110	1.0403e-11 ± 3.7% ± 5.3%	9.9625e-5	
130	6.9863e-12 ± 4.6% ± 6.7%	6.5383e-5	$\bar{y}$ = -0.084 ± 0.033
150	6.3215e-12 ± 5.6% ± 7.8%	5.6682e-5	
170	7.134e-12 ± 7.0% ± 16.4%	6.0441e-5	
190	5.3084e-12 ± 11.8% ± 17.0%	4.3936e-5	

Table 6.4: Results for kinematic I: P_{miss} = 300 ± 25 MeV/c

E_{miss} $[MeV]$	$\frac{d^6\sigma}{d\Omega_e d\Omega_p dE_p dE_e} \pm \delta_{stat} \pm \delta_{sys}$ $[fm^2/(MeV^2 - sr^2)]$	$S_{exp}(E_m, P_m)$ $[fm^3/MeV]$	Kinematic Bin
30	4.4847e-12 ± 5.4% ± 5.5%	5.2641e-5	
50	8.0153e-12 ± 4.5% ± 5.5%	9.7179e-5	$\bar{Q}^2 = 1.993 \pm 0.130\ (GeV/c)^2$
70	7.7198e-12 ± 4.4% ± 5.5%	9.5143e-5	
90	6.5549e-12 ± 4.6% ± 5.7%	8.2357e-5	$\bar{\omega} = 875.9 \pm 44.4\ MeV$
110	5.2778e-12 ± 5.1% ± 5.6%	6.7068e-5	
130	3.4438e-12 ± 6.1% ± 6.5%	4.3845e-5	$\bar{y}$ = -0.128 ± 0.037
150	3.7497e-12 ± 6.8% ± 9.8%	4.5442e-5	
170	3.4710e-12 ± 8.6% ± 8.7%	3.9622e-5	
190	2.5112e-12 ± 13.5% ± 12.0%	2.7476e-5	

Table 6.5: Results for kinematic I: P_{miss} = 350 ± 25 MeV/c

E_{miss} $[MeV]$	$\frac{d^6\sigma}{d\Omega_e d\Omega_p dE_p dE_e} \pm \delta_{stat} \pm \delta_{sys}$ $[fm^2/(MeV^2 - sr^2)]$	$S_{exp}(E_m, P_m)$ $[fm^3/MeV]$	Kinematic Bin
30	1.6486e-12 ± 9.4% ± 5.0%	2.6839e-5	
50	2.6269e-12 ± 8.3% ± 4.9%	4.4269e-5	$\bar{Q}^2 = 2.144 \pm 0.112$
70	3.5321e-12 ± 7.2% ± 4.9%	6.0628e-5	
90	3.1174e-12 ± 7.7% ± 4.8%	5.4493e-5	$\bar{\omega} = 880.0 \pm 46.0$
110	2.5209e-12 ± 8.4% ± 4.8%	4.4248e-5	
130	1.9037e-12 ± 9.8% ± 5.3%	3.3456e-5	$\bar{y} =$ -0.171 $\pm$ 0.036
150	1.8283e-12 ± 10.5% ± 5.9%	3.1177e-5	
170	1.9244e-12 ± 11.7% ± 7.3%	3.1457e-5	
190	1.6238e-12 ± 15.8% ± 18.4%	2.5142e-5	

Table 6.6: Results for kinematic I: $P_{miss} = 400 \pm 25$ MeV/c

E_{miss} $[MeV]$	$\frac{d^6\sigma}{d\Omega_e d\Omega_p dE_p dE_e} \pm \delta_{stat} \pm \delta_{sys}$ $[fm^2/(MeV^2 - sr^2)]$	$S_{exp}(E_m, P_m)$ $[fm^3/MeV]$	Kinematic Bin
20	4.0965e-13 ± 21.2% ± 12.0%	9.087e-6	
60	7.1458e-13 ± 15.8% ± 7.3%	1.6063e-5	$\bar{Q}^2 = 2.253 \pm 0.075$
100	1.0275e-12 ± 15.2% ± 6.5%	2.3029e-5	$\bar{\omega} = 875.0 \pm 44.1$
140	1.0535e-12 ± 16.0% ± 7.6%	2.3123e-5	$\bar{y} =$ -0.207 $\pm$ 0.035
180	4.9575e-13 ± 23.6% ± 15.1%	1.0525e-5	

Table 6.7: Results for kinematic I: $P_{miss} = 450 \pm 25$MeV/c

6.6.2 Kinematic II Results

E_{miss} $[MeV]$	$\frac{d^6\sigma}{d\Omega_e d\Omega_p dE_p dE_e} \pm \delta_{stat} \pm \delta_{sys}$ $[fm^2/(MeV^2 - sr^2)]$	$S_{exp}(E_m, P_m)$ $[fm^3/MeV]$	Kinematic Bin
50	2.0623e-11 ± 19.9% ± 7.7%	1.749e-4	
70	2.4281e-11 ± 10.3% ± 7.8%	2.0539e-4	$\bar{Q}^2 = 1.706 \pm 0.043\ (GeV/c)^2$
90	2.0353e-11 ± 7.9% ± 7.6%	1.7447e-4	
110	1.6841e-11 ± 6.7% ± 6.3%	1.4367e-4	$\bar{\omega} = 909.3 \pm 25.2\ MeV$
130	1.6719e-11 ± 6.5% ± 9.9%	1.4223e-4	
150	1.1524e-11 ± 7.8% ± 8.0%	9.5344e-5	$\bar{y} = -0.018 \pm 0.019\ MeV$
170	7.9021e-12 ± 12.0% ± 13.9%	6.3816e-5	
190	7.7418e-12 ± 19.5% ± >13.9%	6.0037e-5	

Table 6.8: Results for kinematic II: $P_{miss} = 300 \pm 25$ MeV/c

E_{miss} $[MeV]$	$\frac{d^6\sigma}{d\Omega_e d\Omega_p dE_p dE_e} \pm \delta_{stat} \pm \delta_{sys}$ $[fm^2/(MeV^2 - sr^2)]$	$S_{exp}(E_m, P_m)$ $[fm^3/MeV]$	Kinematic Bin
30	8.2590e-12 ± 9.9% ± 8.4%	8.1855e-5	
50	1.4734e-11 ± 6.0% ± 6.6%	1.4532e-4	$\bar{Q}^2 = 1.762 \pm 0.070\ (GeV/c)^2$
70	1.6642e-11 ± 4.5% ± 6.3%	1.6582e-4	
90	1.4496e-11 ± 4.1% ± 6.1%	1.4563e-4	$\bar{\omega} = 889.6 \pm 35.4\ MeV$
110	1.1617e-11 ± 4.1% ± 5.7%	1.1724e-4	
130	1.0349e-11 ± 4.0% ± 5.7%	1.0489e-4	$\bar{y} = -0.048 \pm 0.027$
150	9.3786e-12 ± 4.5% ± 8.2%	9.3814e-5	
170	6.6885e-12 ± 6.0% ± 6.5%	6.466e-5	
190	6.4109e-12 ± 8.4% ± 16.7%	5.963e-5	
210	4.5852e-12 ± 12.2% ± >16.7%	4.1476e-5	

Table 6.9: Results for kinematic II: $P_{miss} = 350 \pm 25$ MeV/c

E_{miss} $[MeV]$	$\frac{d^6\sigma}{d\Omega_e d\Omega_p dE_p dE_e} \pm \delta_{stat} \pm \delta_{sys}$ $[fm^2/(MeV^2 - sr^2)]$	$S_{exp}(E_m, P_m)$ $[fm^3/MeV]$	Kinematic Bin
30	4.7619e-12 ± 6.6% ± 5.3%	5.6078e-5	
50	6.4788e-12 ± 5.0% ± 5.8%	7.7369e-5	$\bar{Q}^2 = 1.850 \pm 0.102$
70	9.2484e-12 ± 4.0% ± 5.6%	1.1341e-4	
90	9.953e-12 ± 3.7% ± 5.3%	1.2417e-4	$\bar{\omega} = 875.1 \pm 42.2$
110	8.6258e-12 ± 3.8% ± 5.3%	1.1021e-4	
130	6.8648e-12 ± 4.1% ± 5.3%	9.0097e-5	$\bar{y} = \text{-}0.084 \pm 0.031$
150	4.8747e-12 ± 4.8% ± 7.9%	6.3875e-5	
170	4.6851e-12 ± 5.8% ± 5.8%	5.9760e-5	
190	4.3172e-12 ± 7.8% ± 14.4%	5.2723e-5	
210	3.8091e-12 ± 11.2% ± >14.4%	4.5356e-5	

Table 6.10: Results for kinematic II: $P_{miss} = 400 \pm 25$ MeV/c

E_{miss} $[MeV]$	$\frac{d^6\sigma}{d\Omega_e d\Omega_p dE_p dE_e} \pm \delta_{stat} \pm \delta_{sys}$ $[fm^2/(MeV^2 - sr^2)]$	$S_{exp}(E_m, P_m)$ $[fm^3/MeV]$	Kinematic Bin
30	2.2453e-12 ± 7.8% ± 5.3%	3.4378e-5	
50	2.8028e-12 ± 6.8% ± 5.3%	4.4599e-5	$\bar{Q}^2 = 1.990 \pm 0.127\ (GeV/c)^2$
70	4.3283e-12 ± 5.5% ± 5.1%	7.1842e-5	
90	4.9272e-12 ± 5.1% ± 5.2%	8.524e-5	$\bar{\omega} = 871.6 \pm 47.8\ MeV$
110	4.337e-12 ± 5.3% ± 5.4%	7.7292e-5	
130	3.4451e-12 ± 5.9% ± 5.2%	6.2574e-5	$\bar{y} = \text{-}0.130 \pm 0.034$
150	2.6791e-12 ± 6.5% ± 5.7%	4.9777e-5	
170	2.3872e-12 ± 7.7% ± 5.9%	4.3285e-5	
190	2.4691e-12 ± 9.2% ± 14.2%	4.3377e-5	
210	1.5048e-12 ± 13.6% ± >14.2%	2.5451e-5	

Table 6.11: Results for kinematic II: $P_{miss} = 450 \pm 25$ MeV/c

E_{miss} $[MeV]$	$\frac{d^6\sigma}{d\Omega_e d\Omega_p dE_p dE_e} \pm \delta_{stat} \pm \delta_{sys}$ $[fm^2/(MeV^2 - sr^2)]$	$S_{exp}(E_m, P_m)$ $[fm^3/MeV]$	Kinematic Bin
30	7.7548e-13 ± 14.2% ± 7.2%	1.686e-5	
50	8.4012e-13 ± 12.8% ± 5.2%	1.8976e-5	$\bar{Q}^2 = 2.148 \pm 0.110\ (GeV/c)^2$
70	1.2475e-12 ± 11.1% ± 4.9%	2.9131e-5	
90	1.4990e-12 ± 10.0% ± 4.8%	3.5699e-5	$\bar{\omega} = 877.8 \pm 49.6\ MeV$
110	1.5397e-12 ± 10.3% ± 4.8%	3.7028e-5	
130	1.7886e-12 ± 9.8% ± 4.8%	4.3519e-5	$\bar{y}$ = -0.174 ± 0.033
150	1.2812e-12 ± 11.5% ± 5.0%	3.1158e-5	
170	1.3208e-12 ± 12.3% ± 5.5%	3.1875e-5	
190	1.4388e-12 ± 13.1% ± 10.5%	3.4383e-5	

Table 6.12: Results for kinematic II: $P_{miss} = 500 \pm 25$ MeV/c

E_{miss} $[MeV]$	$\frac{d^6\sigma}{d\Omega_e d\Omega_p dE_p dE_e} \pm \delta_{stat} \pm \delta_{sys}$ $[fm^2/(MeV^2 - sr^2)]$	$S_{exp}(E_m, P_m)$ $[fm^3/MeV]$	Kinematic Bin
60	2.5632e-13 ± 22.9% ± 5.5%	7.5959e-6	
100	4.5677e-13 ± 19.9% ± 7.8%	1.3601e-5	$\bar{Q}^2 = 2.258 \pm 0.074$
140	5.7681e-13 ± 19.5% ± 9.6%	1.6986e-5	$\bar{\omega} = 867.3 \pm 44.9$
180	3.9764e-13 ± 32.4% ± 15.2%	1.140e-5	$\bar{y}$ = -0.214 ± 0.033

Table 6.13: Results for kinematic II: $P_{miss} = 550 \pm 25$ MeV/c

6.6.3 Kinematic III Results

E_{miss} $[MeV]$	$\frac{d^6\sigma}{d\Omega_e d\Omega_p dE_p dE_e} \pm \delta_{stat} \pm \delta_{sys}$ $[fm^2/(MeV^2 - sr^2)]$	$S_{exp}(E_m, P_m)$ $[fm^3/MeV]$	Kinematic Bin
130	1.3437e-11 ± 17.2% ± 5.9%	1.2975e-4	
150	1.2958e-11 ± 12.8% ± 7.4%	1.2558e-4	$\bar{Q}^2 = 1.694 \pm 0.037\ (GeV/c)^2$
170	8.2608e-12 ± 12.2% ± 6.5%	7.9643e-5	$\bar{\omega} = 914.6 \pm 22.9\ MeV$
190	1.1005e-11 ± 12.0% ± 9.8%	1.0398e-4	$\bar{y} = -0.011 \pm 0.018$
210	7.4011e-12 ± 17.4% ± 6.5%	6.7886e-5	

Table 6.14: Results for kinematic III: $P_{miss} = 400 \pm 25$ MeV/c

E_{miss} $[MeV]$	$\frac{d^6\sigma}{d\Omega_e d\Omega_p dE_p dE_e} \pm \delta_{stat} \pm \delta_{sys}$ $[fm^2/(MeV^2 - sr^2)]$	$S_{exp}(E_m, P_m)$ $[fm^3/MeV]$	Kinematic Bin
70	5.1976e-12 ± 18.0% ± 7.7%	5.8555e-5	
90	9.3533e-12 ± 10.7% ± 6.0%	1.0536e-4	$\bar{Q}^2 = 1.748 \pm 0.062\ (GeV/c)^2$
110	1.0138e-11 ± 8.0% ± 6.0%	1.1341e-4	
130	7.6900e-12 ± 7.6% ± 6.5%	8.6762e-5	$\bar{\omega} = 891.0 \pm 37.2\ MeV$
150	8.5592e-12 ± 6.5% ± 6.4%	9.6726e-5	
170	6.8514e-12 ± 6.4% ± 6.1%	7.7332e-5	$\bar{y} = -0.042 \pm 0.027$
190	6.9346e-12 ± 6.6% ± 9.2%	7.8125e-5	
210	5.4295e-12 ± 8.3% ± 8.7%	5.9481e-5	
230	5.8479e-12 ± 10.6% ± 18.5%	6.1674e-5	
250	7.0210e-12 ± 18.0% ± 16.9%	7.2157e-5	

Table 6.15: Results for kinematic III: $P_{miss} = 450 \pm 25$ MeV/c

E_{miss} $[MeV]$	$\frac{d^6\sigma}{d\Omega_e d\Omega_p dE_p dE_e} \pm \delta_{stat} \pm \delta_{sys}$ $[fm^2/(MeV^2 - sr^2)]$	$S_{exp}(E_m, P_m)$ $[fm^3/MeV]$	Kinematic Bin
50	2.1516e-12 ± 14.2% ± 7.2%	2.8216e-5	
70	3.8327e-12 ± 9.7% ± 5.8%	5.0807e-5	$\bar{Q}^2 = 1.833 \pm 0.091\ (GeV/c)^2$
90	4.4882e-12 ± 7.8% ± 6.3%	6.0347e-5	
110	4.8761e-12 ± 6.9% ± 5.8%	6.6726e-5	$\bar{\omega} = 870.5 \pm 47.8\ MeV$
130	5.9135e-12 ± 6.1% ± 5.2%	8.2249e-5	
150	4.4850e-12 ± 6.7% ± 5.2%	6.3453e-5	$\bar{y} = -0.082 \pm 0.032$
170	4.4639e-12 ± 6.5% ± 5.2%	6.4740e-5	
190	4.5090e-12 ± 6.6% ± 5.2%	6.5933e-5	
210	3.2338e-12 ± 8.3% ± 6.2%	4.6276e-5	
230	3.9910e-12 ± 9.8% ± 9.7%	5.5293e-5	
250	3.1928e-12 ± 15.6% ± 14.7%	4.2965e-5	

Table 6.16: Results for kinematic III: $P_{miss} = 500 \pm 25$ MeV/c

E_{miss} $[MeV]$	$\frac{d^6\sigma}{d\Omega_e d\Omega_p dE_p dE_e} \pm \delta_{stat} \pm \delta_{sys}$ $[fm^2/(MeV^2 - sr^2)]$	$S_{exp}(E_m, P_m)$ $[fm^3/MeV]$	Kinematic Bin
50	8.9102e-13 ± 16.2% ± 5.7%	1.470e-5	
70	1.1931e-12 ± 13.3% ± 5.8%	2.0447e-5	$\bar{Q}^2 = 1.973 \pm 0.118\ (GeV/c)^2$
90	1.5997e-12 ± 11.4% ± 5.0%	2.8386e-5	
110	2.3633e-12 ± 9.3% ± 5.1%	4.3507e-5	$\bar{\omega} = 870.3 \pm 54.5\ MeV$
130	2.3782e-12 ± 9.1% ± 5.4%	4.5358e-5	
150	2.5215e-12 ± 8.9% ± 5.4%	4.9946e-5	$\bar{y} = -0.125 \pm 0.033$
170	2.2207e-12 ± 9.2% ± 6.2%	4.4738e-5	
190	2.3571e-12 ± 9.4% ± 8.9%	4.8766e-5	
210	1.7775e-12 ± 10.8% ± 9.7%	3.6305e-5	
230	1.9500e-12 ± 12.5% ± 7.1%	3.8419e-5	
250	1.4611e-12 ± 19.1% ± 32.0%	2.8005e-5	

Table 6.17: Results for kinematic III: $P_{miss} = 550 \pm 25$ MeV/c

E_{miss} $[MeV]$	$\frac{d^6\sigma}{d\Omega_e d\Omega_p dE_p dE_e} \pm \delta_{stat} \pm \delta_{sys}$ $[fm^2/(MeV^2 - sr^2)]$	$S_{exp}(E_m, P_m)$ $[fm^3/MeV]$	Kinematic Bin
70	4.0401e-13 ± 23.6% ± 5.0%	9.8833e-6	$\bar{Q}^2 = 2.139 \pm 0.104\ (GeV/c)^2$ $\bar{\omega} = 883.7 \pm 56.8\ MeV$ $\bar{y}$ = -0.167 ± 0.035
90	4.9304e-13 ± 20.7% ± 5.0%	1.2481e-5	
110	5.6565e-13 ± 20.3% ± 5.0%	1.4768e-5	
130	8.8261e-13 ± 16.2% ± 4.9%	2.3564e-5	
150	1.0067e-12 ± 15.2% ± 4.9%	2.7334e-5	
170	9.0039e-13 ± 16.2% ± 5.2%	2.4628e-5	
190	8.8911e-13 ± 16.9% ± 5.3%	2.4533e-5	
210	7.6068e-13 ± 18.0% ± 12.4%	2.0877e-5	
230	5.6667e-13 ± 24.3% ± 13.3%	1.5327e-5	

Table 6.18: Results for kinematic III: P_{miss} = 600 ± 25 MeV/c

E_{miss} $[MeV]$	$\frac{d^6\sigma}{d\Omega_e d\Omega_p dE_p dE_e} \pm \delta_{stat} \pm \delta_{sys}$ $[fm^2/(MeV^2 - sr^2)]$	$S_{exp}(E_m, P_m)$ $[fm^3/MeV]$	Kinematic Bin
60	7.0943e-14 ± 39.7% ± 6.6%	2.3169e-6	$\bar{Q}^2 = 2.249 \pm 0.075\ (GeV/c)^2$ $\bar{\omega} = 864.1 \pm 58.5\ MeV$ $\bar{y}$ = -0.213 ± 0.040
100	1.4667e-13 ± 32.4% ± 5.2%	4.9356e-6	
140	1.9285e-13 ± 34.3% ± 8.7%	6.5380e-6	
180	2.3735e-13 ± 36.7% ± 8.4%	7.9443e-6	
220	1.9601e-13 ± 43.4% ± 9.1%	6.4129e-6	

Table 6.19: Results for kinematic III: P_{miss} = 650 ± 25 MeV/c

Chapter 7

Summary and Conclusions

This experiment was motivated by a desire to study short-range nucleon-nucleon correlations through multinucleon knockout reactions, in a kinematic regime where these effects are expected to be significant—namely a large momentum transfer and $x_B > 1$. A triple coincidence (e, e', pN) measurement was made on carbon, using the two high resolution spectrometers in Hall A at JLab along with a third, large acceptance spectrometer, called *BigBite*. The double coincidence (e, e', p) reaction underpins all of the multinucleon knockout data. This provided data on the $^{12}C(e, e', p)$ reaction in previously unexplored kinematics which complement earlier data from experiments on ^{3}He [3] and ^{12}C [27]. This was also the first experiment to use the BigBite spectrometer and resulted in the construction of detectors and equipment that have been used in subsequent experiments in Hall A.

Data were taken at fixed electron kinematics, using a four-momentum transfer $Q^2 = 2$ (GeV/c)^2, with $x_B \approx 1.2$; the acceptances of the spectrometers meant that in reality a range of Q^2 and x_B values were covered. The proton was detected at three different kinematic settings corresponding to a range of missing momentum values, $\vec{P}_m \sim 200 - 650$ MeV/c.

The analysis presented in this thesis focused on the $(e, e'p)$ reaction; the analyses of the multinucleon knockout $^{12}C(e, e', pn)$ and $^{12}C(e, e', pp)$ are presented in [10, 11]. The results of those analyses showed that the combined ratio of (e, e', pn) and (e, e', pp) to the $(e, e'p)$ yield, when all possible combinations of nucleon pairs are accounted for, was unity. This means the experiment observed a recoil partner nucleon which was ejected for every $(e, e'p)$ event.

The experimental cross-section has been extracted for both the $^{12}C(e, e', p)^{11}B$ and $^{12}C(e, e', p)$ continuum reaction channels. The subsequent momentum distribution (for the bound state data) and spectral functions (for the continuum data) have also been extracted.

The $^{12}C(e, e', p)^{11}B$ cross-section was extracted over a range of missing momentum of 200 - 400 MeV/c and compared with a theoretical calculation by J.M. Udias [9], which was based on a relativistic formalism. The experimental cross-section in this channel showed reasonably good agreement with the theoretical calculation for $P_m <$ 300 MeV/c, but disagreed at larger missing momenta. The calculation predicted an increase in the cross-section from around $\vec{P}_m \sim 350$ MeV/c upwards, but the data showed only a steady decrease in the cross-section. Unfortunately, the data stopped at missing momentum of 400 MeV/c and it would be interesting to see if there were any change in the cross-section trend at higher missing momenta values. The bound state data was not observed in kinematic settings which covered missing momenta above 400 MeV/c; this suggested that the cross-section continues to decrease above 400 MeV/c.

The cross-section for the $^{12}C(e, e', p)$ continuum reaction was extracted over a broad range of missing momentum and missing energy values—$\vec{P}_m \sim 200 - 600$ MeV/c and $E_m \sim 30 - 200$ MeV (higher in some cases). A simple model of the reaction mechanism for scattering from a quasideuteron in the nucleus, predicts a peak in the cross-section as a function of missing energy. Such a peak was observed in the data, but not at the missing energy values predicted by the model; the peak was always at a smaller missing energy value. The model assumes that when a proton is knocked-out of the nucleus, the partner neutron in the quasideuteron pair recoils with the missing momentum from the $(e, e'p)$ reaction, $\vec{P}_m$, and the (A-2) remaining nucleons are spectators at rest. However, since the experiment actually detected the recoil partner neutrons that are ejected when scattering off a quasideuteron pair, the data showed that the measured momentum of these neutrons is not the same as the $\vec{P}_m$ predicted from the (e, e', p) reaction data. It was shown that revising the model to account for the recoil neutron momentum being different from the missing momentum, resulted in a shift in the expected cross-section peak location to smaller missing energy values. This also indicates that the assumption of the (A-2) system being at rest is not correct. A further revision to the model to include an excitation energy of the (A-2) system was calculated. Although at lower missing momenta the cross-section peak was predicted to be at larger missing energies than observed in the data, the agreement improved with increasing missing momenta. This suggests that the data shows a possible transition from the (A-2) system being unexcited to having a significant excitation energy. This will be investigated further in the hope that the model of the reaction mechanism can be improved upon.

The reduced cross-section for the continuum reaction channel was extracted by dividing the experimental cross-section by the single-nucleon offshell cross-section. The σ_{cc2} prescription of DeForest [30] was used for the single-nucleon offshell cross-section. A comparison of the reduced cross-section as a function of missing energy for the same missing momentum bins from different kinematics showed disagreement between the data from different kinematics. This shows that the plane-wave impulse approximation does not describe the data well and reduced cross-section does not depend only on the missing energy and missing momentum, as that model requires.

The effective momentum density was evaluated by integrating the reduced cross-sections over missing energy. A function was fit to the peak in each reduced cross-section distribution, allowing the whole distribution including the tail region to be integrated. Comparing the effective momentum density for all three datasets together again showed the breakdown of the factorisation model. The data shows that other effects such as correlations or final state interactions have important contributions to the cross-sections at high missing energy and missing momentum.

Although the continuum channel cross-sections are not compared with any theoretical calculations, it is anticipated that calculations will be forthcoming in the future. Then, the comparison with theory will be interesting to see if the data can be described by calculations which are an improvement upon the plane-wave impulse approximation. These experimental cross-section data provide motivation for our theorist colleagues to produce calculations because now a direct comparision to experiment can be made.

Bibliography

[1] L. Lapikas, Nucl. Phys. **A553**, 297c (1993).

[2] K. S. Egiyan *et al.*, Phys. Rev. Lett. **96**, 082501 (2006).

[3] F. Benmokhtar *et al.*, Phys. Rev. Lett. **94**, 082305 (2005).

[4] T. Frick and H. Muther, Phys. Rev. **C68**, 034310 (2003).

[5] D. Rohe, Nucl. Phys. Proc. Suppl. **159**, 152 (2006).

[6] J. J. Kelly, Adv. Nucl. Phys. **23**, 75 (1996).

[7] K. G. Fissum *et al.*, Nucl. Instrum. Meth. **A474**, 108 (2001).

[8] *Table of Isotopes*, 7th ed., edited by C. M. Lederer and V. S. Shirley (J. Wiley and Sons, New York, 1978).

[9] J. M. Udias *et al.*, Phys. Rev. **C48**, 2731 (1993).

[10] R. Subedi, Ph.D. thesis, Kent State University, 2007.

[11] R. Shneor, Ph.D. thesis, Tel Aviv University, 2008.

[12] M. G. Mayer, Phys. Rev. **74**, 235 (1948).

[13] P. K. A. de Witt Huberts, J. Phys. **G16**, 507 (1990).

[14] G. Orlandini and M. Traini, Rept. Prog. Phys. **54**, 257 (1991).

[15] J. Morgenstern and Z. E. Meziani, Phys. Lett. **B515**, 269 (2001).

[16] G. van der Steenhoven, Nucl. Phys. **A527**, 17c (1991).

[17] L. J. H. M. Kester *et al.*, Phys. Rev. Lett. **74**, 1712 (1995).

[18] W. Bertozzi, E. Piasetzky, J. Watson and S. Wood, jefferson Lab Hall A Proposal **E01015**, (2000) (unpublished).

[19] B. Zhang, Ph.D. thesis, Massachusetts Institute of Technology, 2003.

[20] R. A. Niyazov *et al.*, Phys. Rev. Lett. **92**, 052303 (2004).

[21] A. Tang *et al.*, Phys. Rev. Lett. **90**, 042301 (2003).

[22] L. L. Frankfurt and M. I. Strikman, Phys. Rept. **76**, 215 (1981).

[23] L. L. Frankfurt and M. I. Strikman, Phys. Rept. **160**, 235 (1988).

[24] M. M. Rvachev *et al.*, Phys. Rev. Lett. **94**, 192302 (2005).

[25] R. G. Arnold *et al.*, Phys. Rev. **C42**, 1 (1990).

[26] J. M. Laget, Phys. Lett. **B199**, 493 (1987).

[27] D. Rohe *et al.*, Phys. Rev. Lett. **93**, 182501 (2004).

[28] R. Machleidt, F. Sammarruca, and Y. Song, Phys. Rev. **C53**, 1483 (1996).

[29] E. J. Moniz *et al.*, Phys. Rev. Lett. **26**, 445 (1971).

[30] T. De Forest, Nucl. Phys. **A392**, 232 (1983).

[31] JLab and Hall A webpages, http://www.jlab.org/, http://hallaweb.jlab.org/.

[32] J. Alcorn *et al.*, Nucl. Instr. Meth. **A522**, 294 (2004).

[33] C. W. Leemann, D. R. Douglas, and G. A. Krafft, Ann. Rev. Nucl. Part. Sci. **51**, 413 (2001).

[34] T. Maruyama *et al.*, Appl. Phys. Lett. **85**, 2640 (2004).

[35] M. Baylac *et al.*, Phys. Lett. **B539**, 8 (2002).

[36] N. Falletto *et al.*, Nucl. Inst. Meth. **A459**, 412 (2001).

[37] C. Yan, N. Sinkine, and R. Wojcik, Nucl. Instr. Meth. **A539**, 1 (2005).

[38] O. Ravel, Ph.D. thesis, Universite Blaise Pascal, Clermont-Ferrand, France, 1997.

[39] D. Marchand, Ph.D. thesis, Universite Blaise Pascal, Clermont-Ferrand, France, 1997.

[40] K. Unser, IEEE Trans. Nucl. Sci. **28**, 2344 (1981).

[41] Hall A Operations Manual, http://hallaweb.jlab.org/.

[42] J. Gao, Ph.D. thesis, Massachusetts Institute of Technology, 1999.

[43] D. J. J. de Lange *et al.*, Nucl. Instr. Meth. **A406**, 182 (1998).

[44] D. J. J. de Lange *et al.*, Nucl. Instr. Meth. **A416**, 254 (1998).

[45] Kanya aluminium extrusion system, http://www.kanya.com/.

[46] CODA Group webpages, http://coda.jlab.org/.

[47] Hall A C++ Analyzer, http://hallaweb.jlab.org/root/index.html/.

[48] ROOT project at CERN, http://root.cern.ch/.

[49] N. Liyanage, *Optics Calibration of the Hall A High Resolution Spectrometers using the C Optimizer*, Jefferson Lab Hall A Tech. Note 02-012, 2002, http://hallaweb.jlab.org/publications/Technotes/files/2002/02-012.pdf.

[50] M. Jones, *Report of Electronic Deadtime*, 2000, http://www.jlab.org/jones/e91011/report_on_deadtime.ps.

[51] MCEEP simulation homepage, http://hallaweb.jlab.org/software/mceep/mceep.html.

[52] D. B. Day, J. S. McCarthy, T. W. Donnelly, and I. Sick, Ann. Rev. Nucl. Part. Sci. **40**, 357 (1990).

[53] J. S. Schwinger, Phys. Rev. **75**, 898 (1949).

[54] S. Penner, nuclear Structure Physics, *Proc. of the 18th Scottish Univ. Summer School in Physics* (1977).

[55] E. Borie and D. Drechsel, Nucl. Phys. **A167**, 369 (1971).

[56] J. A. Templon, C. E. Vellidis, R. E. J. Florizone, and A. J. Sarty, Phys. Rev. **C61**, 014607 (2000).

[57] Y.-S. Tsai, Rev. Mod. Phys. **46**, 815 (1974).

[58] Y.-S. Tsai, Rev. Mod. Phys. **49**, 421 (1977).

[59] W. R. Leo, *Techniques for Nuclear and Particle Physics Experiments: A How-To Approach* (Springer-Verlag, Berlin, 1987).

[60] J. M. Udias, private communication.

[61] E. D. Cooper, S. Hama, B. C. Clark, and R. L. Mercer, Phys. Rev. **C47**, 297 (1993).

[62] J. Le Goff *et al.*, Phys. Rev. C **55**, 1600 (1997).

[63] C. Marchand *et al.*, Phys. Rev. Lett. **60**, 1703 (1988).

Acknowledgements

There have been many people that have helped me along the way to my PhD, so if I have forgotten you here, please forgive me.

First and foremost I owe a huge debt of thanks to my research supervisor, Prof. Bill Bertozzi. Bill's knowledge and experience in nuclear physics is truly amazing and his enthusiasim has never diminished in the years I have known him. Bill also has a caring attitude towards his students and I am thankful for his patience and faith in me as his student, especially during the times when I struggled with the dreaded general exams. I thank Bill for all his help, guidance and advice.

I also wish to thank Shalev Gilad for his help and guidance in my research, especially during the data analysis after the experiment finished. Shalev's additional supervision for my thesis and help in keeping me 'on track' has been incredibly helpful.

I thank Douglas Higinbotham for all of his help and support while I have been doing research at Jefferson Lab, especially in making the initial transition from life in Boston to Virginia. Doug has an excellent understanding of both the physics and the practical requirements to do any experiment at Jefferson Lab. Doug's help and contributions before, during and after the experiment cannot be understated. I have learned many things from Doug about physics and research and I can only hope that perhaps he may have learned something from me as well during our many fruitful discussions, even if it was only to never, *ever* drink draught Guinness straight from the can; it should always be decanted into a glass first.

My fellow graduate students Ran Shneor and Ramesh Subedi deserve many thanks for all their efforts and hard work. Together we built the detectors, set up all the equipment, worked on the software, took shifts when the experiment was running and then analysed all the data. Without their help and support, it would have been quite a different story. I also wish to thank the other spokespersons for our experiment, Eli Piasetzky, John Watson and Steve Wood. Their knowledge and experience has guided all of us throughout the experiment. Also a big 'thank you' goes to Robert Feuerbach for all his help with the analysis and with learning much more about the

ROOT analysis software. My thanks to the Hall A staff and collaboration for their help with the experiment.

I thank Prof. Bill Donnelly and Prof. Richard Milner for being on my thesis committee and for their guidance and helpful advice during my research. I also thank them for reading my thesis and the feedback and improvements they have suggested.

My thanks to my friend Simon Širca who provided much help and feedback while I was working on the data analysis and writing my thesis. I have enjoyed our many discussions and I'm pleased to have encountered someone else who shares my appreciation for fine Swiss timepieces. It's always nice to dream about what we might wear if physicists were paid properly for all their hard work; Blancpain, Girard-Perregaux, Ulysse-Nardin .... What is that Aerosmith song called?

Although I only spent a couple of years in Boston before moving to Virginia to do my research, I made some truly lasting friendships there. My thanks to Conor Henderson, Miranda McGill, Oliver Dial, Jay Kane, Susan Dunne, Gary Steele, Kevin and Katie Turner, Lara Greden, Sejal Patel, Linda Kalnejais, Corey Reed, Tom Ewing and Yasmine Abbas. Wherever you all are in the world, I hope you are having fun, just like our THDA days. My thanks especially to Miranda and Oliver for their hospitality and support during the last few weeks of my thesis writing and defense—it really made a huge difference!

It was an interesting twist of fate that while I was still at MIT, my friend Henriette Elvang, who I've known since my time as an undergraduate at the University of Edinburgh, ended up coming to MIT for a postdoc position. My thanks for the encouragement and support and inspiration that I could finish this PhD.

During my research at Jefferson Lab I was fortunate to make more friends that have made my experiences their so much more enjoyable. My thanks to Al Gavalya and Joyce Miller for their design work on our detector systems and the many meals and fine wines we have enjoyed together. My thanks also to Jack Segal, Rolf Ent and Walter Kellner for the times we've been out to enjoy a few beers together. I also thank Paul Ulmer for taking the time on many occasions to discuss physics and the simulation code, giving me a much better understanding of both. Thanks also to Kevin Fissum for the many useful discussions and guidance he provided as well. I wish to thank Xiaochao Zheng, Alexandre Deur, Marcy Stutzman, Vincent Sulkosky, Bryan Moffit, Nikos Sparveris, Olivier Gayou, Rikki Roche, Fatiha Benmokhtar, Tania Horn, Paul King, Julie Roche, Andrew Puckett, Yi Qiang and Jaideep Singh for helping make my experiences at Jefferson Lab much more fun; I'm sure I have left someone out of this list, so my apologies if you are not mentioned.

I was also fortunate to join a football team in an adult league while living in Virginia. I have enjoyed many good times with my teammates David Hearne, Mark Chipchase, Mike Crawshaw, Jo Dudek, Mike Mitchell and Kevin Kendall. A special 'thank you' to Kevin Kendall for having the courage and audacity to introduce me to Jen, who eventually became my wife.

My family has always been supportive and encouraging throughout my life, especially when I made the decision to come to America for graduate school and for that I am truly grateful. My wife, Jen, has been a source of constant love and support, especially as I worked to finish everything off and I am thankful for all of her love and help. I am truly blessed with the family I have. Finally, for Mum, gone, but not forgotten, keep an eye out over me.